UNIVERSITY OF OKLAHOMA

GRADUATE COLLEGE

CORE BASED DEPOSITIONAL, CHEMOSTRATIGRAPHIC, AND DIAGENETIC ANALYSIS OF THE UPPER WOLFCAMP, SOUTHERN DELAWARE BASIN, TEXAS

A THESIS

SUBMITTED TO THE GRADUATE FACULTY

in partial fulfillment of the requirements for the

Degree of

MASTER OF SCIENCE

By

CALVIN THOMAS LAYMAN

Norman, Oklahoma

2019

CORE BASED DEPOSITIONAL, CHEMOSTRATIGRAPHIC, AND DIAGENETIC ANALYSIS OF THE UPPER WOLFCAMP, SOUTHERN DELAWARE BASIN, TEXAS

A THESIS APPROVED FOR THE

CONOCOPHILLIPS SCHOOL OF GEOLOGY AND GEOPHYSICS

BY

Dr. R. Douglas Elmore, Chair

Dr. John D. Pigott

Dr. Matthew J. Pranter

Dedication

I want to dedicate this work to my fiancé, Amanda, and to my parents.

Amanda, you are my rock and I could not have completed this without you. Even after all of the challenges we have faced I can always count on you to be there for me with a smile.

Mom and Dad, you instilled in me the love of the Earth, and always push me to do good work.

Acknowledgements

Thank you to Dr. R. Douglas Elmore for your help and patience while I worked to complete my thesis work. Thank you to the folks at Parsley Energy for providing the core, data, and support for this project. Thank you to my committee members Dr. John D. Pigott, and Matthew J. Pranter for your guidance and advice. Thank you to Dr. Roger Slatt for allowing me to use the handheld XRF and your labs to work on my core.

Abstract

CORE BASED DEPOSITIONAL, CHEMOSTRATIGRAPHIC, AND DIAGENETIC ANALYSIS OF THE UPPER WOLFCAMP, THE SOUTHERN DELAWARE BASIN, TEXAS

Calvin Layman, R. Douglas Elmore

School of Geology and Geophysics, University of Oklahoma

The Wolfcamp Series in the Southern Delaware Basin of West Texas is Permian in age and is composed of a mix of siliciclastics and carbonates deposited through pelagic sedimentation, turbidity currents, and mass wasting in a deep-water environment. A more isolated depositional system was present in the study area than in the rest of the Southern Delaware basin during Wolfcamp time. The Central Basin Platform to the East, and the Waha and Coyanosa structural features to the West and South form a mini basin in northern Pecos County. Isolation resulted in lithologies with less siliciclastic input compared to other areas in the Southern Delaware Basin. One objective of the study is to determine the depositional setting for the Wolfcamp Formation in this sub basin in order to characterize the reservoir and specifically test if a turbidite fan model is applicable to the Wolfcamp Formation in this study area. A second objective is to characterize the diagenesis and test if there is evidence for alteration by late fluids.

Using a core from the Southern Delaware Basin, the reservoir characteristics of the upper Wolfcamp are being analyzed. Eight different lithofacies were observed in the core. Two of the more siliceous lithofacies have the best reservoir characteristics. Based on observed depositional features, stacking patterns, chemostratigraphic proxies, log character, and thin section

observations, it is hypothesized that a channelized submarine fan system was active off the Central Basin Platform during Upper Wolfcamp deposition in the study area. An overall coarsening upward package is interpreted as the system was prograding out into the basin. Levee deposits, lobes, and channel fill deposits are present in the cored interval.

Diagenesis is complex, with multiple stages and multiple paragenetic sequences observed throughout the core. Different lithologies have experienced varying degrees of diagenesis. The carbonate clasts inherited diagenetic features from the source area and record events during late diagenesis in the basin. Mudstones features that are both internally and externally sourced phases. Early diagenesis contains phases that are primarily self-sourced. Middle and late diagenesis contains mineralized fractures and other diagenetic phases acquired from external fluids migrating through the system.

TABLE OF CONTENTS

List of Tables

List of Figures

Introduction

The greater Permian Basin of West Texas has been actively drilled for hydrocarbons since oil was discovered in the Spraberry in 1949. The Wolfcamp Formation has more recently become of interest with the integration of horizontal drilling and hydraulic fracturing (Kutchin, 2001). While depositional studies have been previously performed on the Wolfcamp of the Southern Delaware basin (Moede, 2018), this is not the case for a sub basin between the Central Basin Platform to the East and the complex structural features of the Coyanosa and Waha rises to the Sest and South (Figure 1). In particular, the depositional setting is not known and was likely influenced by Central Basin Platform and the Coyanosa and Waha rises.

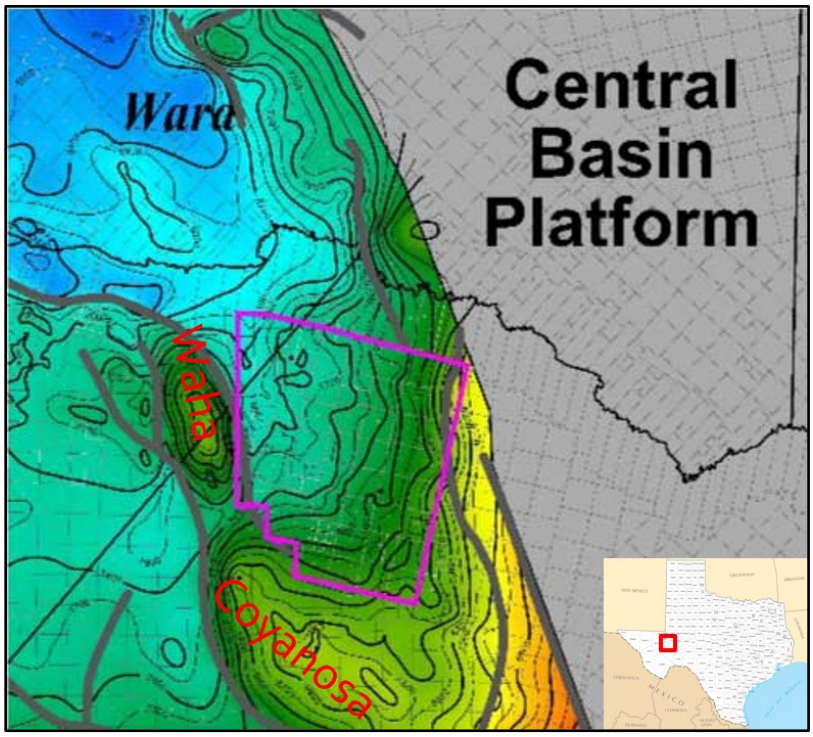

Figure 1: Structural top of the Upper Wolfcamp formation with outline of the project area (Parsley Energy). Inset map shows location

One objective of this study is to determine the depositional setting and larger depositional controls for the Wolfcamp Formation in this sub basin in order to characterize the reservoir. I

will specifically test if a turbidite fan model is applicable to the carbonate rich Wolfcamp formation in this study area. Previously for the Southern Delaware, rocks similar to this study were modelled as a carbonate debris apron (Moede, 2018).

In addition, the proximity of the study area to structure and faults suggests that fluid movement after deposition could have resulted in diagenetic alteration. A second objective for this study is to characterize the diagenesis. I will specifically test if there is evidence that late fluid alteration influenced the paragenesis and if the Upper Wolfcamp is an open or closed system with regards to diagenetic fluids.

The depositional and diagenetic setting could produce reservoir properties different from those observed in the rest of the basin and highlights the need for further characterization of the reservoir to understand the best intervals for drilling and completion. As a result, this study focuses on identifying the depositional system, comparing lithofacies and chemofacies, characterizing the diagenesis, and investigating for late fluid interaction of the Upper Wolfcamp, from one core in northern Pecos County, Texas.

Geologic Setting

The Permian Basin of West Texas is a prolific producer of oil and gas (Broadhead, 2004). The Wolfcamp Formation in the Permian Basin has been the subject of numerous studies (Udden et al., 1917; Baker, 1928; King, 1942). The sub basin between the Central Basin Platform and the complex structural features of the Coyanosa and Waha rises (Figure 1) has not received as much attention as other areas and is the focus of this study. An idealized stratigraphic section from Ver Wiebe 1957 can be seen in Figures 2 and 3.

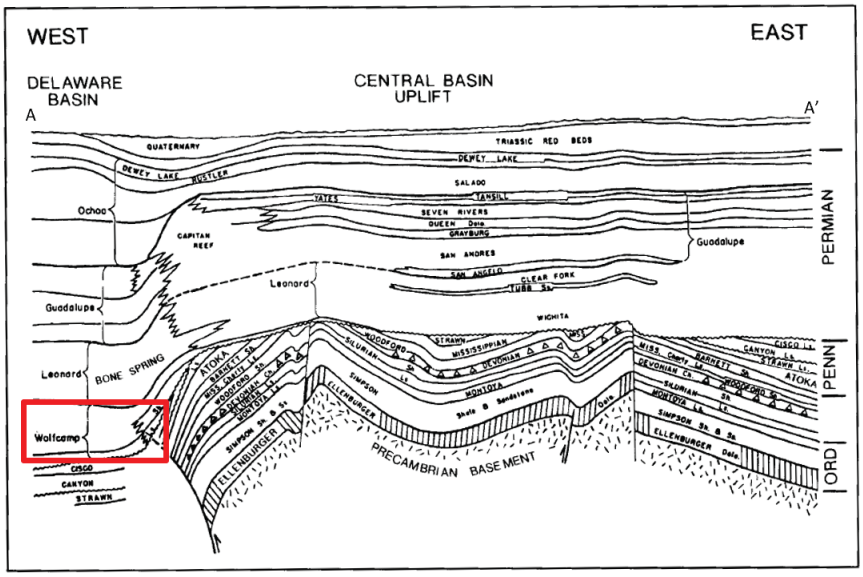

Figure 2: Generalized stratigraphic cross section, Central Basin Uplift and adjacent Delaware basin with red box showing highlighted area of inferred deposition for this study from Ver Wiebe 1957.

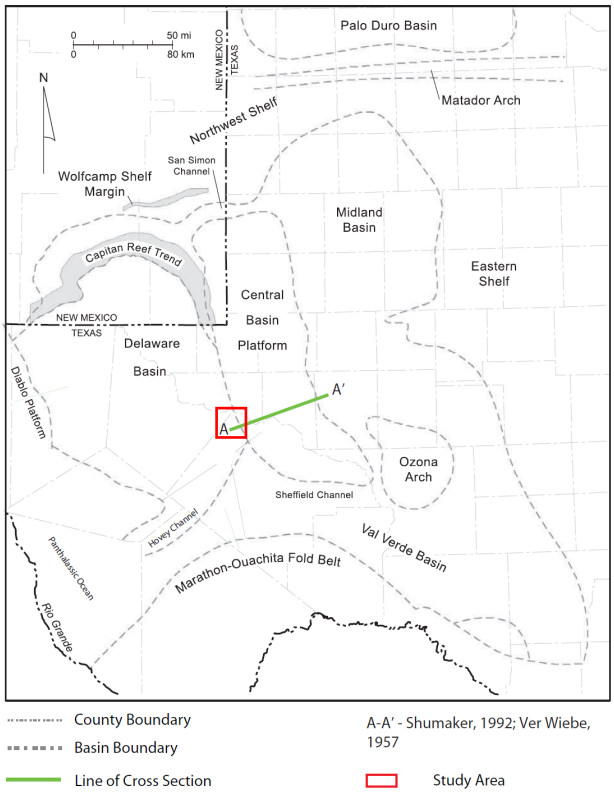

Figure 3: Major subdivisions and boundaries of the Permian Basin in West Texas and Southeast New Mexico. Adapted from Moede (2016). Location of A-A' cross section from Figure 2 is shown.

During Lower Ordovician time, the sagging transcontinental arch produced a flattened coastal plain across which the Ellenburger Sea deposited carbonate sediments in what is now Texas and New Mexico. Circulation in the broad, shallow sea was restricted and Ellenburger sediments were dolomitized after deposition (Adams 1965). By the Middle Ordovician the Tobosa basin had developed between the Texas arch on the East and the Diablo arch on the West (Adams 1965). In the beginning of the Mississippian, the large Tobosa Basin (Galley,1958) began experiencing tectonic activity when Gondwana collided with North America (Mazzullo, 1995). This resulted in deformation of the Tobosa basin along high angle basement faults (Horak, 1985) to create the Midland Basin to the East, the Central Basin Platform in the center, and the Delaware Basin to the West (Figure 3). During the Middle Mississippian, compression continued which tilted the Delaware Basin to the East and uplifted the Central Basin Platform (Hills, 1984).

During the Early Pennsylvanian the Permian Basin began to rapidly subside. In the southern portion of the Delaware basin, mainly shale was deposited (Adams, 1965). In the Middle and Late Pennsylvanian tectonism increased and large carbonate platforms began to rim both the Midland and Delaware Basins (Hills, 1984).

In Early Permian time, active tectonism, fluctuating sea level (Mazullo and Reid 1988; Flamm, 2008) and an active carbonate platform, all contributed to the large amount of sediment deposited in the study area during the Upper Wolfcamp. This produced a mix of clay rich shales and shelf sourced calclithites. The project area is about five and a half to six miles away from the platform (Figure 4). While still a basinal setting, the project area was proximal to a large active carbonate platform on the central uplift during Wolfcamp time. Additionally, the tectonically active Central Basin Platform to the East and the Waha and Coyanosa structural features to the West and South created a depositional sub basin. Structural evolution of the area

has been described by Van Wiebe (1957), Adams (1965), Ross (1986), Shumaker (1992), Yang and Dorobek (1995), and Tai and Dorobek (2000). Movement along high angle basement faults near the Central Basin Platform is inferred based on thinning of Wolfcamp sediments across the Waha and Coyanosa structures (Figures 5 and 6) (Schumaker,1992; Hardage, 1999; personal communication with Delaware Basin team at Parsley Energy).

In the Middle to Late Permian, subsidence rapidly decreased. By the Late Permian (Ochoan), growing carbonate reefs and banks caused circulation in the basin to be greatly reduced (Adams,1965) and created a lagoon. The broad, restricted lagoon resulted in deposition of the Ochoan evaporites (Adams 1965). Continued restriction then resulted in the deposition of the Castile evaporite in the Delaware Basin. Dolomitization also occurred during this interval through circulation of saturated brines (Hills, 1984). Hypersaline fluids generated during this time could have potentially circulated down into Wolfcampian sediments.

From the end of the Permian to the Late Cretaceous, no significant structures were formed within the basin. Some terrestrial clastics were deposited during the Triassic along with some early Cretaceous sediments. During the Late Cretaceous through the Early Eocene, the Laramide Orogeny deformed the Permian sediments. The orogeny elevated the western side of the Delaware Basin up to 4000 ft and pushed the basin above sea level permanently (Horak, 1985). Laramide deformation could have reactiveated faults in and around the project area and could also have caused migration of fluids.

Analogous areas to the study area within the Southern Delaware Basin have been described by both Moede (2016) and Coldwell (1991). The cores from both of these studies showed large, coarse grained allochtonous carbonate flow deposits. Other similar depositional settings have been described by Hobson et al. (1985) and Louks et al. (1985). However, because

of the Coyanosa and Waha structures described by Shumaker (1992), the area in this study had a depositional environment that was more restricted than other areas in the Delaware Basin.

Diagenesis in the Upper Wolfcamp has been described by Zoeten et al. (2017) and Wickard et al. (2016). Both studies were in the Midland basin. Previous studies of diagenesis in the Delaware Basin have primarily been focused on the large carbonate reef complex in the northwestern part of the basin (Mazzullo, 1994).

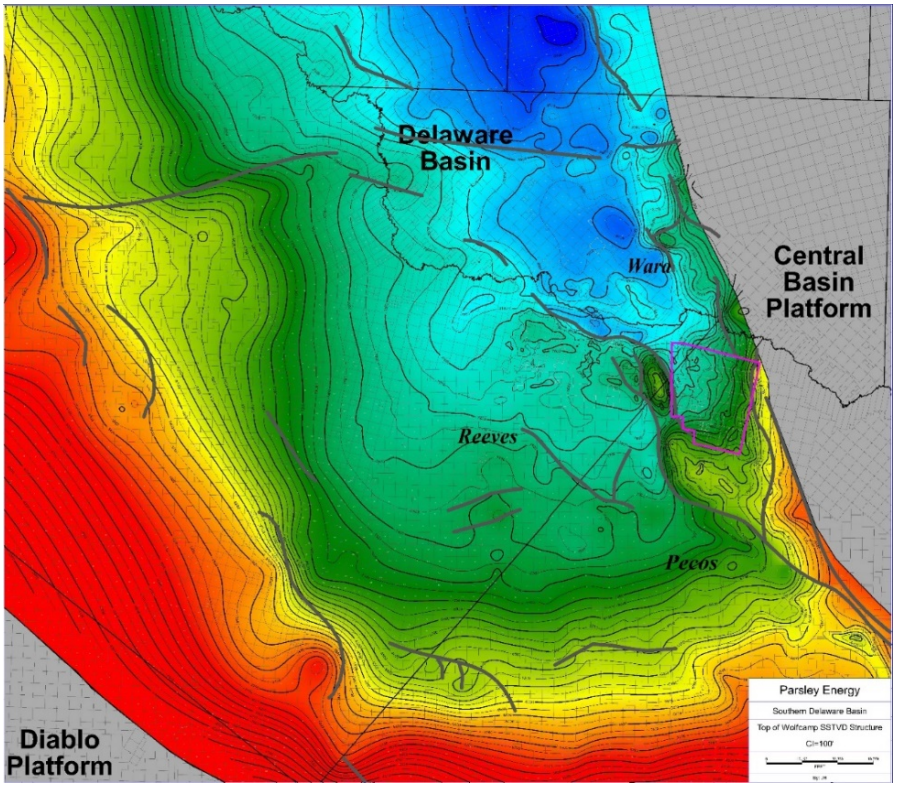

Figure 4: Map showing the structural top of the Wolfcamp and Project Area Outline (Parsley Energy).

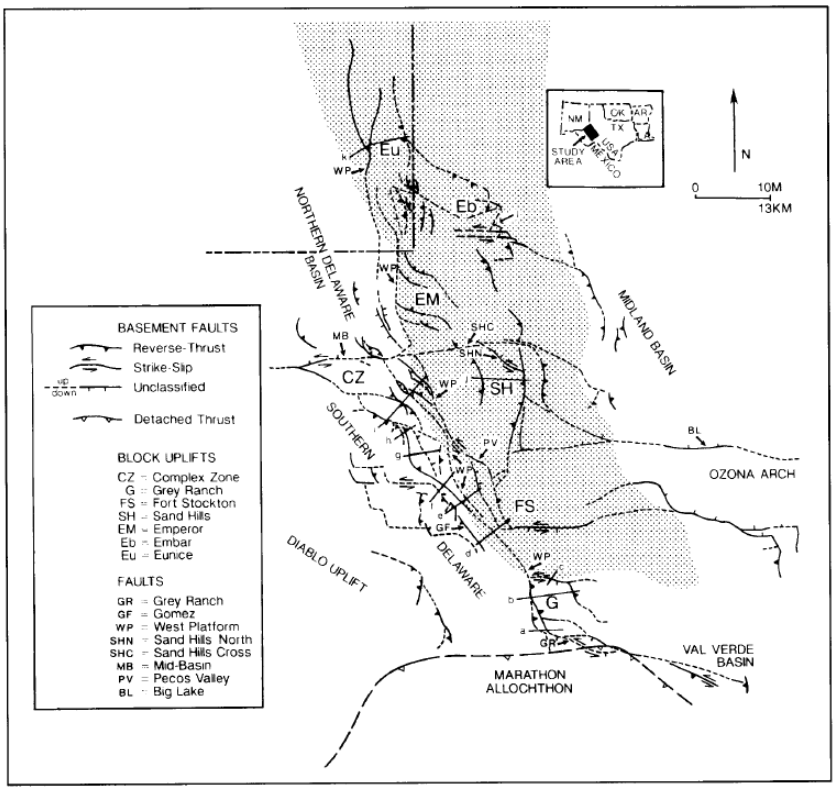

Figure 5: Tectonic map showing late Paleozoic sub surface structures and section line locations for Figure 5. Shumaker (1992).

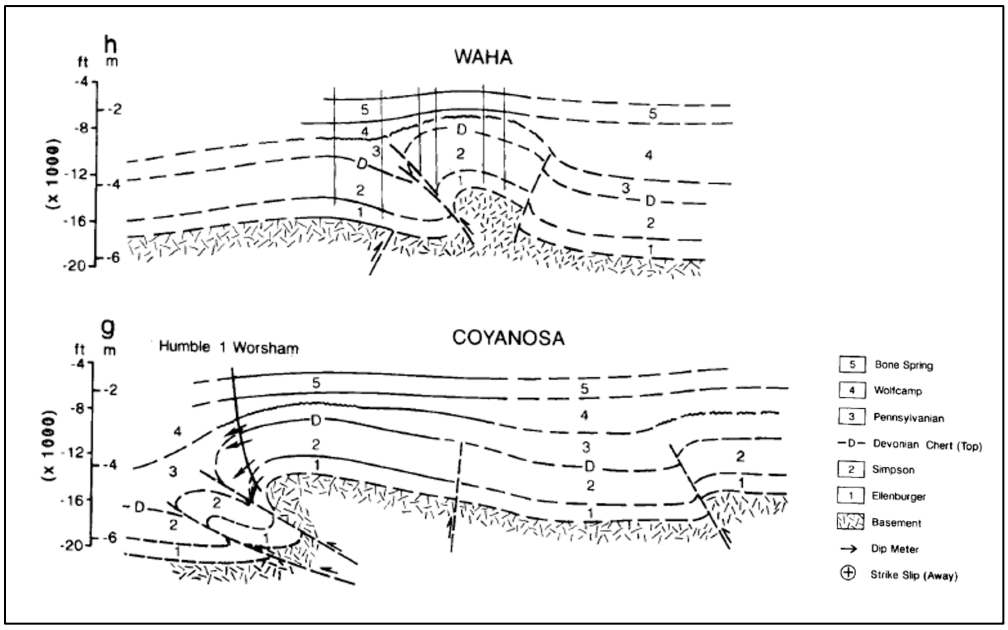

Figure 6: Structural sections across the Frontal fold and West Platform fault zone along the Fort Stockton block. Shumaker (1992)

Methods

Core Description and Facies

The entire 573 feet (175 meters) of cored interval was described based on grainsize, composition, sedimentary structures, and other characteristics (e.g., fossils, fractures, etc.). Once the core was fully described, intervals were separated into descriptive facies that were then interpreted based on inferred processes and the interpreted depositional system.

Handheld XRF

Chemostratigraphic analysis was performed using a Bruker Tracer IV-SD handheld X-ray fluorescence gun at a six-inch interval on the core slab face. Measurements for both major and trace elements were performed. The core was prepared by first thoroughly cleaning the face of the slab and then using stickers to demarcate every 6 inches for measurement. Each sample site was scanned for 90 seconds at 15 kV with a vacuum pump for major elements, and 60 seconds at 40kV for trace elements. Notes on general lithology were taken at each measurement point. XRF measurements were calibrated using Bruker's excel macro based on calibrations for mudrocks (Rowe et al. 2012). A chemostratigraphic framework was developed based on elemental proxies and Hierarchical Clustering Analysis (HCA) (Turner, 2016).

X-Ray Defraction

XRD was performed by personnel at the Chesapeake labs using sixty-five plugs taken from the core butt to determine mineralogy. Plugs were crushed and powdered and then analyzed with a Bruker Diffractometer. Results were presented in weight percent mineralogy. A priority was given to sampling shales.

TOC, Porosity, and Saturations

Total organic carbon (TOC), porosity, and saturation measurements were performed by personnel at the Chesapeake labs using 103 plugs taken from core butts.

Geomechanics

Geomechanical properties were measured using a Proceq Bambino 2 Leeb Hardness Tester. Five geomechanical measurements were taken at each XRF measurement point on the slab with the mean and standard deviations calculated. The average of the five geomechanical measurements was used to generate a log for relative mechanical strength. The measurement acquired was unitless, so the measurement is a relative measurement throughout the core. Properties such as relative "frackability" will be inferred using these measurements.

Petrography and Diagenesis

Forty-four plugs were selected for thin sections throughout the cored interval. Thin sections were cut by Spectrum Petrographic. Blue epoxy was used to indicate open porosity within the rock. Selected thin sections containing abundant carbonate material were stained with Alizarin Red to help identify calcite and dolomite. Wentworth classification (Wentworth, 1922) was used for clastics and Dunham classification (Dunham, 1962) was used for carbonates. A Zeiss AxioImager.Z1m petrographic microscope was used for petrographic analysis and scanning electron microscope work was performed using a FEI Quantum 250 Scanning Electron Microscope (SEM) with an attached Bruker Electron Dispersive Spectrometer (EDS) to further characterize the diagenesis.

Results and Interpretation

Lithofacies Descriptions

Throughout the cored interval, six different lithofacies were identified; Argillaceous Siliceous Silty Shale, Interbedded Laminated Calclithite and Argillaceous Siliceous Silty Shale, Open-Framework Bioclastic Argillaceous Siliceous Mudstone, Crinoid Brachiopod Bryozoan Wackestone and Packstone, Oligomictic Limestone Extraclast Paraconglomerate, and Calcite Cemented Fine Grained Arkose. The full description profile with gamma ray log is shown in Figure 7, and the full core description can be seen in appendix 1. Tables with average values from XRD and XRF for each facies are shown in tables 1 and 2 respectively. Thin sections with their interpreted lithofacies are shown in table 3.

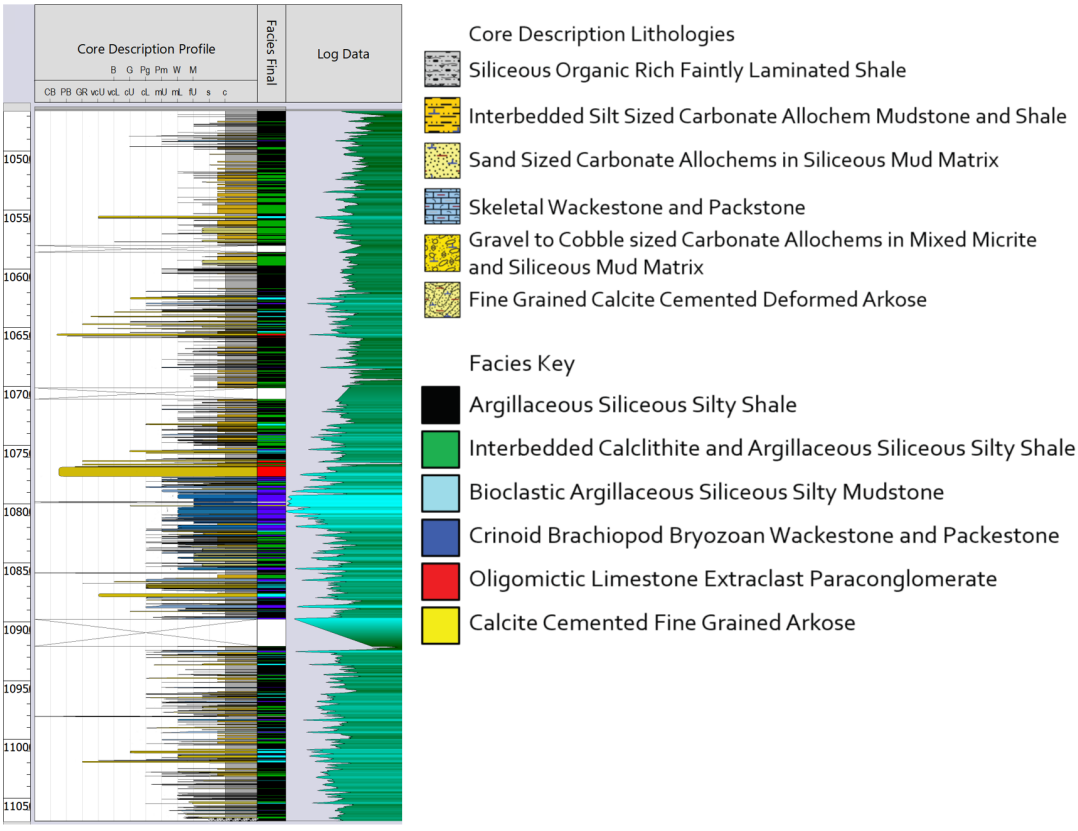

Figure 7: Core Description Profile with associated lithofacies and Gamma Ray log.

Table 1: Average Mineralogy in Weight % for lithofacies from XRD.

Facies	Quartz	K-Feldspar	Plagioclase	Apatite	Pyrite	Calcite	Dolomite	Mixed-Layer ILLITE/SMECTITE	Illite+Mica	TOTAL Clay
Argillaceous Siliceous Silty Shale	52.88	0.29	5.59	0.47	2.70	4.06	3.42	7.51	23.04	30.58
Interbedded Laminated Calclithite and Argillaceous Siliceous Black Shale	46.93	0.19	5.15	1.67	2.69	14.63	3.02	6.15	19.43	25.72
Open-Framework Bioclastic Argillaceous Siliceous Mudstone	25.79	0.18	2.60	0.39	2.01	55.29	2.52	2.82	8.40	11.22
Crinoid Brachiopod Bryozoan Wackestone and Packstone	16.97	0.16	1.86	0.67	1.31	70.44	3.34	1.32	3.93	5.25
Oligomictic Limestone Extraclast Paraconglomerate	N/A	N/A	N/A	N/A	N/A	N/A	N/A	N/A	N/A	N/A
Calcite Cemented Fine Arkose	N/A	N/A	N/A	N/A	N/A	N/A	N/A	N/A	N/A	N/A

Table 2: Average elemental abundances in parts per million for lithofacies from XRF.

Facies	Si (ppm)	Na (ppm)	Al (ppm)	K (ppm)	Ca (ppm)	Mg (ppm)	P (ppm)	S (ppm)	Fe (ppm)	Ti (ppm)	Zr (ppm)	Mo (ppm)	V (ppm)	Ni (ppm)
Argillaceous Siliceous Silty Shale	244322.89	4312.81	34200.73	13187.93	39550.07	4169.90	1443.03	47599.90	22391.33	2345.48	109.16	21.74	88.81	80.69
Interbedded Laminated Calclithite and Argillaceous Siliceous Black Shale	217218.50	4766.42	36622.96	12880.34	88111.26	3544.10	977.16	19968.86	21205.85	2382.58	110.40	19.81	132.13	71.97
Open-Framework Bioclastic Argillaceous Siliceous Mudstone	165712.19	4121.36	16411.17	5551.52	160499.14	3605.02	1361.20	16832.35	13769.96	1250.26	49.09	9.73	81.15	49.48
Crinoid Brachiopod Bryozoan Wackestone and Packstone	79894.91	3081.41	5902.74	2096.97	268311.76	4878.81	722.85	7595.12	6734.85	572.13	22.78	3.81	68.38	27.74
Oligomictic Limestone Intraclast Paraconglomerate	101950.70	3527.43	10916.78	3698.46	238077.48	4188.57	739.06	9255.74	8245.90	889.56	37.32	7.02	63.23	35.27
Calcite Cemented Fine Arkose	115406.51	11904.99	0.00	0.00	48982.19	0.00	0.00	515.90	2318.29	0.00	14.66	10.46	0.00	11.45

Table 3: Thin sections with associated depth (ft) and lithofacies.

Sample Name	Depth	Facies
TR-S2	10474.5	Argillaceous Siliceous Silty Black Shale
TR-CS6	10487.8	Argillaceous Siliceous Silty Black Shale
TR-S7	10489.8	Argillaceous Siliceous Silty Black Shale
TR-S15	10521.2	Interbedded Laminated Calclithite and Argillaceous Siliceous Silty Black Shale
TR-CS17	10531.3	Interbedded Laminated Calclithite and Argillaceous Siliceous Silty Black Shale
TR-S20	10550.2	Interbedded Laminated Calclithite and Argillaceous Siliceous Silty Black Shale
TR-S21	10555.7	Open Framework Bioclastic Argillaceous Siliceous Mudstone
TR-CS21	10555.7	Open Framework Bioclastic Argillaceous Siliceous Mudstone
TR-S25	10586.4	Argillaceous Siliceous Silty Black Shale
TR-CS27	10590.8	Interbedded Laminated Calclithite and Argillaceous Siliceous Silty Black Shale
TR-S30	10624.5	Open Framework Bioclastic Argillaceous Siliceous Mudstone
TR-S31	10628.2	Argillaceous Siliceous Silty Black Shale
TR-CS35	10644.5	Interbedded Laminated Calclithite and Argillaceous Siliceous Silty Black Shale
TR-S39	10662.2	Open Framework Bioclastic Argillaceous Siliceous Mudstone
TR-CS39	10662.2	Open Framework Bioclastic Argillaceous Siliceous Mudstone
TR-S42	10672.2	Argillaceous Siliceous Silty Black Shale
TR-CS44	10678.4	Interbedded Laminated Calclithite and Argillaceous Siliceous Silty Black Shale
TR-CS46	10684.3	Open Framework Bioclastic Argillaceous Siliceous Mudstone
TR-S48	10690.9	Argillaceous Siliceous Silty Black Shale
TR-CS50	10694.2	Argillaceous Siliceous Silty Black Shale
TR-S55	10723.1	Argillaceous Siliceous Silty Black Shale
TR-CS58	10746.1	Open Framework Bioclastic Argillaceous Siliceous Mudstone
TR-S60	10756.3	Open Framework Bioclastic Argillaceous Siliceous Mudstone
TR-S61	10758.7	Argillaceous Siliceous Silty Black Shale
TR-S63	10776.1	Oligomictic Limestone Extraclast Paraconglomerate
TR-CS63	10776.1	Oligomictic Limestone Extraclast Paraconglomerate
TR-S64	10788.5	Crinoid Brachiopod Bryozoan Wackestone and Packstone
TR-S65	10797.5	Crinoid Brachiopod Bryozoan Wackestone and Packstone
TR-S69	10850	Argillaceous Siliceous Silty Black Shale
TR-S71	10866.8	Argillaceous Siliceous Silty Black Shale
TR-S74	10893.6	Argillaceous Siliceous Silty Black Shale
TR-S75-2	10897.2	Crinoid Brachiopod Bryozoan Wackestone and Packstone
TR-S75	10897.2	Crinoid Brachiopod Bryozoan Wackestone and Packstone
TR-CS82	10951.3	Interbedded Laminated Calclithite and Argillaceous Siliceous Silty Black Shale
TR-10963 (84)	10963	Crinoid Brachiopod Bryozoan Wackestone and Packstone
TR-CS86	10973.2	Interbedded Laminated Calclithite and Argillaceous Siliceous Silty Black Shale
TR-10983	10983	Crinoid Brachiopod Bryozoan Wackestone and Packstone
TR-S89	10986	Argillaceous Siliceous Silty Black Shale
TR-S91	10994.3	Crinoid Brachiopod Bryozoan Wackestone and Packstone
TR-S92	10998	Argillaceous Siliceous Silty Black Shale
TR-CS92	10998	Argillaceous Siliceous Silty Black Shale
TR-S97	11026.7	Interbedded Laminated Calclithite and Argillaceous Siliceous Silty Black Shale
TR-S98	11029.6	Interbedded Laminated Calclithite and Argillaceous Siliceous Silty Black Shale
TR-S102	11050.7	Open Framework Bioclastic Argillaceous Siliceous Mudstone

Argillaceous Siliceous Silty Shale

This is the most abundant facies observed in the core. The facies is dominantly silt sized quartz, albite, and carbonate clasts in an illite matrix. Characteristic images of the facies at both core and thin section scale can be seen in Figures 8 A through F and 9 A through F. Based on 41 XRD measurements from plugs, the facies on average is 52.9% quartz, 0.3% k-feldspar, 5.6% plagioclase, 0.5% apatite, 2.7% pyrite, 4.1% calcite, 3.4% dolomite, and 30.6% clay minerals. Based on 542 XRF points, the average elemental abundances in parts per million are displayed in Figure 10. On average the lithofacies is silica rich with high values of sulfur, calcium, aluminum, iron, and potassium. Ferroan rimmed dolomites, framboidal pyrite, pyritized allochems, partially dissolved feldspars, calcite allochems and, detrital feldspars and illite were observed in thin section.

The most common fossils observed in thin section were radiolarians, calcispheres, Schwagerina fusulinids, crinoids, brachiopods, peloids, and sponge spicules (Figure 9B and 9D). Fistuloporid bryozoan pieces were observed in two thin sections but were rare.

The facies is usually faintly to planar laminated and fissile (Figure 8A). Thin carbonate starved ripples were also present (Figure 8E). Small laminations of quartz silt, carbonate allochems, and clay were commonly observed in thin section (Figure 9A and 9C). Siderite and pyrite were present as both lamina and nodules at both hand sample (Figure 8B and 8F) and thin section scale (Figure 9D). Carbonate nodules were also present. Trace fossils were present throughout this facies with nereites being observed at both hand sample scale (Figure 8D) and thin section scale (Figure 9F). Thin, horizontal mineralized fractures were common in this facies as well as larger vertical mineralized fractures. When the facies was juxtaposed to more carbonate rich intervals, injectites were sometimes observed (Figure 8C).

Process interpretations are based on the model of subaqueous sedimentary flows and their deposits (Mulder et al., 2001) (Figure 11) compared to the observed lithologies and stacking patterns. The argillaceous siliceous silty shale facies is interpreted to be deposited through hemipelagic sedimentation and distal turbidity flow. The small starved ripples within the facies were likely a result of the distal turbidity flows.

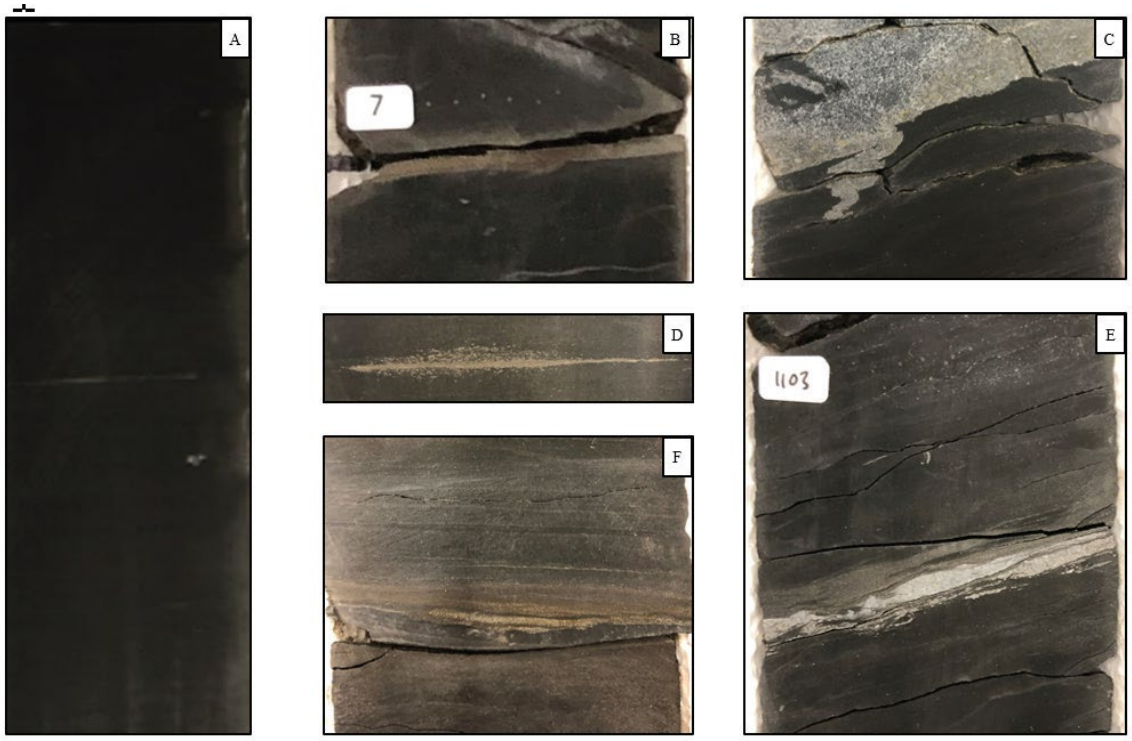

Figure 8: Core scale sedimentary features of argillaceous Siliceous Silty Shale facies. (A) Characteristic interval of argillaceous siliceous silty shale. Black in color with faint laminations. (B) Pyrite and siderite rich lamination (C) Carbonate rich injectite into argillaceous siliceous silty shale (D) Grazing trace fossil (E) Starved carbonate and quartz silt ripples (F) Pyrite and siderite rich planar laminations.

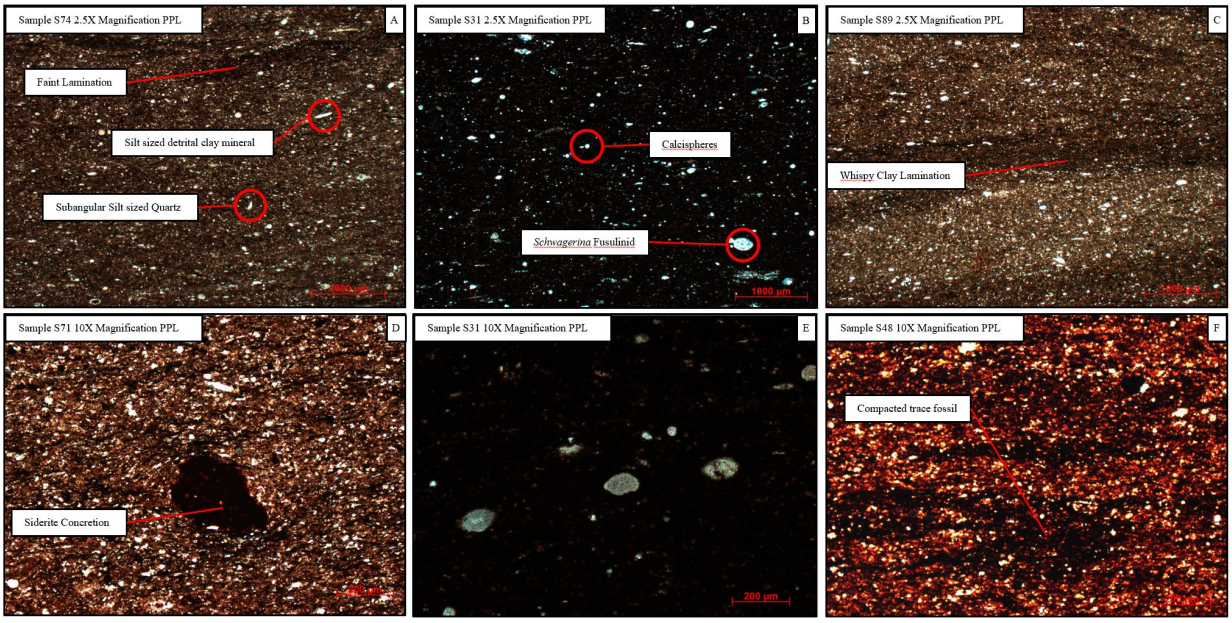

Figure 9: *Thin section scale sedimentary features of argillaceous siliceous silty shale (A) Characteristic photomicrograph of argillaceous siliceous silty shale. Thin section shows subangular to subround silt and clay sized quartz, albite, clays, and carbonate allochems. Faint laminations are also present. (B) Calcispheres and Schwagerina fusulinids. (C) Wispy clay and quartz silt laminations. (D) Siderite concretion with surrounding clay compacted. (E) Schwagerina fusulinids in siliceous muds. (F) Compacted burrows or grazing trace fossils.*

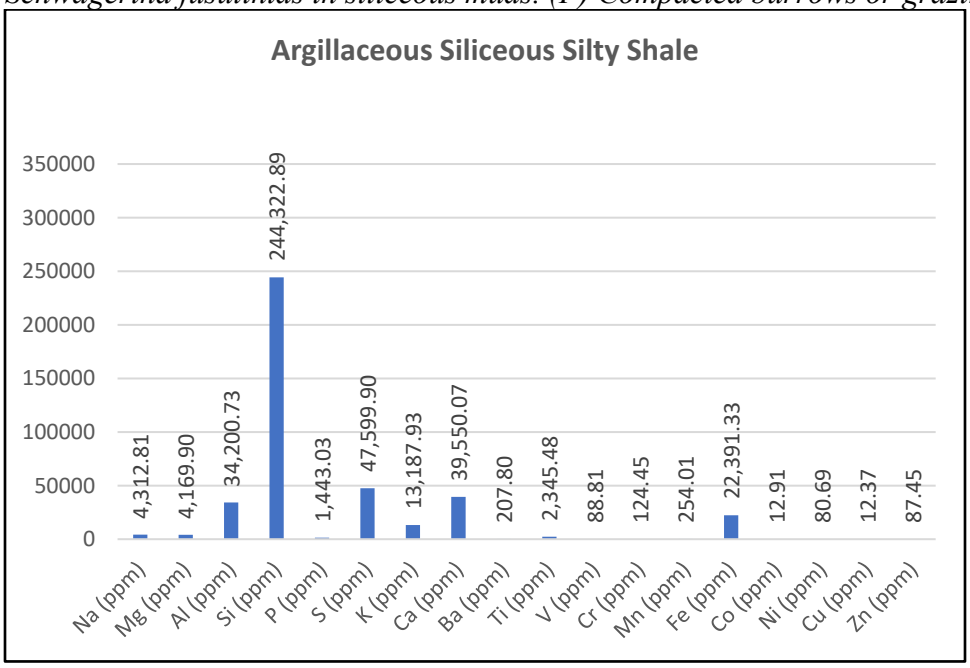

Figure 10: Graph showing average elemental abundances in parts per million for argillaceous siliceous silty shale Facies.

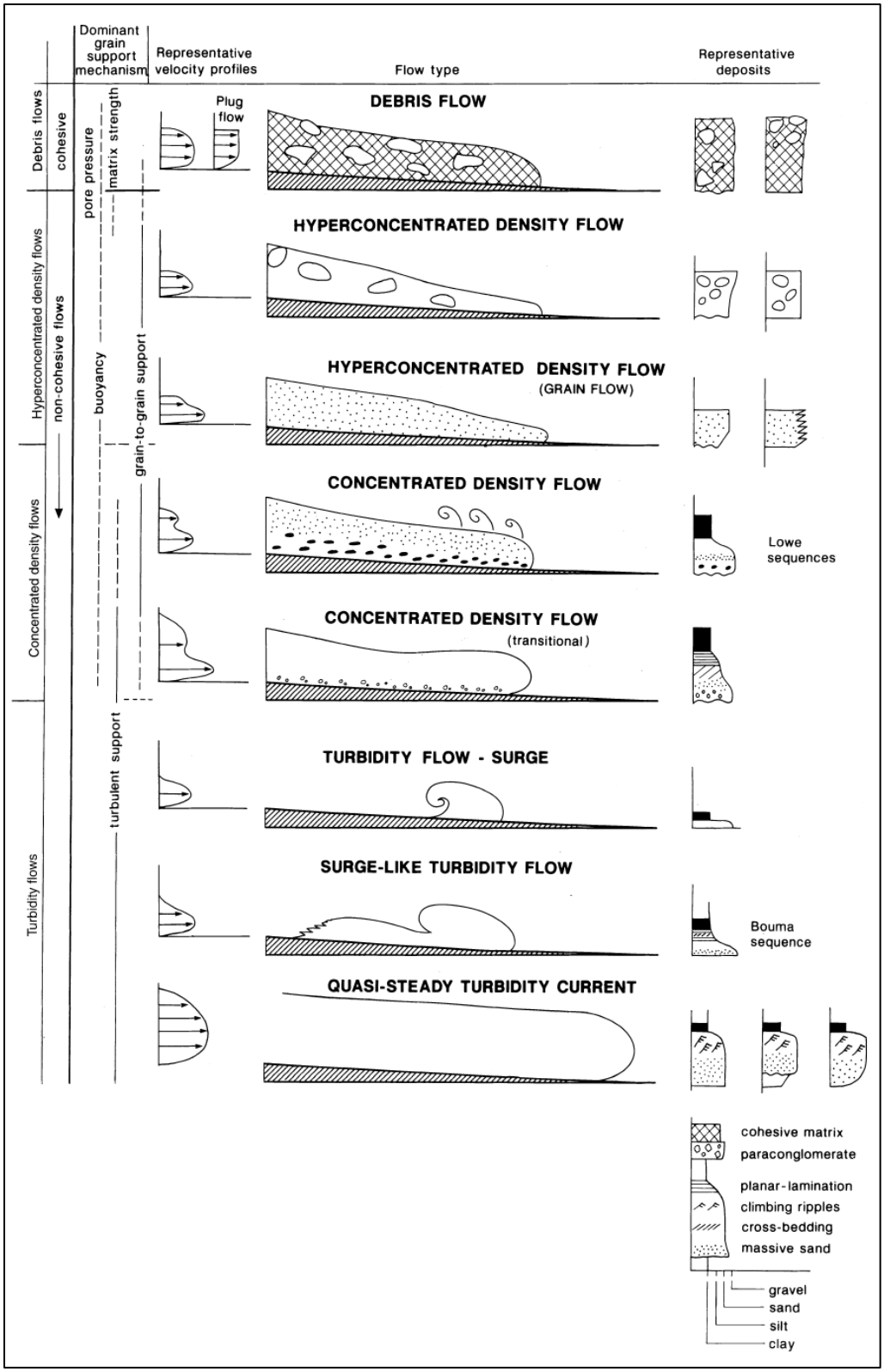

Figure 11:Subaqueous Sedimentary Density Flows and their Deposits from Mulder et. al., 2001.

Interbedded Laminated Calclithite and Argillaceous Siliceous Silty Shale

This facies was the second most abundant and is a mix of interbedded clay and silica rich shales, calclithite, and micrite mud. Characteristic images of the facies at both core and thin section scale can be seen in Figures 12 A through H and 13 A through F. The facies is slightly less silica and clay rich overall and slightly more calcite rich than the argillaceous siliceous silty shale. Based on 15 XRD measurement points, the facies on average was 46.9% quartz, 0.2% k-feldspar, 5.1% plagioclase, 1.7% apatite, 2.7% pyrite, 14.6% calcite, 3.0% dolomite, and 25.7% clay minerals. XRF averages show the facies to be silica rich with slightly more elevated carbonate associated elements (Figure 14) than the argillaceous siliceous silty shale facies. Horizontal fractures, larger subvertical fractures, ferroan dolomite, framboidal pyrite, and euhedral pyrite are present.

Fossils were larger and more abundant than in the argillaceous siliceous silty shale facies. Most common fossils were silt to coarse sand sized echinoderms, crinoids, brachiopods, fusulinids, sponge spicules, and peloids (Figure 13 A and D). Smaller radiolaria and calcispheres were also present. Bryozoans, and algae were rare (Figure 13E and 13F).

The most common sedimentary structures are planar, rippled, wavy, and flaser bedding (Figure 12A-C). Some small fining upward sequences (inch to a couple inches scale) were observed. Some intervals of lenticular laminated muds were observed but were rare (Figure 12F). Carbonate injectites were most common in this facies (Figure 12D and 12H). Burrows were occasionally observed (Figure 12E). Micro laminations of detrital clays, quartz silt, and carbonate material were observed in thin section (Figure 13 B and C). The interbedded laminated calclithite and argillaceous siliceous silty shale is interpreted to be intermittent hemipelagic fallout with more frequent turbidity flows than the argillaceous siliceous silty shale facies.

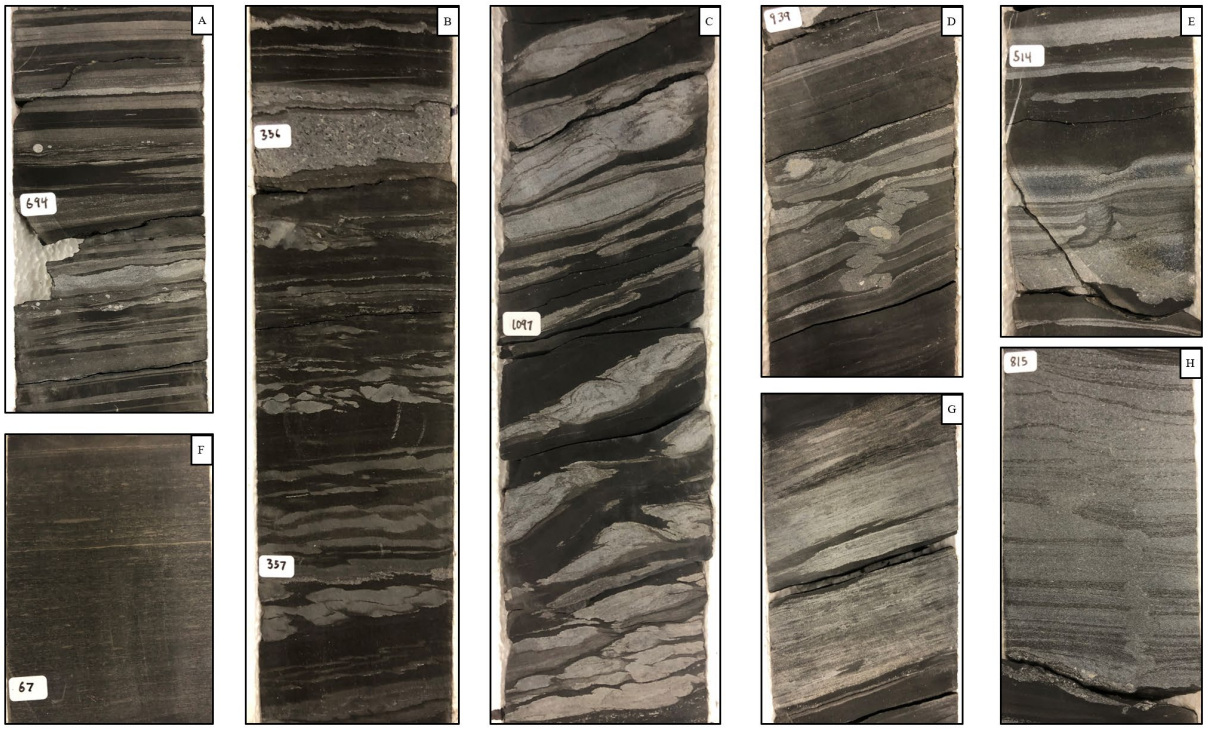

Figure 12: *Core scale sedimentary features of Interbedded Calclithite and Argillaceous Siliceous Silty Shale facies. (A) Planar and ripple laminations of silt and calclithite material. (B) Planar and climbing ripple laminations of silt and carbonate material. Flaser and wavy bedded calclithite also present. There is also evidence for some soft sediment deformation. (C) Flaser and wavy bedded calclithites along with evidence of soft sediment deformation. (D) Injectite of calclithite through planer laminations. (E) Compacted burrow through planar laminations. (F) Lenticular laminated muds interbedded with argillaceous siliceous silty shale (G) Planar and wispy laminated calclithite and shale (H) Injectite through planar laminations with some evidence of soft sediment deformation.*

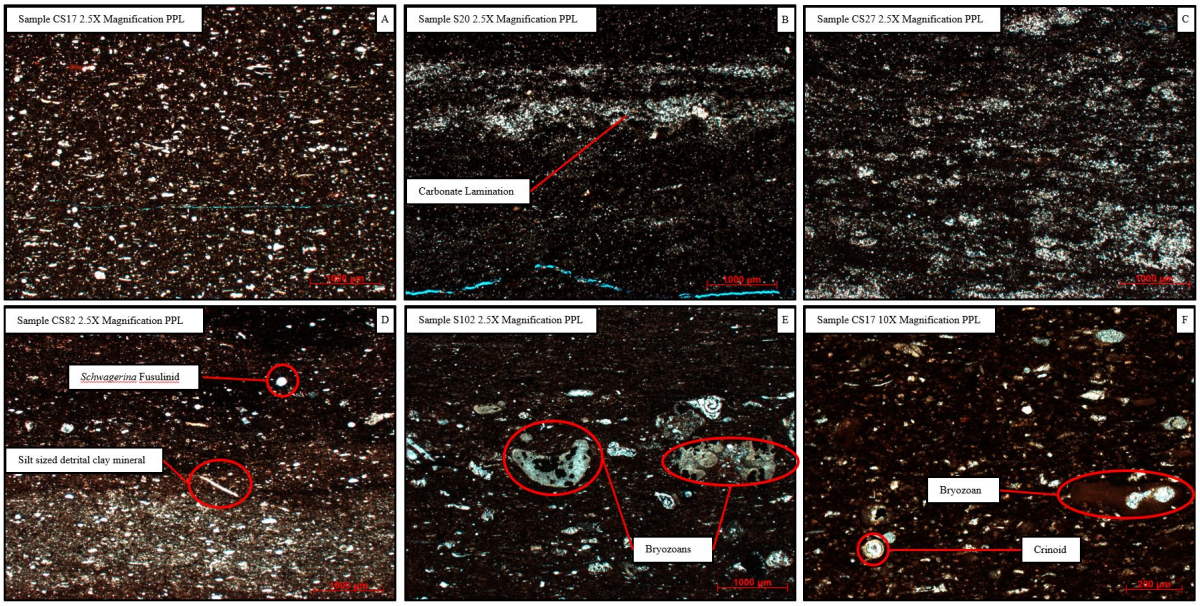

Figure 13: *Thin section scale sedimentary features of Interbedded Calclithite and argillaceous siliceous silty shale facies (A) More abundant silt sized quartz, carbonate allochem, and clays than the argillaceous siliceous silty shale facies. (B) Silt and carbonate allochem rich lamination. (C) Abundant microlaminations of carbonate allochems. (D) Carbonate lamination with fusulinids, spicules, and micrite (E) Carbonate lamination with fusulinids, Pyritized Fistuloporid bryozoans, and brachiopods. (F) Schwagerina fusulinids, brachiopod spines, Fistuloporid bryozoans with mineralized cavities, and sponge spicules in carbonate rich lamination.*

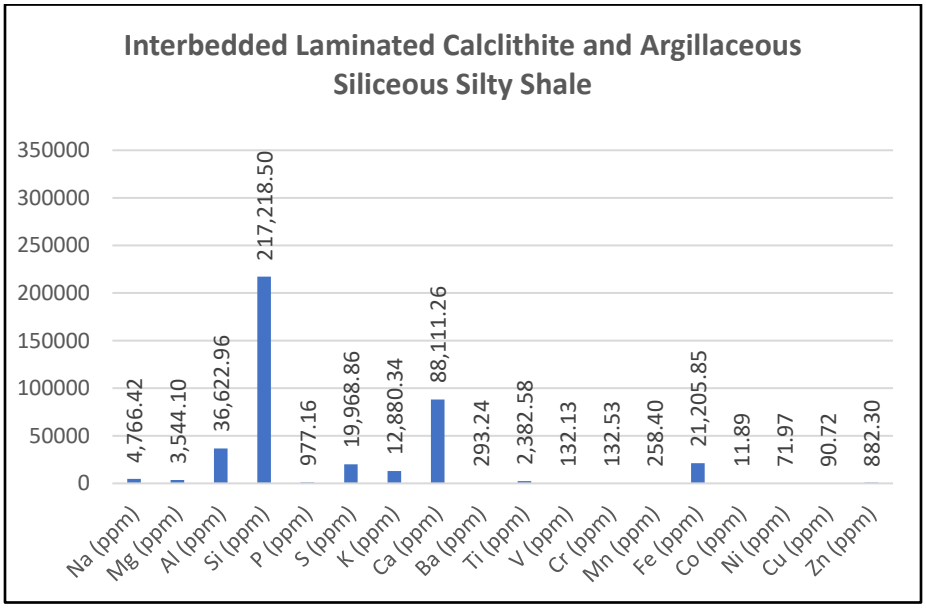

Figure 14: Graph showing elemental abundances in parts per million for Interbedded Laminated Calclithite and Argillaceous Siliceous Silty Shale Facies.

Open-Framework Bioclastic Argillaceous Siliceous Mudstone

The open-framework bioclastic argillaceous siliceous mudstone consists of carbonate allochems in an argillaceous siliceous silty mudstone matrix. Characteristic images of the facies at both core and thin section scale can be seen in Figures 15 A through D and 16 A through F. Based on 2 XRD measurement points, the facies on average consisted of 25.8% quartz, 0.2% k-feldspar, 2.6% plagioclase, 0.4% apatite, 2.0% pyrite, 55.3% calcite, 2.5% dolomite, and 11.2% clay minerals. Based on average elemental abundances (Figure 17), the facies is inferred to be an equal mix of silica rich minerals and more calcium rich minerals. Intraclasts of carbonate material and siliceous muds are also present. Small replaced halite crystals were present in one thin section but were very rare (Figure 16 D).

Fossils were larger, more abundant and more diverse than the interbedded calclithite and argillaceous siliceous silty shale facies. The most common fossils are radiolaria, calcispheres, peloids, fusulinids, echinoderms, crinoids, brachiopods, bryozoans, sponge spicules, gastropods, and algae (Figure 16 A, C, E, and F).

This facies is usually massive or fines upward from thin section scale (Figure 16B) to two and a half feet thick with sharp erosional contacts at the base. Injectites are present but rare (Figure 15B). Intervals of planar laminations and deformed laminations are present at the top of some beds (Figure 15A and 15C). The open-framework bioclastic argillaceous siliceous mudstone is interpreted to be a result of concentrated and hyperconcentrated density flows because of its overall grainsize and massive bedding, sometimes with larger clasts towards the top of flows. Planar laminations toward the top of the facies could reflect density of the flow decreasing as the flow lost energy.

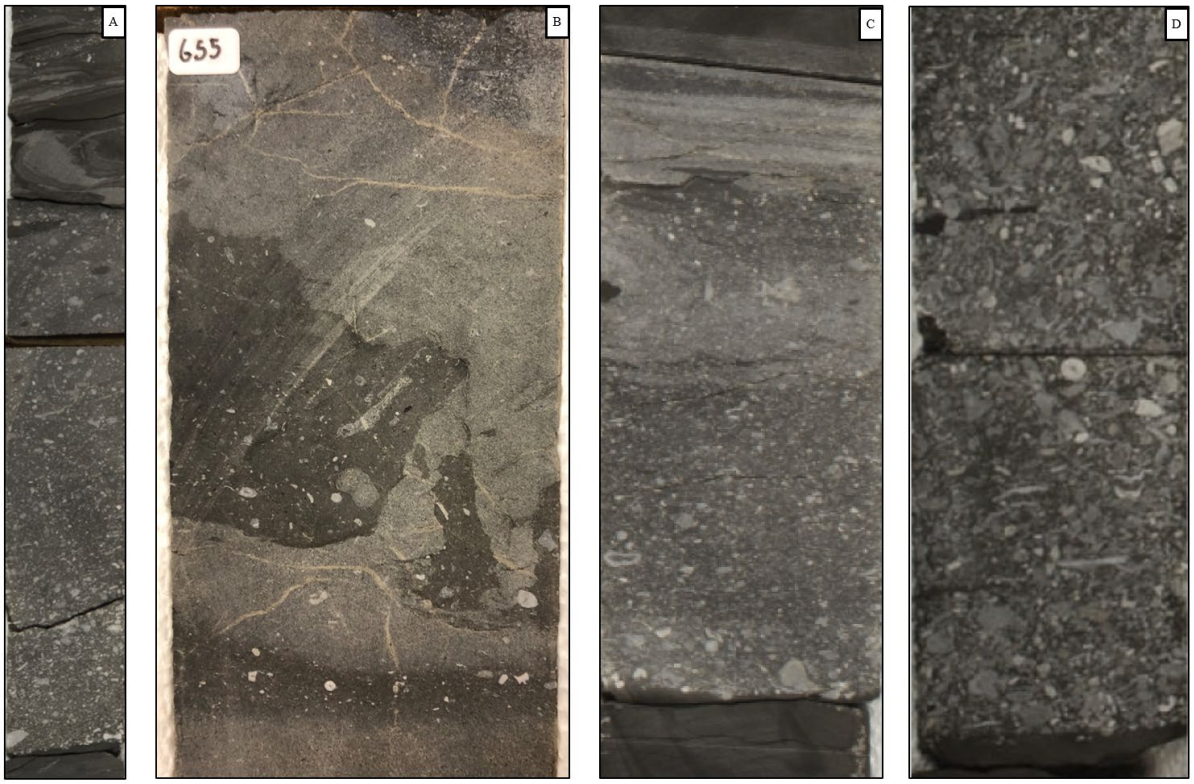

Figure 15: Core scale sedimentary features of Bioclastic Argillaceous Siliceous Silty Mudstone. (A) Characteristic interval of Bioclastic Argillaceous Siliceous Mudstone Facies. Slumped clast of interbedded shale and calclithite present at the top of the bed. (B) Injectites of carbonate rich interval into bioclastic argillaceous siliceous silty mudstone (C) Interval showing slight fining upward sequence and planar laminations (D) Interval showing pebble sized crinoids, brachiopods, and carbonate extraclasts in siliceous mud matrix.

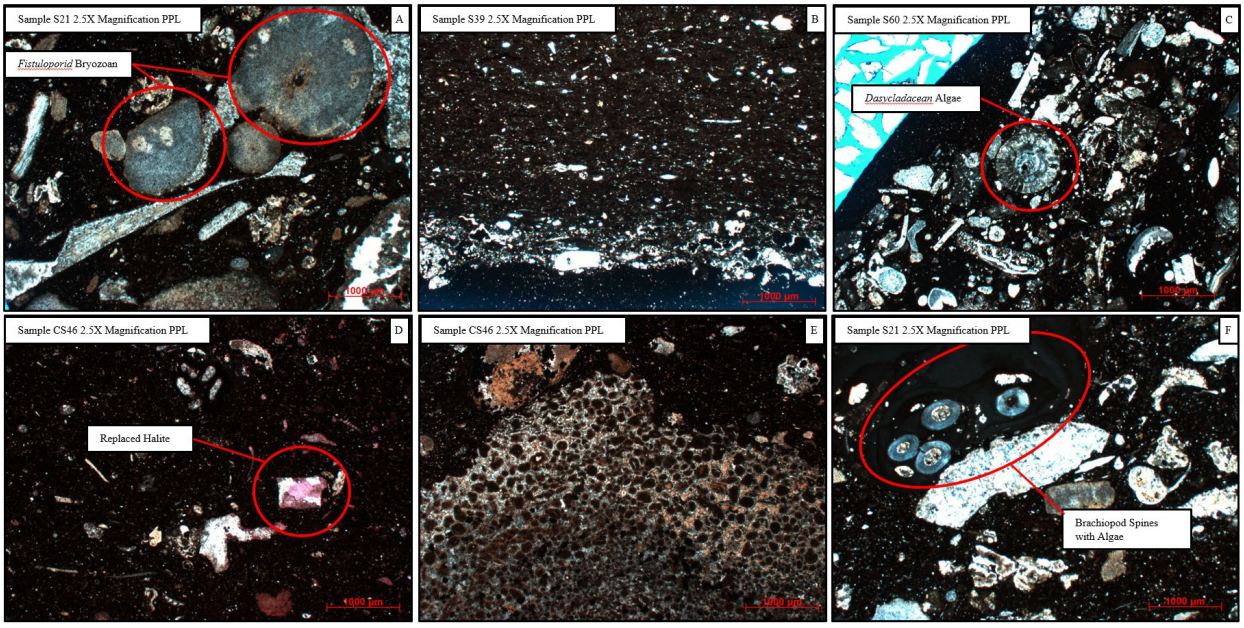

Figure 16: *Thin section scale sedimentary features of Open-framework bioclastic argillaceous siliceous mudstone facies (A) Large Fistuloporid bryozoans in siliceous mud matrix. Large mineralized bivalve also present (B) Fining upward sequence and coarser grained erosive flow base (C) Dasycladacean algae and other carbonate allochems. (D) Replaced halite crystal (E) Intraclast within flow. Intralcast has abundant ooids and coated grains. (F) Brachiopod spines with encrusting algae.*

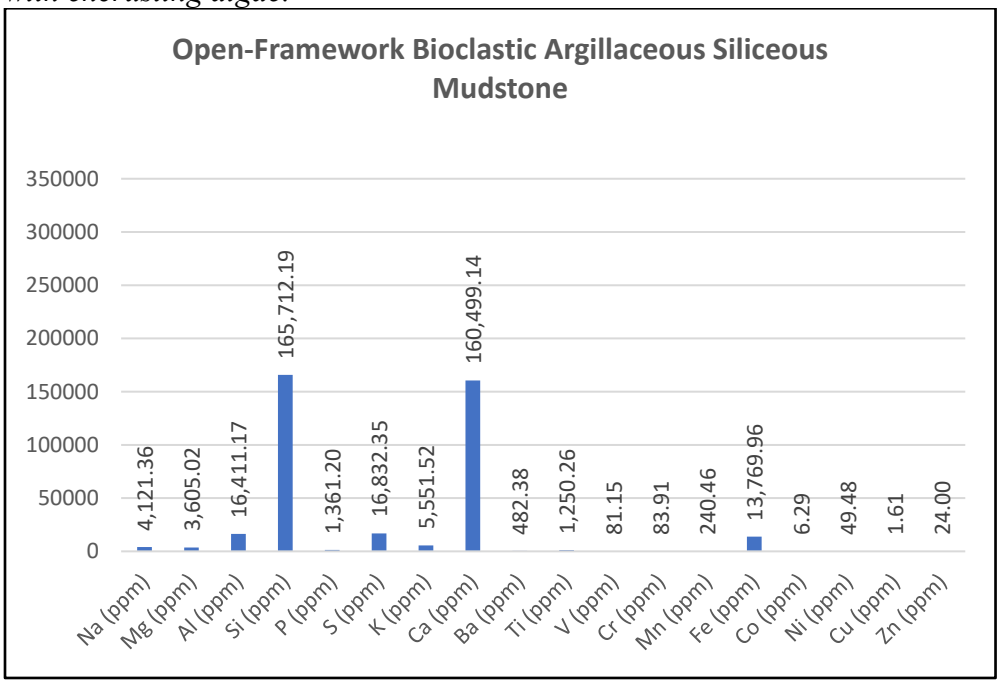

Figure 17: Graph showing elemental abundances in parts per million for Open-framework bioclastic argillaceous siliceous mudstone Facies.

Crinoid Brachiopod Bryozoan Wackestone and Packstone

This facies was observed to be carbonate allochems in carbonate micrite mud. Characteristic images of the facies at both core and thin section scale can be seen in Figures 18 A through E and 19 A through F. Based on 7 XRD measurement points, the facies on average consisted of 17.0% quartz, 0.2% k-feldspar, 1.9% plagioclase, 0.7% apatite, 1.3% pyrite, 70.4% calcite, 3.3% dolomite, and 5.2% clay minerals. Based on average elemental abundances (Figure 20), the facies is inferred to be dominantly calcite with some quartz.

Carbonate fossils were diverse and abundant. The most common are echinoderms, crinoids, brachiopods, bivalves, bryozoans, and sponge spicules (Figures 19 A-E). Less common were dasycladacean algae, tubiphytes algae, and cephalopods (Figure 19B and 19C). Fusulinids, radiolaria, and calcispheres were less common than observed in the other facies.

Beds are massive with high angle, erosive contacts at the base (Figure 18A-D). Some intervals were heavily pyritized and fractured. Some larger gravel sized intraclasts were also present (Figure 18B). Certain intervals in the facies also contained oil-stained open porosity (Figure 18E and 19E). The facies is interpreted to be a result of concentrated and hyperconcentrated density flows because of its overall grainsize and massive bedding.

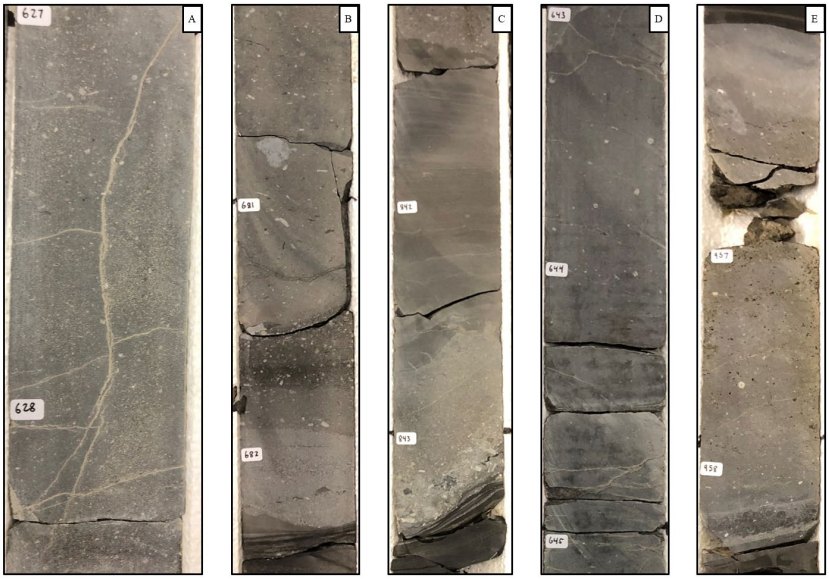

Figure 18: Core scale sedimentary features of crinoid brachiopod bryozoan wackestone and packstone (A) Massive bedding with carbonate allochems in micrite matrix (B) Interval showing mud rich lamination, pebble sized intraclast, and small compacted burrows (C) Interval showing high angle contact, coarse grained erosive base and slight laminations. (D) Massive bedding with gravel sized crinoids. (E) Interval showing dark colored oil stained porosity.

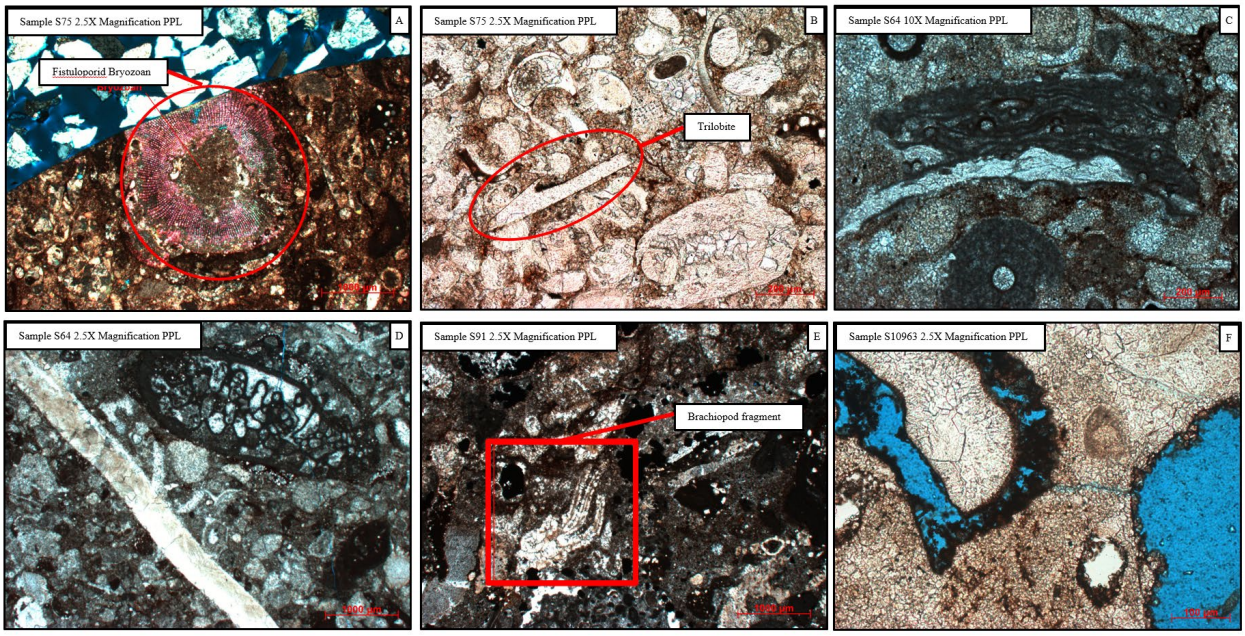

Figure 19: *Thin section scale sedimentary features of crinoid brachiopod bryozoan wackestone and packstone facies (A) Large Fistuloporid bryozoans in micrite mud matrix. (B) Abundant carbonate allochems in micrite mud. trilobite fragment highlighted. (C) Bivalve with encrusting Tubiphytes algae. (D) Large Schwagerina fusulinid and brachiopod fragment. (E) Large more*

intact brachiopod. Also note large amount of black euhedral pyrite(F) Oil-stained open porosity in sparry calcite.

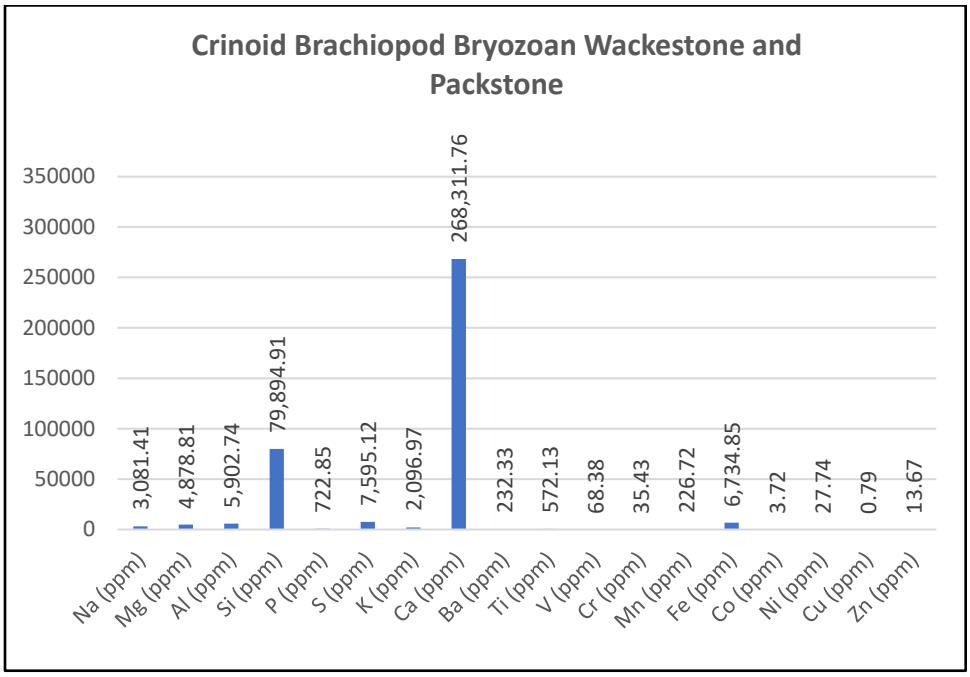

Figure 20: Graph showing elemental abundances in parts per million for crinoid brachiopod bryozoan wackestone and packstone Facies.

Oligomictic Limestone Extraclast Paraconglomerate

The facies is the second least abundant and consists of cobble to gravel sized fragments of platform and basinal material with smaller carbonate allochems in a mix of lime mud and argillaceous siliceous silty mudstone matrix. Cobble sized clasts tend to be either heavily cemented wackestones and packestones with abundant fossils or rounded clasts of interbedded laminated shale and carbonate. Characteristic images of the facies at both core and thin section scale can be seen in Figures 20 A through F and 21 A through F. The matrix tends to be slightly more micrite rich compared to clay rich. No XRD points were taken from this facies, however based on XRF data taken through the facies (Figure 23), the mineralogy is inferred to be in between that of the Crinoid Brachiopod Wackstone/Packstone and the Open Framework

Bioclastic Siliceous Argillaceous Silty Shale, with carbonate allochems and a mix of both siliceous and calcareous mud matrix.

Fossils in this facies were much larger and more coherent than in the previously mentioned crinoid brachiopod bryozoan wackestone and packstone facies. Fossils observed in this facies were fusulinids, echinoderms, crinoids, brachiopods, bivalves, dasycladacean algae, bryozoans, red algae, tubiphytes algae, gastropods, and cephalopods (Figures 21C, 22B, and 22D). In one of the extraclasts, ooids were observed.

The facies tends to be massively bedded and sometimes fines upward, and contained extraclasts up to eight cm in diameter and intraclasts up to four cm in diameter (Figure 21A-F). Extraclasts were from a variety of different platform environments and contained multiple generations of cements (Figures 22C and 22F). The interbedded carbonate and shale intraclasts were rounded and showed evidence for soft sediment deformation (Figure 21E). The oligomictic limestone extraclast paraconglomerate is interpreted to be a result of debris flows. This process interpretation is supported by the massive habit and large clast size of the facies. The larger extraclasts compared to intraclasts reflect the relatively higher energy as the flow began.

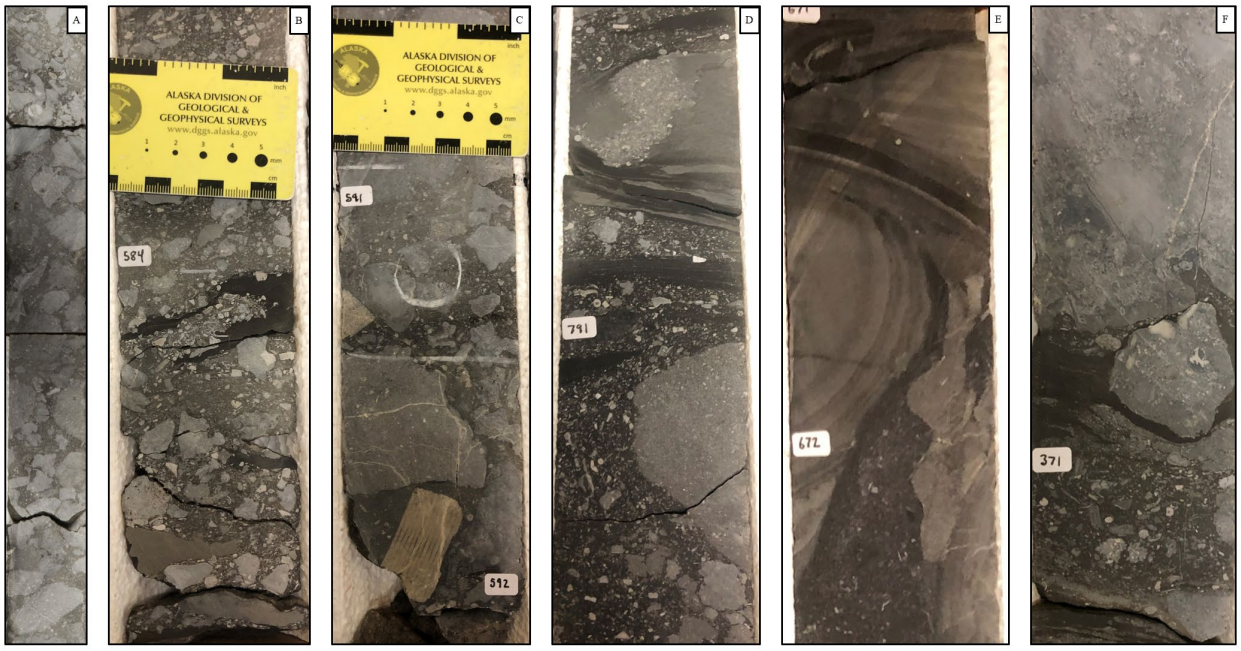

Figure 21: Core scale sedimentary features of the oligomictic limestone extraclast paraconglomerate. (A) Interval showing large cobble sized transported pieces of the Central Basin Platform. (B) Deformed shale clast and cobble sized extraclasts. (C) Large extraclasts and large crinoid (D) Large cobble sized intraclasts and shale clasts (E) Cobble sized laminated intraclast (F) Cobble sized extraclast in siliceous mud rich interval.

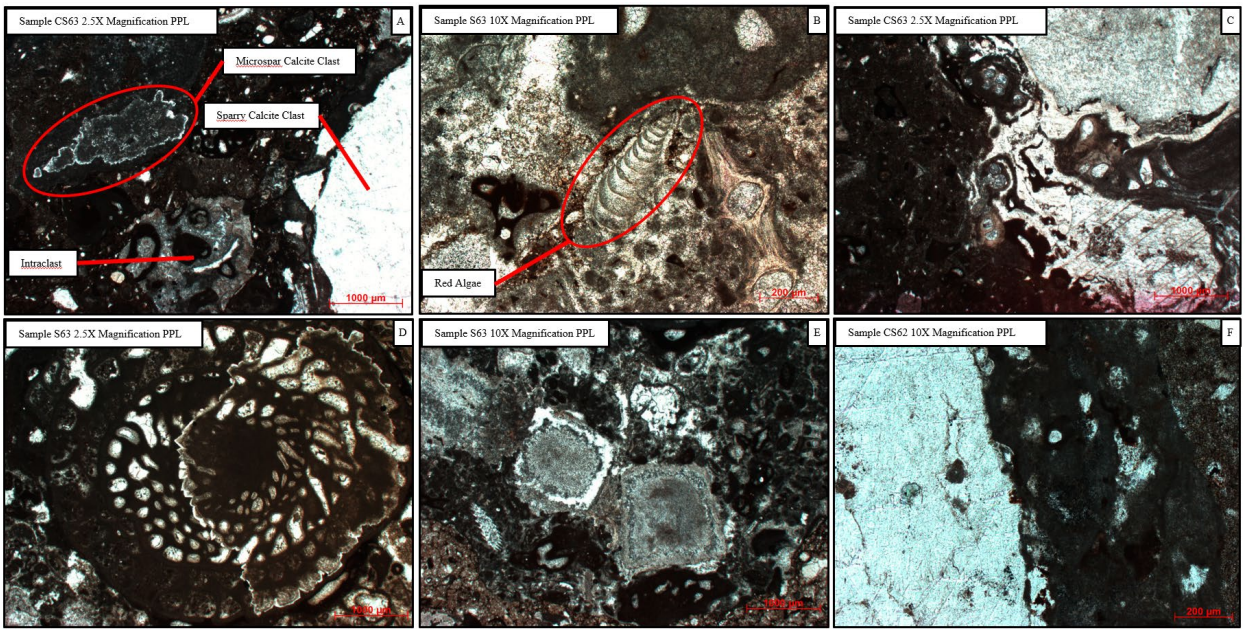

Figure 22: *Thin section scale sedimentary features of oligomictic limestone extraclast paraconglomerate Facies (A) Large sparry calcite clast, smaller microspar calcite clast, and intraclast. (B) Red algae and large Fistuloporid bryozoans. (C) Twinned calcite and*

Fistuloporid bryozoans. (D) Schwagerina fusulinid with partial dolomitization. (E) Calcite and silica replaced halite crystals. (F) Sparry calcite clast with encrusting Tubiphytes algae on the surface.

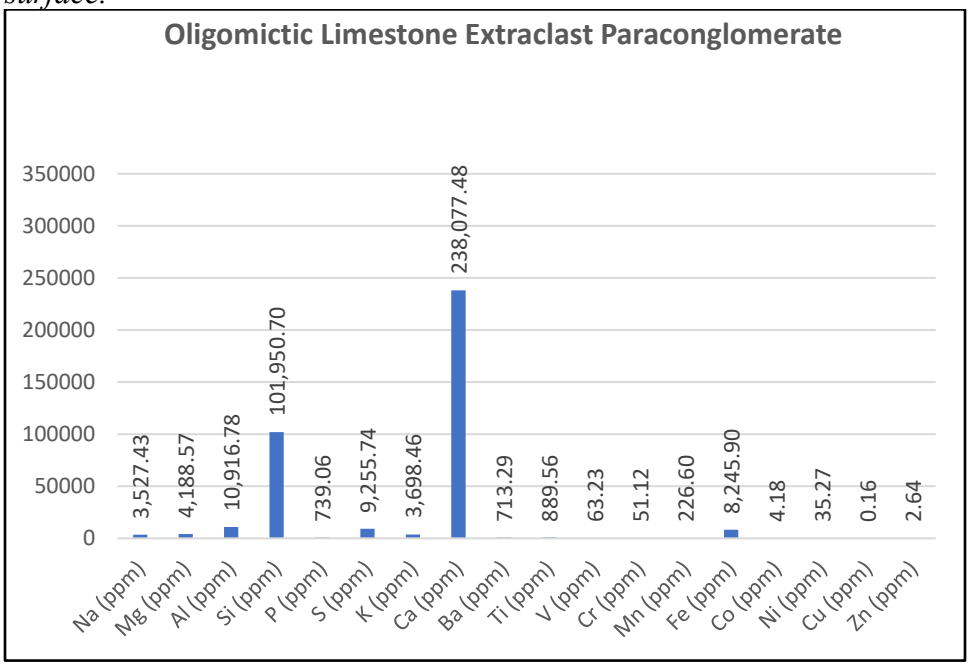

Figure 23: Graph showing elemental abundances in parts per million for oligomictic limestone extraclast paraconglomerate Facies.

Calcite Cemented Fine Grained Arkose

This facies was the least common in the cored interval, appearing only once (Figure 24A and 24B). It contains fine sand sized quartz and albite grains with sparry calcite cement. The sandstone has convolute and overturned laminations. There were no XRD samples from this interval, but based on the XRF and hand sample observation, the mineralogy is inferred to be dominantly quartz, albite, and calcite due to the abundance of Na, Si, and Ca (see Figure 25). The calcite cemented fine grained arkose is likely a result of either a small turbidity current or it was incorporated into a larger flow.

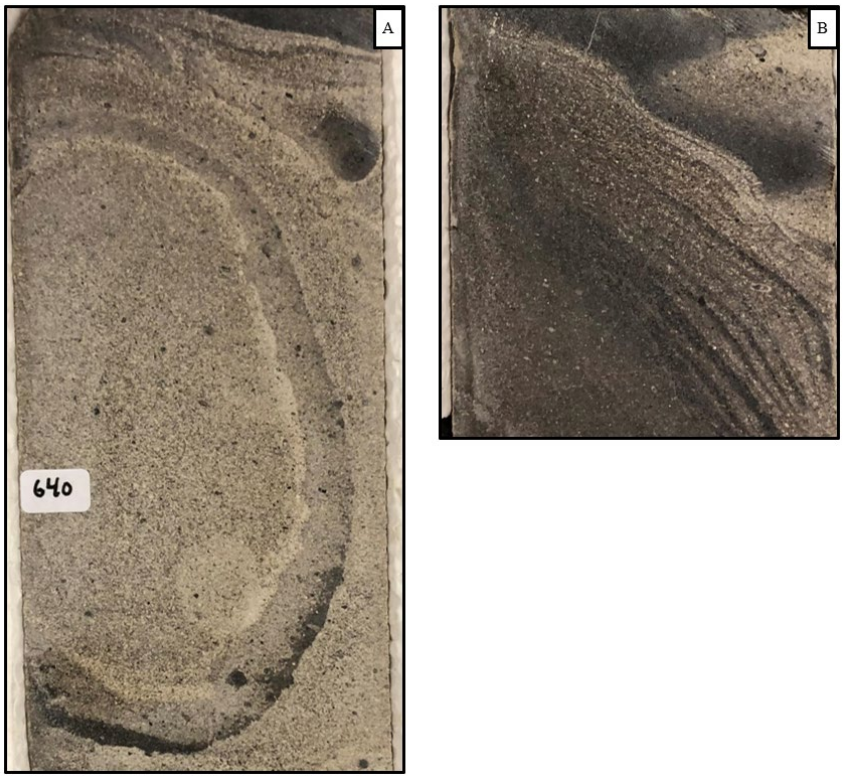

Figure 24: Core scale sedimentary features of the calcite cemented fine grained arkose. (A) Interval showing laminated fine sands. Interval could be either soft sediment deformation or a concretion. (B) Interval showing deformed laminations of fine sand. Note white albite grains.

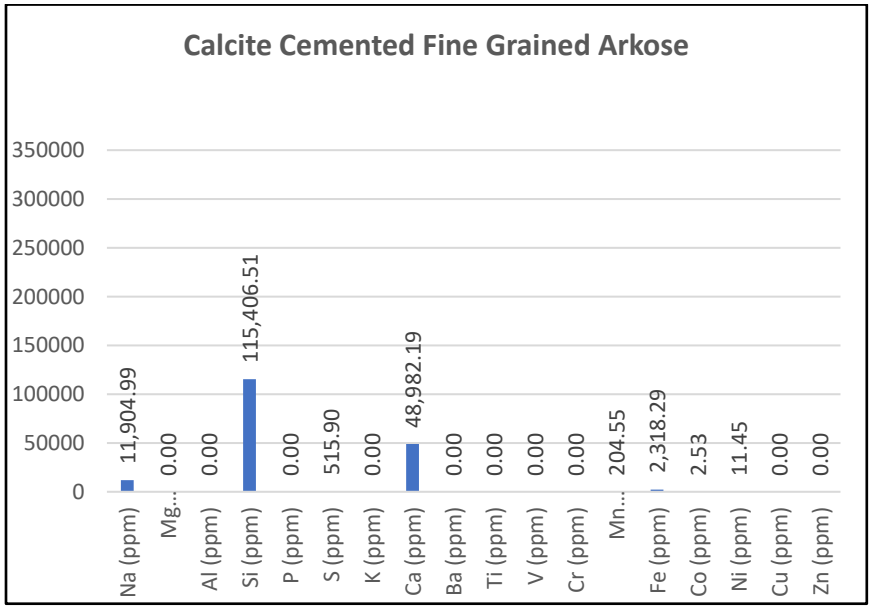

Figure 25: Graph showing elemental abundances in parts per million for calcite cemented fine grained arkose Facies.

Chemofacies

Using the elbow graph shown in Figure 26 it was determined that 4 clusters would be used to run the hierarchical clustering. A dendrogram showing how the facies were clustered is shown in Figure 27. Average elemental abundances for each chemofacies are shown in table 4. Logs generated from XRF for elemental abundances and chemofacies can be seen in Figure 46.

Chemofacies 1 was the most abundant with 463 measurement points. Chemofacies 2 was the second most abundant with 294 measurement points. Chemofacies 3 was the third most abundant with 226 measurement points. Chemofacies 4 was the least abundant with 145 measurement points.

Chemofacies 1 and 2 are generally from shale rich intervals. The abundance of the elements Si, Na, Al, and K (table 4) within chemofacies 1 and 2 can be explained by minerals within the shales such as detrital quartz and albite, as well as clay minerals. Chemofacies 3 and 4 are generally from calclithite intervals. These chemofacies are abundant in Ca and Mg (table 4) sourced from calcite and dolomite.

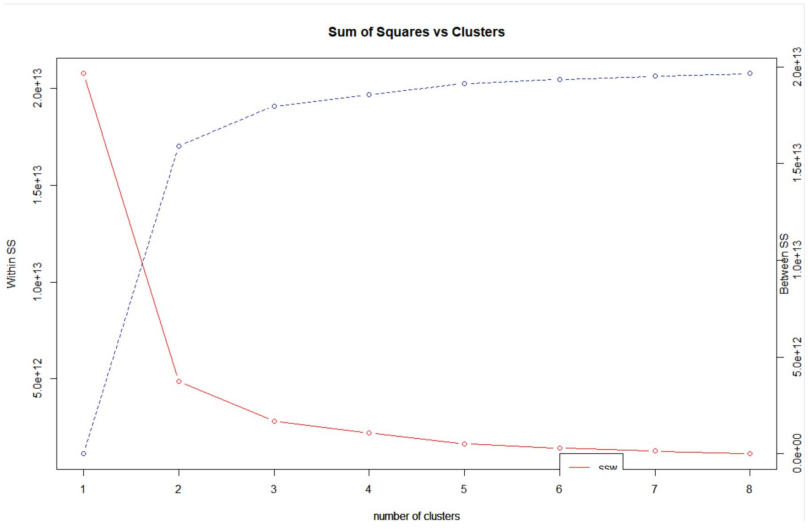

Figure 26: Elbow graph for XRF clustering. Number of clusters in the X axis and error in the Y axis.

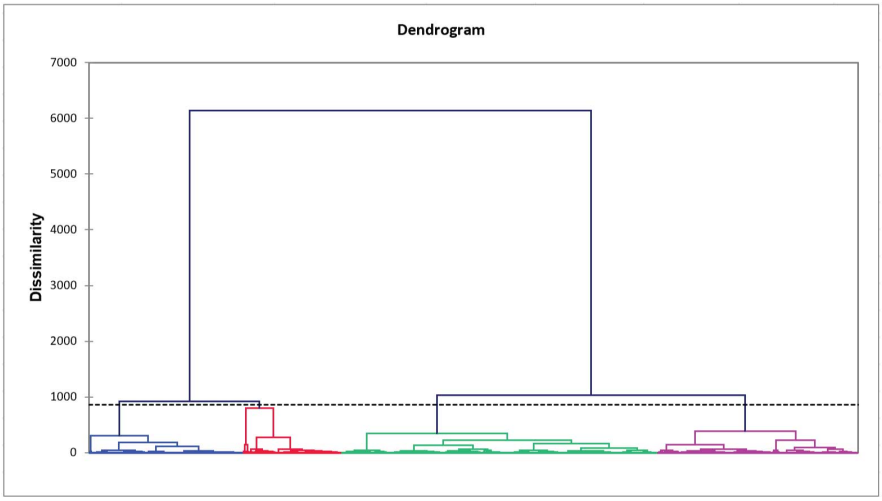

Figure 27: Dendrogram for XRF data showing the clustering for 4 chemofacies.

Table 4: Average elemental abundances for Chemofacies.

Class	Na (ppm)	Mg (ppm)	Al (ppm)	Si (ppm)	P (ppm)	S (ppm)	K (ppm)	Ca (ppm)	Ti (ppm)	V (ppm)	Fe (ppm)	Ni (ppm)	Mo (ppm)
1	3815.00	4891.12	36359.68	240467.08	1238.96	57767.82	14073.35	36364.60	2506.43	76.38	23630.92	78.01	20.48
2	5627.63	2172.10	34244.69	253463.07	810.28	24191.99	12592.22	39033.79	2269.51	114.40	20800.56	85.90	24.95
3	2911.92	4967.64	3774.12	69622.66	822.31	5399.19	1212.20	284889.94	443.26	68.98	6774.89	23.64	1.52
4	4161.61	3865.57	17022.00	185994.46	5198.08	14147.10	5607.21	146249.21	1273.83	97.70	14343.25	50.99	10.50

Reservoir Properties

Logs showing gamma ray, relative geomechanical measurements, total organic carbon (TOC), porosity, and saturations are displayed in Figure 28. The more shale rich intervals had higher gamma ray values and the carbonate rich intervals had lower gamma ray values. The shale rich intervals were mechanically weaker than the more carbonate rich intervals within the core. TOC, porosity, and oil saturation are all higher above in the upper part of the core above 10750ft.

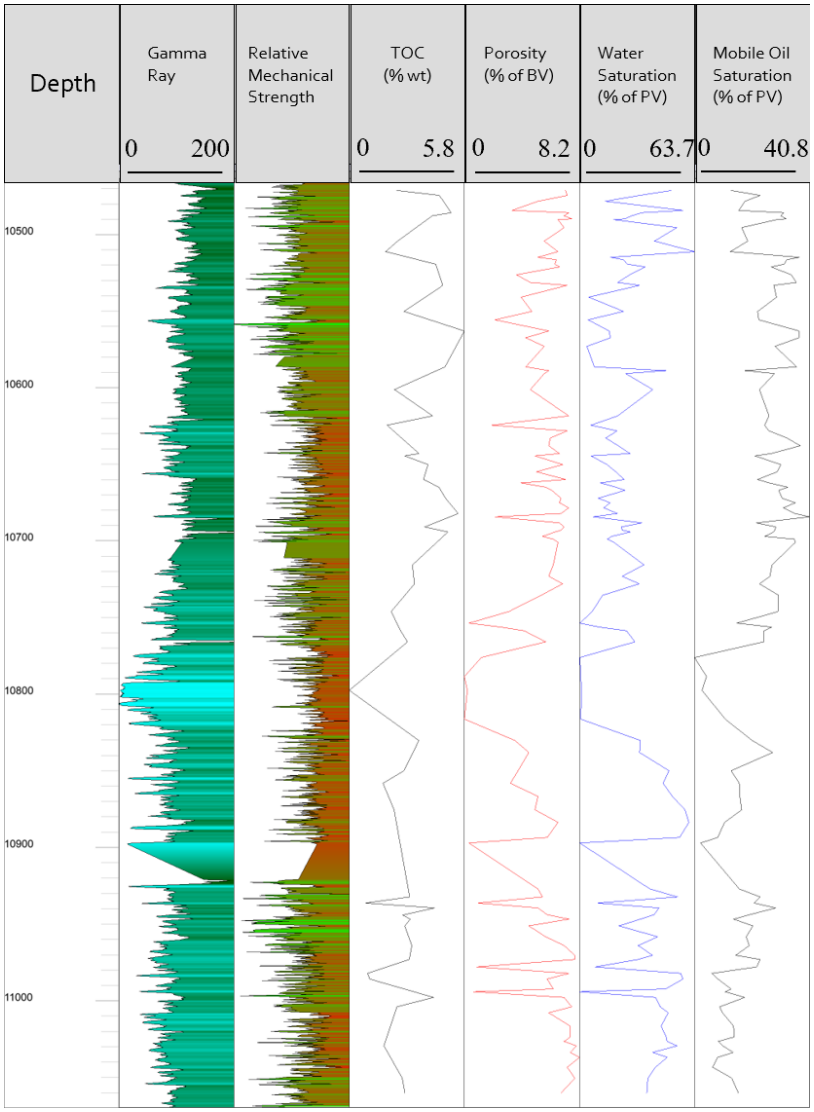

Figure 28: Logs for reservoir properties; Gamma ray, relative mechanical strength (green being weaker and red being stronger), TOC (%), porosity (% of BV), sater Saturation (% of PV), and mobile oil saturation (% of PV).

Diagenesis

Within the cored interval three different paragenetic sequences were constructed (Figures 29-32); one in the upper portion of the core, one in the lower portion of the core, and one within the carbonate interval towards the middle of the core.

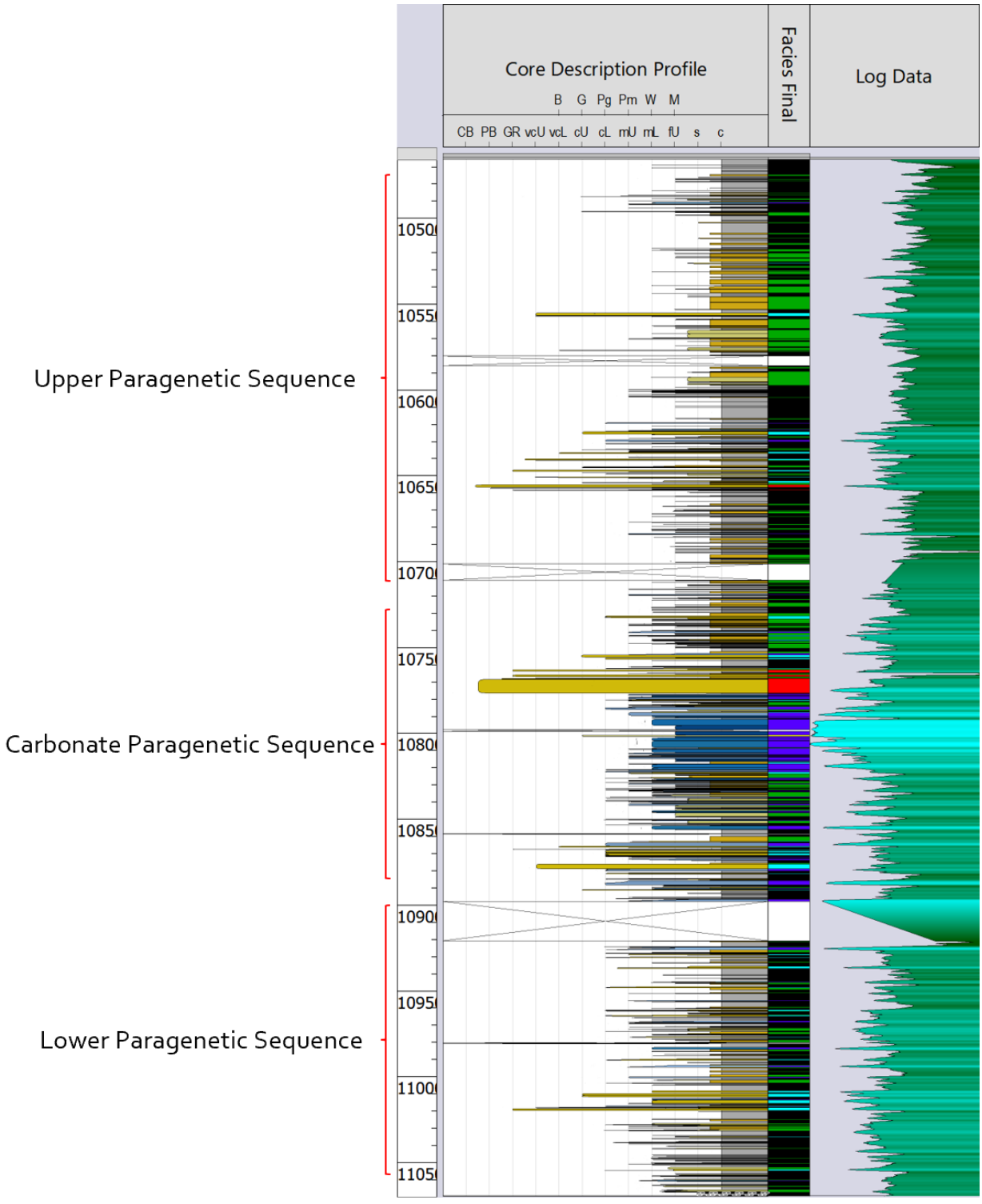

Figure 29: Stratigraphic column showing approximate depths for three paragenetic sequences.

Figure 30: Paragentic sequence for shale rich sediments above the submarine fan.

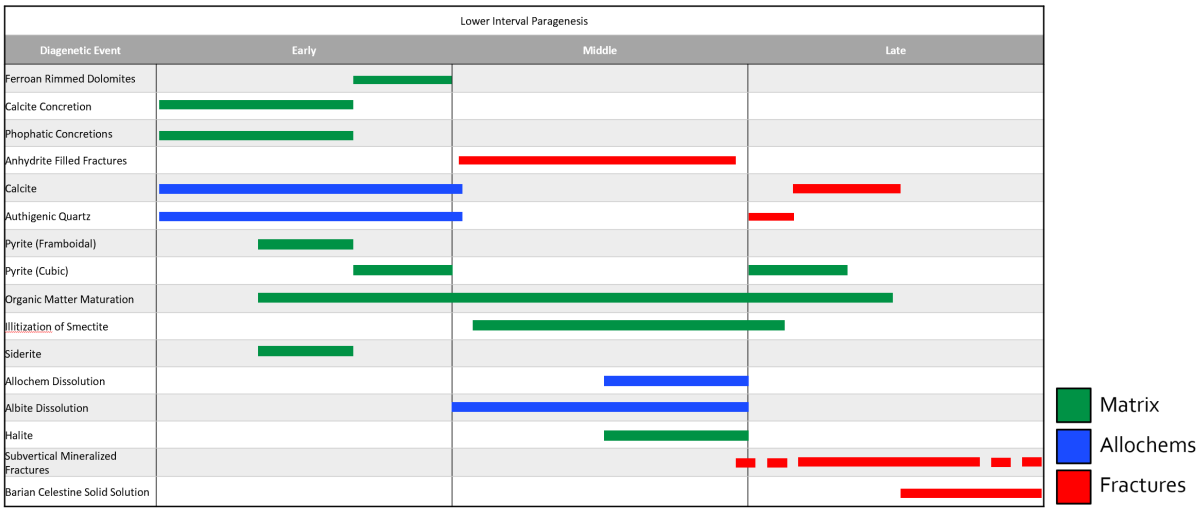

Figure 31: Paragentic sequence for shale rich sediments below the submarine fan.

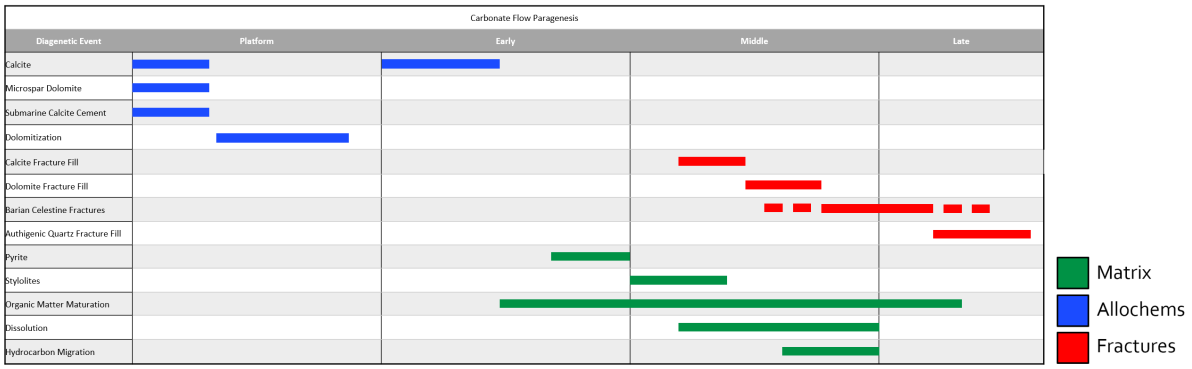

Figure 32: Paragentic sequence for carbonate rich sediments in the submarine fan.

Early Diagenesis

Early diagenesis of the two, shale rich paragenetic sequences, is very similar (Figs. 30 and 31). The rocks have many components that would be reactive during early diagenesis such as, organic matter, biogenic quartz, high magnesium calcite, and aragonite which could source early mineral phases. Framboidal pyrite is persistent throughout both the upper and lower intervals (Figure 33A and B) and range in size from 1 to 10 um with and clusters of framboids were anywhere from 15-70 um in size. Clusters of framboids also contained intracrystalline organic matter. The framboids are interpreted to be a result of early sulfate reduction when soluble ferrous iron ions were readily available (Hesse and Schacht, 2011). Silt sized detrital and authigenic quartz is present throughout (Figure 33A). Amorphous chert, quartz, calcite and dolomite replaced radiolarians, calcispheres, sponge spicules, and other calcite allochems during early diagenesis (Figure 35A and B). Concretions of calcite, pyrite, siderite, and phosphates have a pre-compactional texture, with clay minerals deforming around them (Figure 36 A and B). They are interpreted to be early diagenetic in origin. Calcite and siderite concretions were most likely related to early degradation of organic matter which provided the carbon needed for the reaction in the oxidation and nitrate-reduction zones (Hesse and Schacht 2011). Pyrite and phosphatic concretions likely occur during sulfate reduction (Hesse and Schacht. 2011). Authigenic and detrital ferroan rimmed dolomites are present throughout (Figures 33B and 34). Detrital ferroan rimmed dolomites show some rounding in both the rims and Mg rich cores, while the authigenic dolomites have euhedral crystals. Authigenic dolomites were likely organogenic dolomites which are common in interbedded shales and gravity flows (Hesse and Schacht, 2011). The iron poor centers of the dolomite probably crystallized during sulfate-reduction when iron was being incorporated into other mineral phases such as siderite and pyrite.

Then when iron became more available during the carbonate-reduction phase, the ferroan rims on both the authigenic and detrital dolomites formed. Larger euhedral pyrite began to form toward the end of early diagenesis through to late diagenesis as the system began to close off from the seawater above.

In the carbonate flows there is evidence of diagenetic alteration from platform processes before transport into the basin. Submarine calcite cements (Figure 37C), microspar calcite (Figure 37A), halite, and microdolomites (Figure 37B) were all present within the carbonate flows. After transport from the platform through gravity driven flow and deposition, early diagenetic phases in the basin include chert, calcite, quartz, and euhedral pyrite.

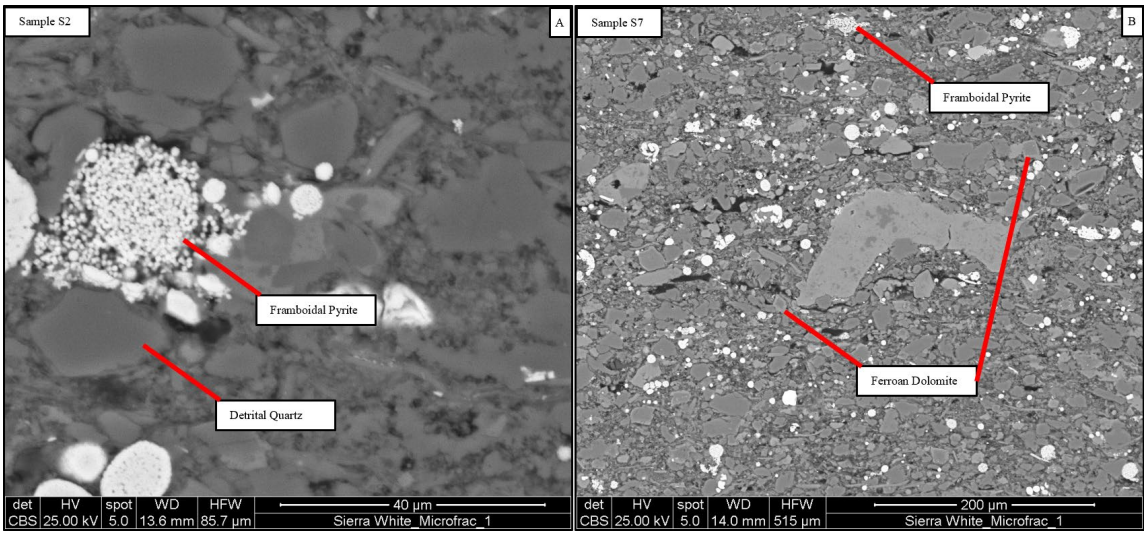

Figure 33: (A) Backscatter photomicrograph showing framboidal pyrite cluster with intracrystalline organic matter. Also, detrital subangular quartz. (B) Dispersed framboidal pyrite and ferroan dolomite in mud matrix.

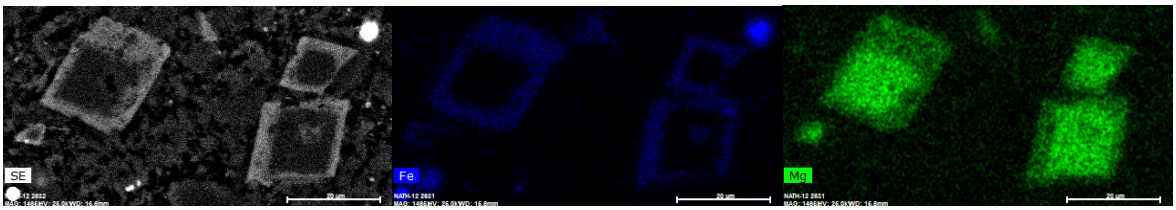

Figure 34: Backscatter photomicrograph of ferroan rimmed dolomite with EDAX elemental mapping of Fe in blue and Mg in green.

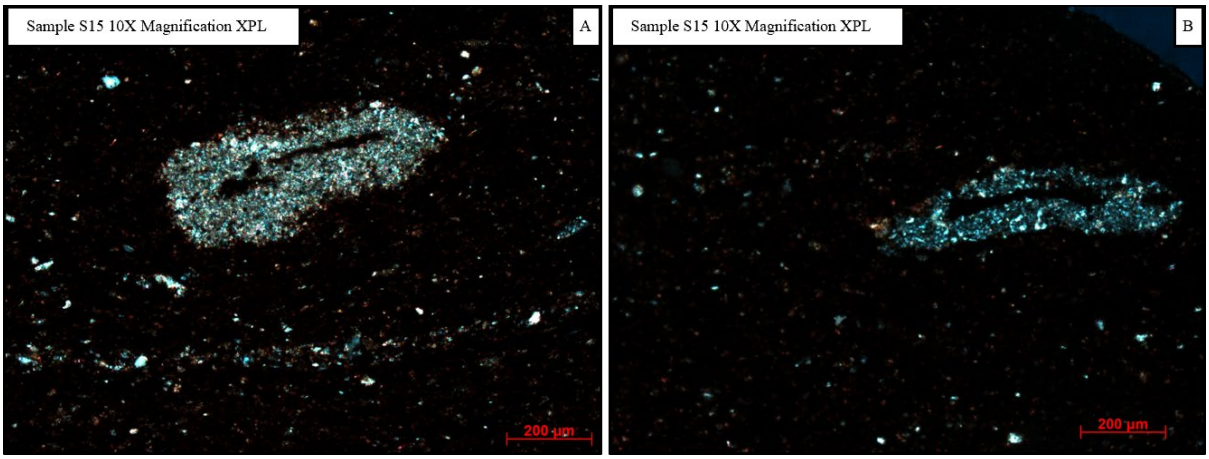

Figure 35: Photomicrographs showing replaced allochems (A) Calcite allochem with organic matter in center (B) Chert allochem with organic matter in the center.

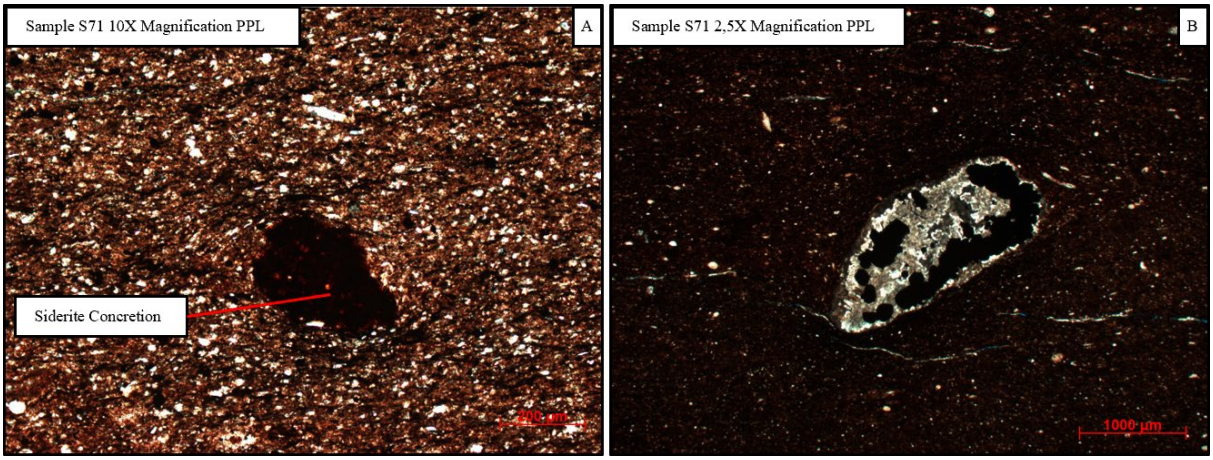

Figure 36: Photomicrographs showing concretions (A)Siderite concretion with alteration of mud matrix (B) Calcite concretion with euhedral pyrite.

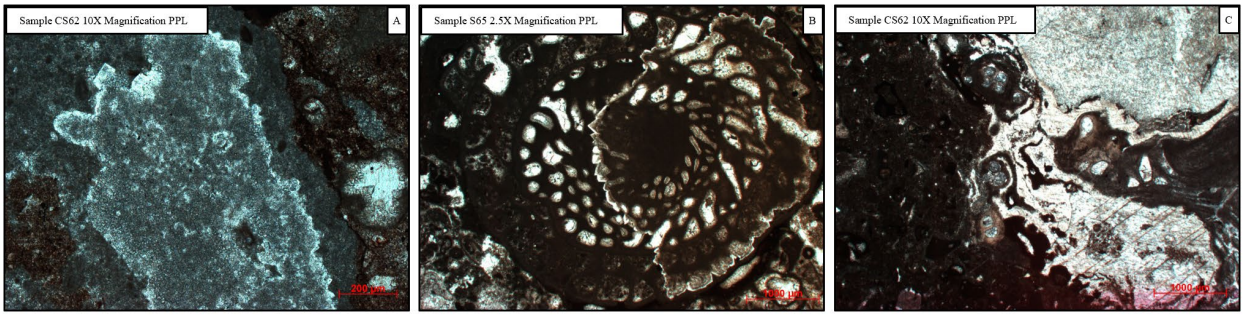

Figure 37: Photomicrographs showing platform diagenesis (A) Microspar calcite allochem (B) Partially dolomitized Schwagerina Fusulinid (C) Twinned calcite cement next to sparry calcite.

Middle Diagenesis

During middle diagenesis is when the shale rich paragenetic sequences start to differentiate. Middle diagenesis is primarily sourced from fluids and minerals within the system. Toward the end of middle diagenesis the system opens to outside fluids as larger conduits form.

In the shale rich intervals there is dissolution of some allochems and mobilization of calcite rich fluids. In the carbonates this causes some moldic porosity (Figure 38) which is coated in hydrocarbons similar to what was observed by Wickard et. Al. (2016). This oil-stained porosity was sometimes next to less mature organic matter within the carbonate flows suggesting the hydrocarbons within the flows was externally sourced from the shale rich intervals.

XRD shows dominantly illite clays within the core. The smectite to illite conversion releases fluids rich in Si, Na, Ca, Mg and Fe (Coniglio and James, 1988; Freed and Peacor, 1989; Lumsden, 1988; Sivalingam, 1990) which likely contributed to the overpressuring of the system. These fluids also contribute to the formation of chert, calcite fracture fills, and later authigenic ferroan dolomite formation.

Toward the end of middle diagenesis in the upper sequence, horizontal fractures formed and were filled with “beef” calcite (Cobbold et al., 2013) and contain hydrocarbons (Figures 39A and 40A). In the lower sequence, horizontal fractures were filled with fibrous “beef” anhydrite and hydrocarbons (Figures 39B and 40B). Halite is also found within the lower sequence in middle to late diagenesis (Figure 41). The anhydrite and halite is inferred to be sourced from outside the Upper Wolfcamp. The horizontal and open fractures in the core may be related to

overpressuring (Cobbold et. al., 2013). These fractures mark the start of the larger system beginning to open to external fluids.

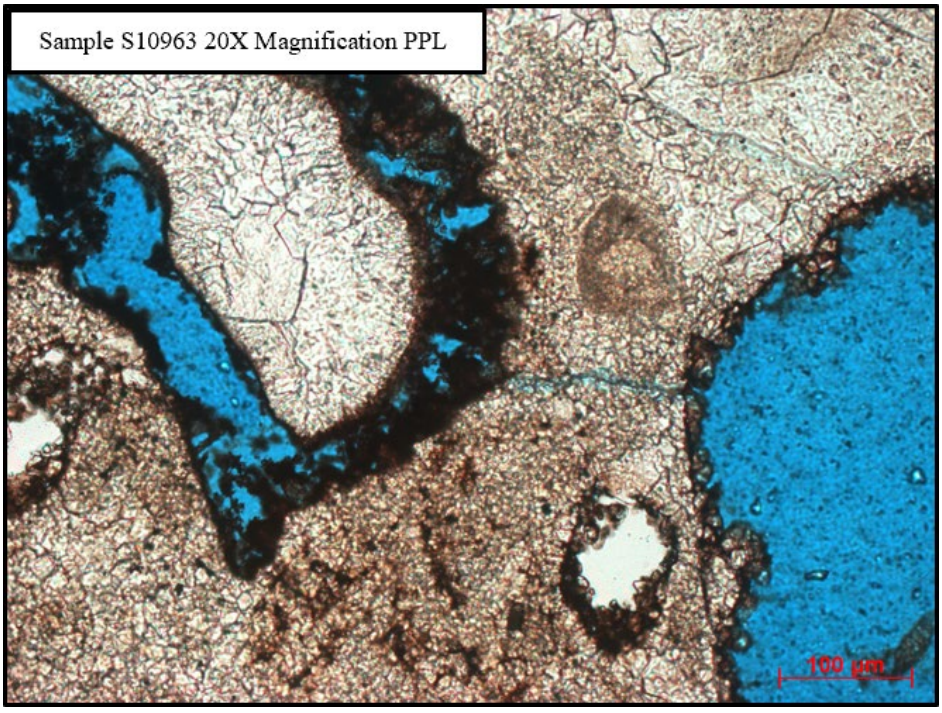

Figure 38: Open moldic porosity with hydrocarbon.

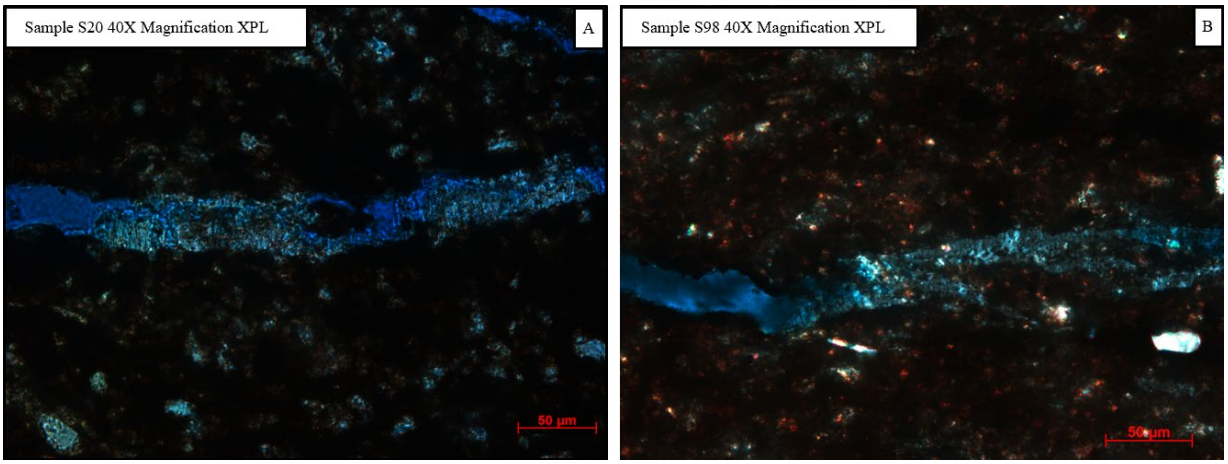

Figure 39 : Photomicrographs showing horizontal fractures (A) "Beef" calcite from upper interval paragenetic sequence (B) "Beef" anhydrite from lower paragenetic sequence.

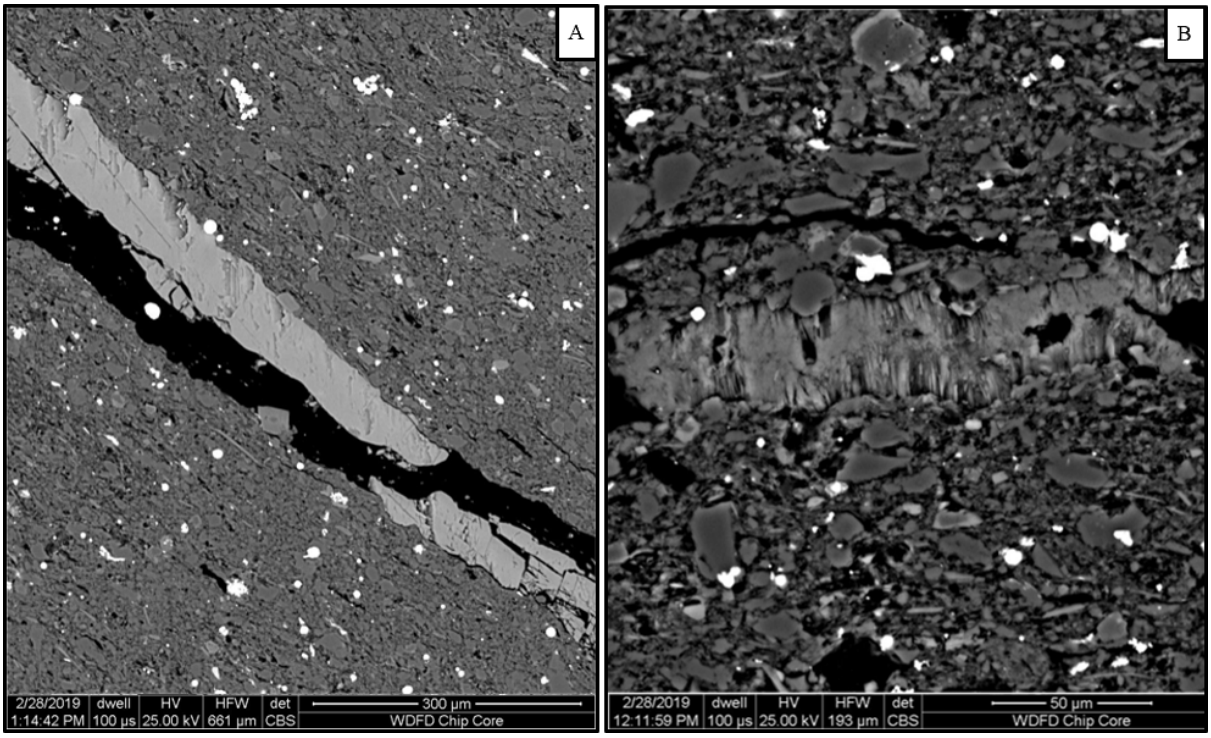

Figure 40: Backscatter photomicrographs showing horizontal fracture fill (A) "Beef" calcite with open porosity and hydrocarbon in the upper paragenetic sequence (B) "Beef" anhydrite with open porosity and hydrocarbon in the lower paragenetic sequence.

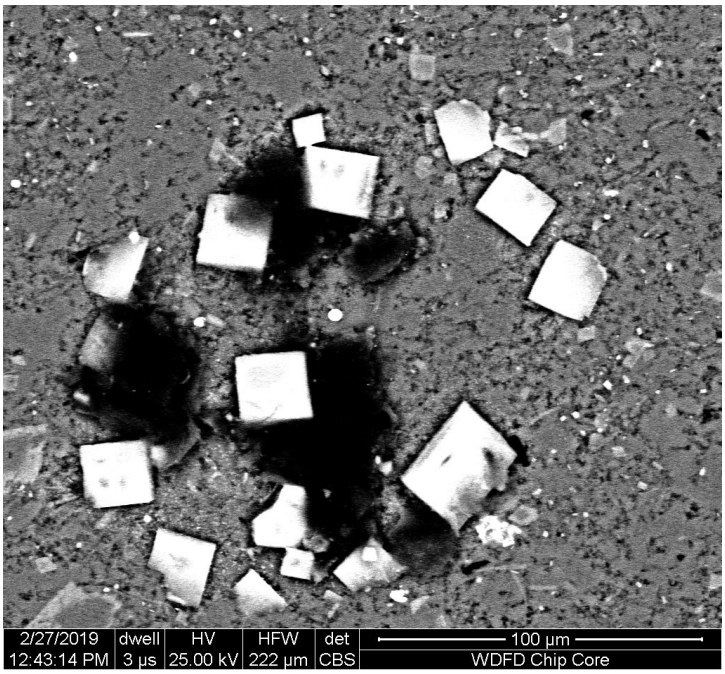

Figure 41: Backscatter photomicrograph showing euhedral halite with hydrocarbon in the lower paragenetic sequence.

Late Diagenesis

Late diagenesis shows evidence of external fluid movement in all three paragenetic sequences. Larger subvertical fractures opened in all sequences during late diagenesis. Within the shale rich sequences, fractures are filled with twinned calcite, a barite-celestine solid solution, and authigenic quartz (Figures 48A, 49, and 50A). Barite-celestine solid solution could not have been sourced from within the Upper Wolfcamp therefore external fluids are inferred. In the carbonates, the fractures are filled in the following sequence; calcite, dolomite, barite-celestine, and finally authigenic quartz (Figures 48B, 50B, and 51). Pyrite overprints of fractures are observed in all facies.

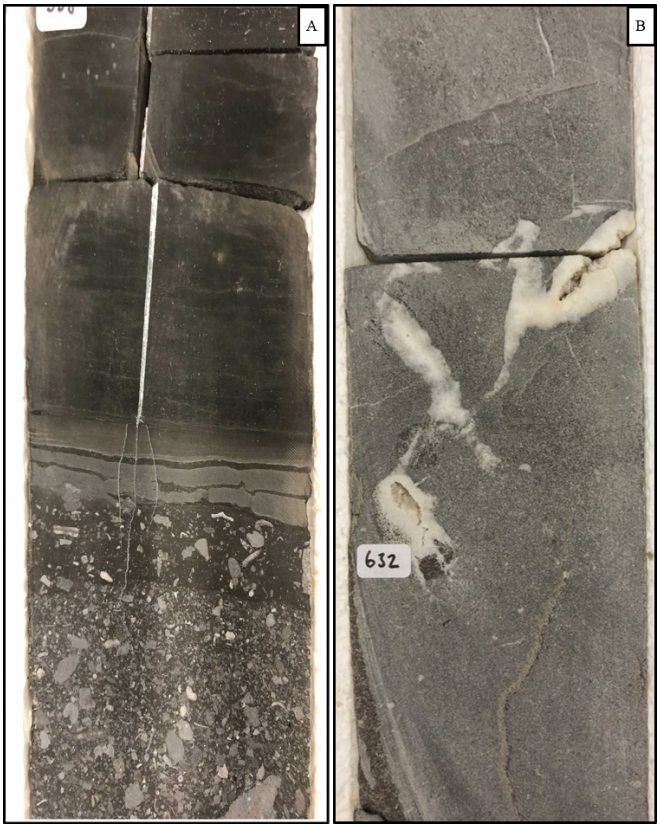

Figure 42: Core scale photos showing late fractures (A) Subvertical fracture bifurcating as it enters an open framework Bioclastic Argillaceous Siliceous Mudstone interval (B) Fracture with large open porosity in the Crinoid Brachiopod Bryozoan Wackestone and Packestone facies.

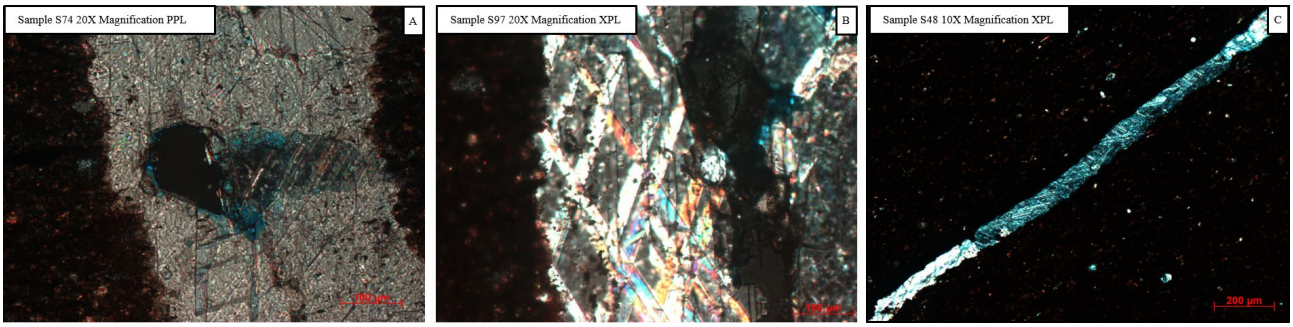

Figure 43: Photomicrographs showing late subvertical fractures (A) Twinned calcite with open porosity (B) Twinned calcite with barite-celestine solid solution (C) Twinned calcite fracture fill.

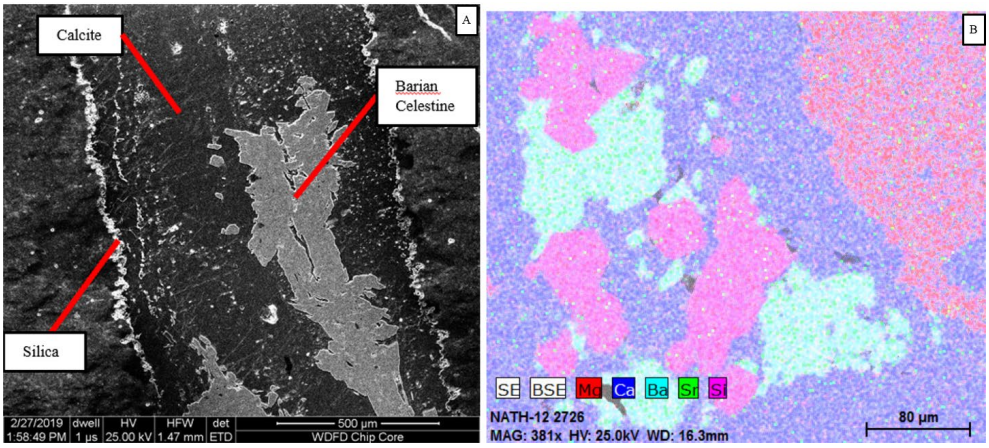

Figure 44: Backscatter photomicrographs of late fracture fill (A) Subvertical fracture in shale rich interval showing succession of silica, calcite, barite-celestine solid solution (B) EDAX elemental map of fracture fill in carbonate flow showing the succession of calcite, dolomite, barite-celestine solid solution, then euhedral quartz.

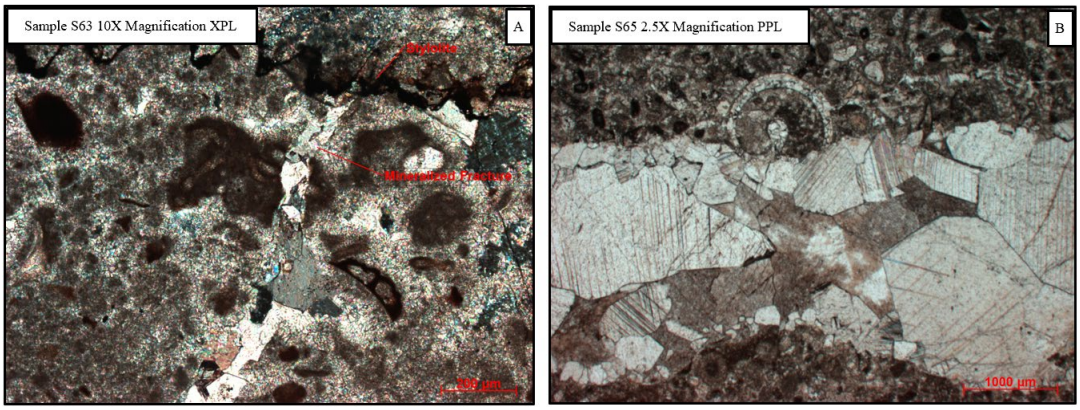

Figure 45: Photomicrographs of late fracture fill in carbonate flows (A) Stylolite crosscutting mineralized fracture (B) fracture from EDAX image in Figure 49 B showing calcite, then dolomite, then barite-celestine, then quartz.

Discussion

Chemostratigraphy

The key elements used in the chemostratigraphic study were Si, Al, Na, K, Ca, Mg, S, P, Fe, Ti, Zr, Mo, V, and Ni. Relative abundances are shown in Figure 30. Most rock property proxies put forth in previous studies are primarily based on siliciclastic rich systems where chemostratigraphic interpretations can be used to make system track interpretations. In the lower portion of this Southern Delaware Basin core, the source material is primarily carbonate therefore sequence inferences from chemostratigraphy are more difficult.

Silicon (Si) can be sourced in many ways such as detrital quartz, clay minerals, feldspars and biogenic quartz (Pearce and Jarvis, 1992; Pearce et al., 1999; Sageman and Lyons, 2004). Because silica abundance can be caused by multiple phases, it can be helpful to observe Si concentration relative to other elements like Ti or Al. Using ratios of Si/Ti and Si/Al, silica in clays and feldspars can be differentiated from silica associated with quartz phases (Pearce et al. 1999). Below about 10920ft there is an increase upward in Si without an associated increase in Al which may signal an increase in quartz. Increases in Ti , Zr, and the ratio of Si/Al like those seen above 10750 ft are inferred to be prograding siliclastic sedimentation (Turner, 2016)

Aluminum (Al) and Potassium (K) are usually derived from clay minerals and alkali feldspars (Pearce et al., 1999, Tribovillard et al., 2006). While alkali feldspar grains typically behave hydrodynamically similarly to sand and silt sized quartz grains, clay minerals have the potential to travel much farther due to a lower entrainment rate of flow. When the abundance of Al and K is compared to the abundance of other detrital elements, inferences about mineralogy can be made. In the interval above 10750 ft, an Al and K increase is associated with a relative

increase in detrital sourced Ti and Zr. This is interpreted to mean an increase in the abundance of feldspar minerals (Turner, 2016).

Titanium (Ti) and Zirconium (Zr) are derived from minerals of continental origin (Bhatia and Crook 1986: Sageman and Lyons, 2004). Above 10750ft, as these elements increase upward, it is inferred that continental sedimentation is increasing. Ti and Zr are also less likely to be included in sediments transported by wind (Sageman and Lyons, 2004).

Calcium (Ca) and Magnesium (Mg) are most strongly related to carbonate minerals such as calcite, aragonite, and dolomite (Banner, 1995; Tribovillard et al., 2006). Within the interval below 10750ft, Ca and Mg become enriched as carbonates push further out into the basin floor. Above 10750ft, Ca and Mg decrease.

Molybdenum (Mo) and Vanadium (V) concentrations are a useful proxy for determining the degree of anoxia within the bottom waters of a basin (Algeo and Lyons, 2006; Algeo and Rowe, 2012). Mo is generally in solution under oxidizing conditions and precipitates out of solution under anoxic conditions in combination with the right concentrations of sulfur (Tribovillard et al., 2006). Below 10750 ft the system likely had more oxygenated waters and there was a relative decrease in Mo and V. Above 10750 ft, Mo and V increased, signaling a shift to more anoxic bottom waters.

Nickel (Ni) can be linked to marine productivity (Tribovillard et al., 2006) and can indicate higher TOC values. Within the core, Ni did not show strong correlation with higher values of TOC, but Ni did increase as Mo and V did above 10750 ft. This suggests marine productivity was potentially higher above 10750 ft.

Depositional Model and Facies Interpretations

Depositional setting interpretations for lithofacies can be seen in table 5 and are based on processes from the model for subaqueous flows (Mulder et al., 2001) (Figure 11). The Argillaceous Siliceous Silty Shale Facies is interpreted to be deep basin sediment from hemipelagic fallout and distal turbidites. The interbedded laminated calclithite and argillaceous siliceous silty shale facies was common underneath flow intervals which supports the hypothesis that they could be submarine channel levee deposits. Some of the turbidity flows that were not near channels within the cored interval could have been submarine channel splays. The open-framework bioclastic argillaceous siliceous mudstone and the crinoid brachiopod bryozoan wackestone and packstone are interpreted to be a result of concentrated and hyperconcentrated density flows within a submarine channel. The massive and sometimes fining upward habit and grainsize of the two facies support density flow processes. Some of the flows could have also been splay deposits. The open-framework bioclastic argillaceous siliceous mudstone facies is likely a more distal flow than the crinoid brachiopod bryozoan wackestone and packestone facies. The flows incorporated more siliceous material as they moved basinward resulting in carbonate allochems in a siliceous matrix. The oligomictic limestone extraclast paraconglomerate facies is interpreted to be a result of debris flows within a submarine channel and these debris flows are likely more proximal than the open-framework bioclastic argillaceous siliceous mudstone and the crinoid brachiopod bryozoan wackestone and packstone. This debris flow interpretation is supported by the massive habit and large clast size of the oligomictic limestone extraclast paraconglomerate facies. The calcite cemented fine grained arkose facies is likely a result of either a small turbidity current in a submarine channel or it was incorporated into a larger density or debris flow.

Within the cored interval, the thickening, thinning, coarsening, and fining package were identified and interpreted (Figure 46. Smaller packages that show coarsening upward and thickening upward are interpreted as lobes building out from submarine. The fining upward and thinning upward sequences are interpreted to be channel deposits. The channel deposits are coarse and erosive at the base and typically contain both intraclasts and extraclasts eroded from upstream in the system. Intraclasts are comprised of pieces of other flows, fragments of planar laminated calclithite and shale, and shale clasts. Extraclasts are fragments derived from shelf environments up on the Central Basin Platform.

From the base of the core to approximately 1075 0ft, there is an overall thickening upward and coarsening upward sequence. This large package is interpreted to be a prograding submarine fan system within a larger shelf apron system (Figure 47). The gamma ray log also shows a corresponding trend to the observed deposition. There were likely multiple sources of carbonate material coming off the Central Basin Platform during Upper Wolfcamp time. The Central Basin Platform is the inferred source rather than Waha or Coyanosa. The shallower relief of the top of the Upper Wolfcamp to the East suggests sedimentation coming from the Central Basin Platform. Thinning of Wolfcamp sediments over the top of the Waha and Coyanosa structural features indicates that no framework carbonates were actively building. The proposed prograding fan model is based on a single well interpretation and could be tested through the use of regional 3-D seismic.

As the submarine fan system prograded basinward (base of the core to about 10750 ft), there was a gradual increase in oxygen rich water being delivered from the shelf, which decreased the preservation of the redox sensitive elements. The increase in supply of oxygenated waters is also supported by the increase in observed bioturbation. Above 10750 ft there appears

to be shift in deposition to a more shale rich system. The gamma ray and relative elemental abundance logs support this interpretation. Carbonate input drops significantly and there is an increase in siliciclastic associated elements. In addition to the shift in mineralogy above 10750 ft, there is also a shift in bottom water conditions. Bottom waters shift to a more anoxic environment which is illustrated by the increase upward in abundance of redox sensitive elements such as Mo, V, and Ni and a decrease in bioturbation.

One of the research objectives was to identify the key depositional system controls within the project area. This area of the Southern Delaware Basin experienced active tectonism and fluctuations in sea level during the time of Wolfcamp deposition. The apparent termination of the submarine fan sequence above 10750 ft indicates a larger shift in the depositional system rather than a submarine fan avulsion. This shift could mark the transition from Wolfcamp highstand carbonate production into a Bone Spring lowstand siliciclastic system, with the Hovey Channel cutting off circulation.

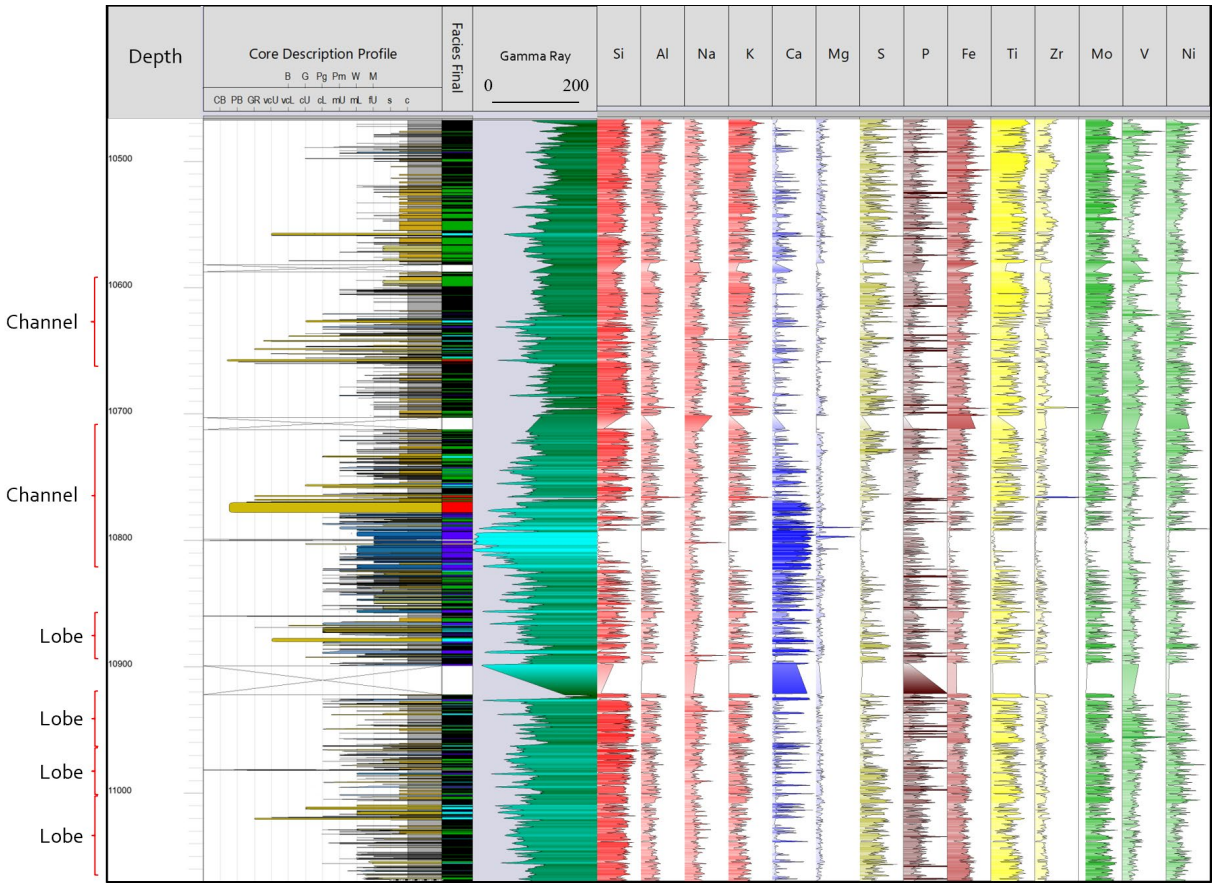

Figure 46: Core description with interpreted packages and logs for relative elemental abundances. Relative elemental abundances increase from left to right.

Table 5: Lithofacies with associated features and interpretations.

Facies	Rock Fabric	Sedimentary Structures	Bed Thickness	Fossils	Additional Features	Processes	Inferred Depositional Environment
Argillaceous Siliceous Silty Shale	Subangular-subround mud and silt sized quartz, albite, and clays	Facies dominantly black and faintly laminated. Sparse quartz and carbonate starved ripples. Sparse siderite and pyrite rich laminations. Calcite, siderite, and pyrite nodules present. Few Trace Fossils at both core and thin section scale.	<1in-12ft	Radiolaria, Calcispheres, peloids and Schwagerina Fusulinids were most abundant. Echinorderms, Crinoids, and brachiopods were also common but less abundant.	Horizontal and sub vertical mineralized fractures. Injectites	Hemipelagic Sedimentation and Distal Dilute Turbidity Currents	Deep Basin and Submarine Fan Interlobe
Interbedded Laminated Calclithite and Argillaceous Siliceous Silty Shale	Lamination of carbonate allochems and detrital quartz, albite and clay interbedded with argillaceous siliceous silty shale	Planar , ripple, and wavy laminations. Small fining upward sequences. Lenticular laminated muds. Thin section scale silt and carbonate laminations. Bioturbation more common than argillaceous siliceous silty shale	<1in-8ft	Radiolaria, calcispheres, peloids, Schwagerina fusulinids, echinoderms, crinoids, brachiopods, and sponge spicules were common. Some Fistuoloporit bryozoans and algae were also present but rare	Horizontal and sub vertical mineralized fractures. Injectites	Intermittent Hemipelagic Sedimentation and Turbidity Flows	Distal Lobe, Submarine Channel Levee, Submarine Fan Splay
Open-Framework Bioclastic Argillaceous Siliceous Mudstone	Carbonate allochems in and argilaceous siliceous silty shale matix	Massive, sometimes fining upward. Some planar laminations present	<1in-3ft	Radiolaria, calcispheres, peloids, Schwagerina fusulinids, echinoderms, crinoids, brachiopods, Fistuloporid bryozoans, sponge spicules, gastropods, and algae	Horizontal and sub vertical mineralized fractures. Injectites	Concentrated Density Flow or Hyperconcentrated Density Flow	Distal Submarine Channel Deposit, Distal Submarine Fan Lobe, Submarine Fan Splay
Crinoid Brachiopod Bryozoan Wackestone and Packstone	Carbonate allochems in a lime mud matrix	Massive with erosive contact at base	<1in-9ft	Schwagerina fusulinids, echinoderms, crinoids, brachiopods, bivalves, Dasycladacean algae, Fistuloporid bryozoans, sponge spicules, Tubiphytes algae, cephalopods, trilobites, and ooids were all present.	Mineralized fractures. Oil-stained porosity	Concentrated Density Flow or Hyperconcentrated Density Flow	Submarine Channel and Submarine Fan Lobe
Oligomictic Limestone Intraclast Paraconglomerate	Cobble to gravel sized fragments of platform material with smaller carbonate allochems in a mix of lime mud and argilaceous siliceous silty shale matrix	Massive with high angle erosive contact at base	6in-8.5ft	Schwagerina fusulinids, echinoderms, crinoids, brachiopods, bivalves, Dasycladacean algae, Fistuloporid bryozoans, sponge spicules, Tubiphytes algae, cephalopods, gastropods, peloids, and ooids were all present.	Large carbonate extraclasts present. Mineralized fractures	Debris Flow	Submarine Channel
Calcite Cemented Fine Arkose	Subangular fine sand sized quartz and albite grains with calcite cement	Planar laminations with evidence of soft sediment deformation	8.5in	None observed	Calcite cement	Turbidity Current or Debris Flow	Submarine Channel

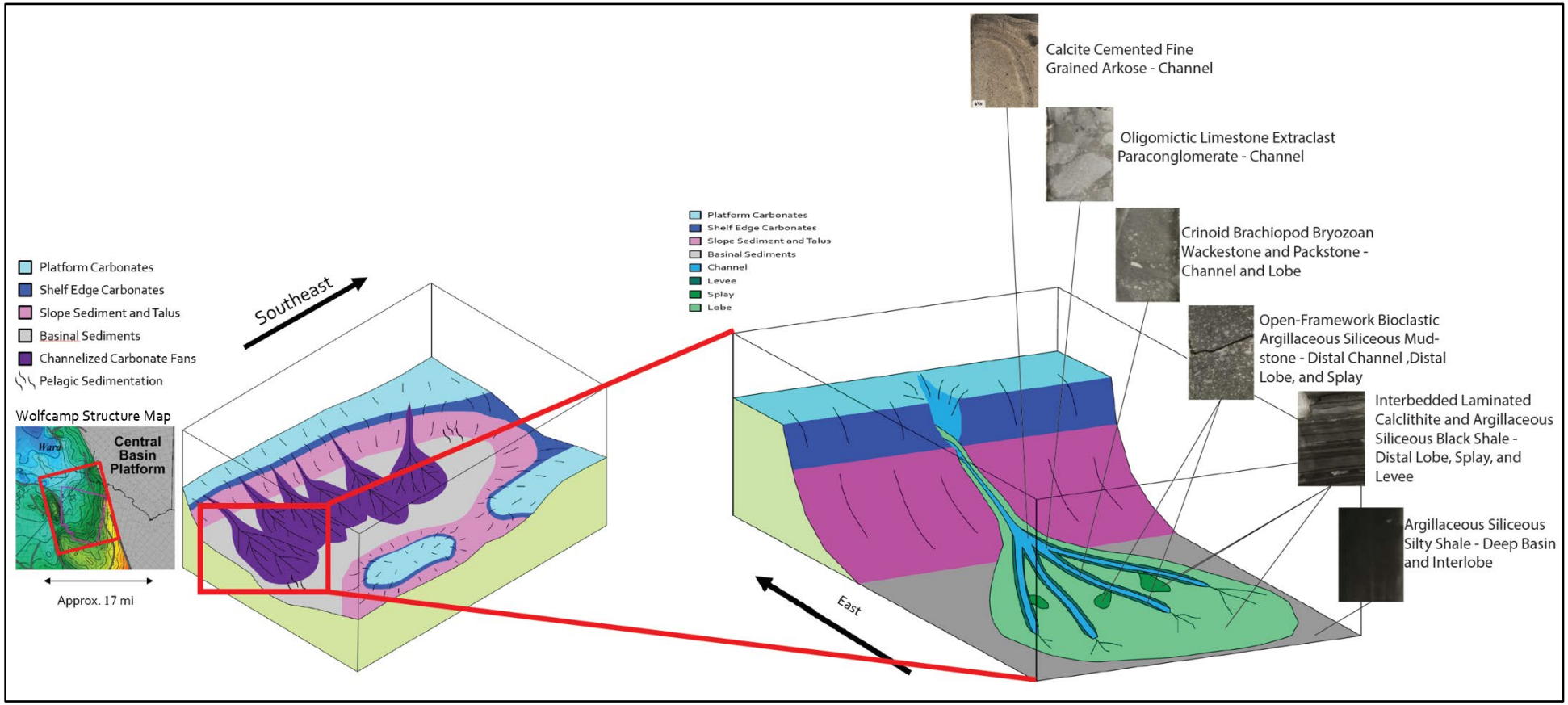

Figure 47: Model for observed deposition in the project area with interpreted facies depositional environments.

Lithofacies and Chemofacies Comparison

Figure 48 shows the comparison of chemofacies to lithofacies. Chemofacies 1 and 2 are typically associated with the argillaceous siliceous silty shale facies or the interbedded laminated calclithite and argillaceous siliceous silty shale facies because of the siliceous mineralogy and small amount of carbonate allochems. The enrichment in Mo, V, and Ni reflect the distal and anoxic interpretation for both the shale and interbedded shale and carbonate facies.

Chemofacies 3 and 4 are typically associated with the more carbonate rich lithofacies such as the open-framework bioclastic argillaceous siliceous mudstone, the crinoid brachiopod bryozoan wackestone and packstone, the oligomictic limestone extraclast paraconglomerate, and the calcite cemented fine grained arkose. These facies have the high relative abundances of Ca and Mg, associated with calcite and dolomite, and lower abundances of elements associated with siliciclastic minerals like quartz, clay minerals, etc.

Chemofacies 1 and 4 both show enrichment in elements associated with diagenetic alteration. In chemofacies 1 and 4, the relative increase in P, S, and Fe compared to chemofacies 2 and 3 probably correlates to early diagenetic minerals such as pyrite, apatite, and siderite. In chemofacies 1 the increase in Mg probably correlates to an increase in ferroan dolomite, the Mg in the carbonate rich facies could be detrital as well.

For this core the use of hierarchical cluster analysis (HCA) could point to differences in diagenetic alteration rather than significant changes in deposition. The diagenetically altered intervals do not seem to correlate to any depositional trends.

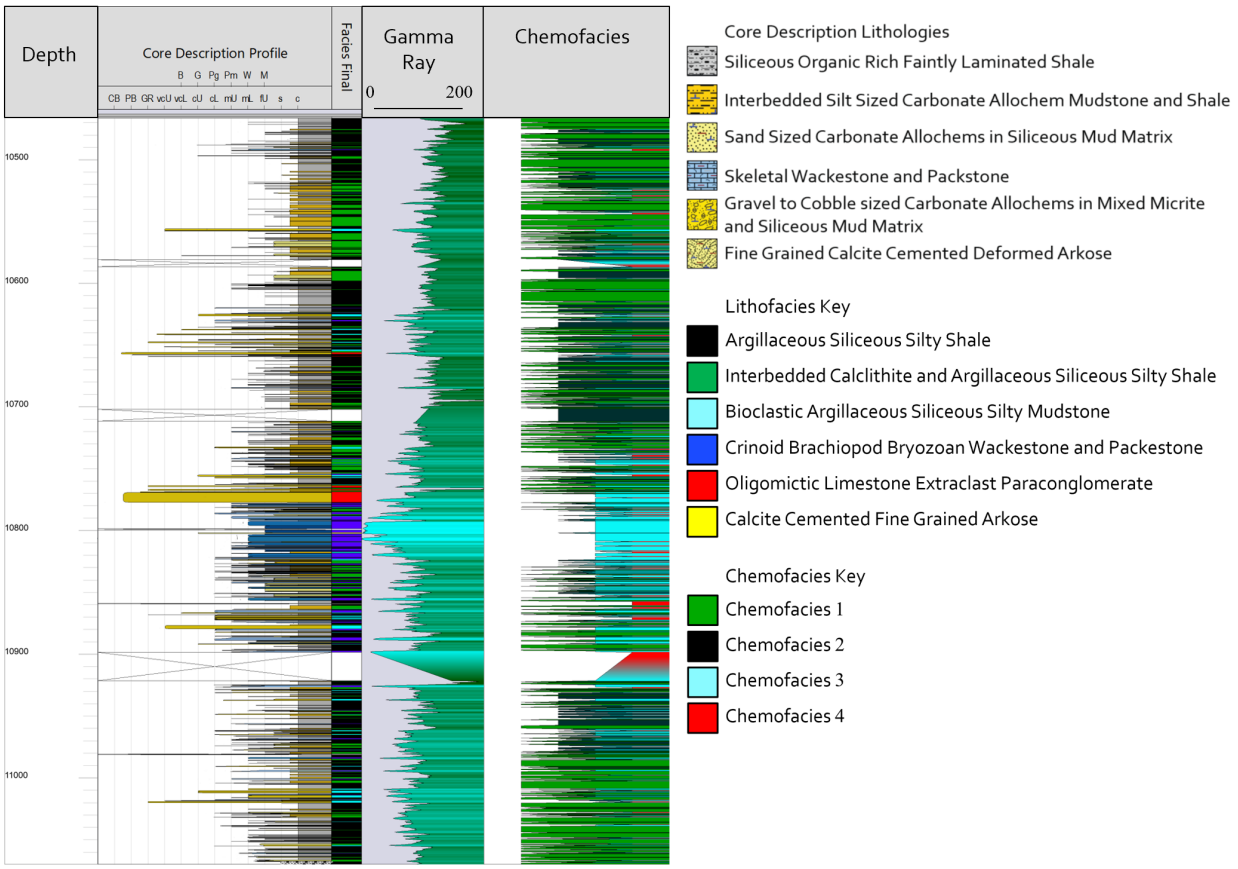

Figure 48: Comparison of Description Profile to Lithofacies, Gamma Ray log, and Chemofacies.

Reservoir Properties

For the entire project area, the interval above the apron system (Figure 49) looks ideal for unconventional development. In the interval above the fan, the distal flows would be laterally continuous and good targets. These flows would be good reservoirs for the organic rich intervals surrounding them, with good correlation between porosity and permeability. Less water saturation is associated with the decrease in carbonates. If the change from a carbonate rich prograding fan system to a more siliciclastic rich system is mappable on a regional scale, it would mark the shift to significantly better reservoir quality and source rock. The siliclastic interval appears to be good for fracturing due to the relatively high amount of quartz (Jin et al., 2015) compared to the more carbonate rich intervals. Mineralized fractures are observed

propagating more readily through the shale rich intervals and terminating or bifurcating into the carbonate flows throughout the core (Figure 38).

The interval below the fan (Figure 49) may be a good secondary target as it contains significant amount of the shale rich facies. There may be stratigraphic traps as shales pinch out in between impermeable carbonate rich lobes. Concerns would be higher water saturations, lower TOC, and lower mobile oil saturations. The interval could be similar to the type of production seen in the Lower Spraberry Shale near the Glasscock Nose in the Midland Basin (very high water production relative to oil). This secondary target is likely vertically isolated from the primary target above in terms of fracture propagation due to the thick carbonates in between.

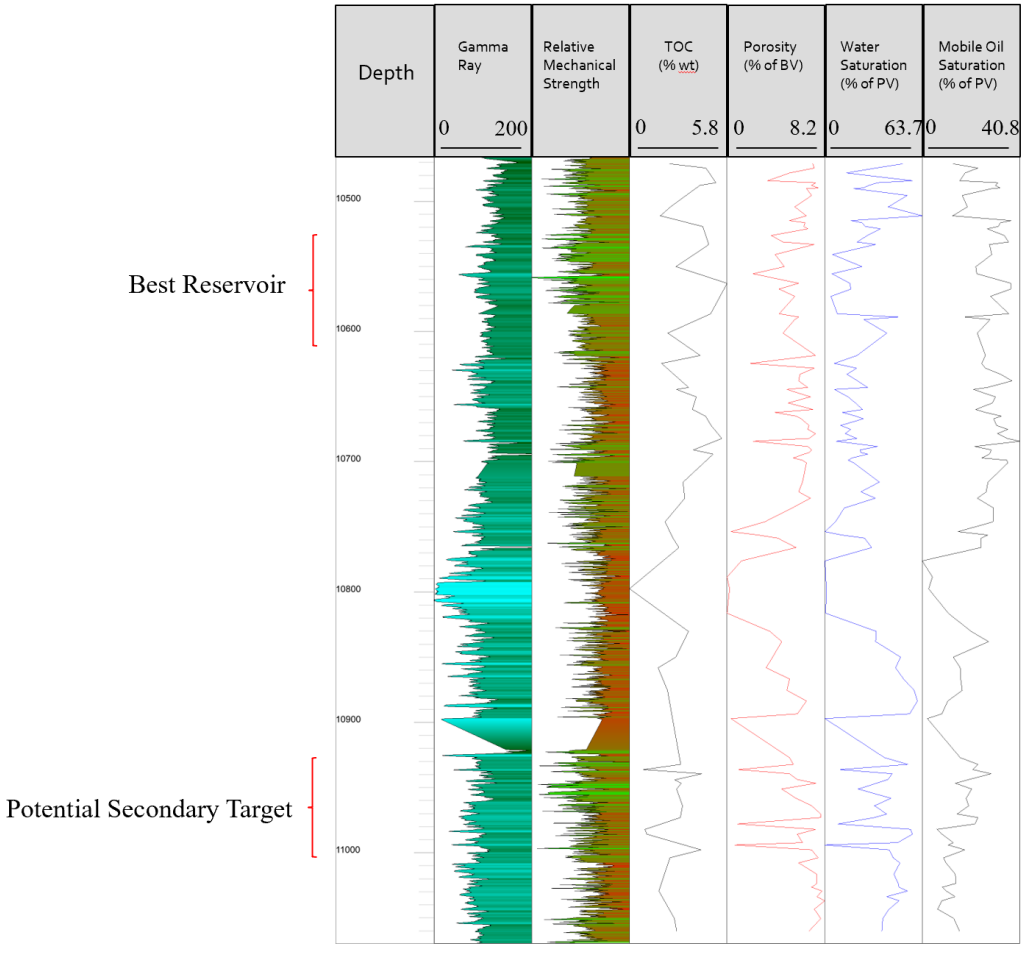

Figure 49: Logs for reservoir properties with inferred intervals best for development.

Diagenesis

The core from the Upper Wolfcamp show evidence for fluids and mineral phases that were sourced internally during early and middle diagenesis. The three paragentic sequences identified (Figures 30-32) also show late diagenetic phases that are likely externally sourced.

During early diagenesis the fluids were sourced from within the depositional system and the mineral constituents of the two shale rich intervals were very similar. During middle diagenesis the lower interval appears to have begun to open to outside fluids while the upper interval stayed closed through middle diagenesis. Then during late diagenesis, both intervals experienced fluid movement through large subvertical fractures.

The carbonate paragenetic sequence was different from the shales because of the shelf derived source material. The carbonate flows contained early diagenetic minerals and fluids from the platform that formed prior to transport and deposition. During later diagenesis moldic porosity, stylolites, and dolomite fracture fill were observed in the carbonates that were not observed in the shales.

The Upper Wolfcamp core contained many components that would be reactive during early diagenesis such as, organic matter, biogenic quartz, high magnesium calcite, and aragonite which could source early diagenetic mineral phases. These original minerals can source framboidal pyrite, amorphous chert, quartz, calcite, phosphatic and calcite concretions, and ferroan dolomite observed in the core through processes in the oxidation zone, the nitrate reduction zone, the sulfate reduction zone, the carbonate reduction zone and the fermentation zone (Hesse and Schacht, 2011).

During middle diagenesis within all three sequences, the organic matter continues to mature and enters a decarboxylation phase. During this phase organic acids are produced which caused the dissolution (moldic porosity and dissolved allochems) that was observed in the core. In the shale rich intervals, smectite to illite (McHargue and Price, 1982; Sivalingam, 1990) conversion is also associated with maturation of hydrocarbons. XRD shows dominantly illite clays within the core interval and hydrocarbons were observed between layers of clays. Smectite to illite conversion in addition to shale dewatering (Coniglio and James, 1988; Lumsden, 1988) began to overpressure the system. Horizontal calcite "beef" in the upper interval was likely sourced from within the system and formed during overpressuring (Cobbold, 2013). Hypersaline fluids that sourced evaporite minerals like anhydrite "beef" and halite in the lower paragenetic sequence were most likely sourced from above the Wolfcamp from either the Bone Spring, or the Ochoan evaporites. Hypersaline fluids were likely generated in a sabkha environment, were driven downward because of their density, penetrated the lower interval, and then were prevented from entering the upper part of the cored interval by the fan sequence. Temperature of formation for anhydrite is lower than calcite (Cobbold et. al., 2013) and this supports the idea that the fluids came from above the Wolfcamp rather than below. A block diagram showing a model for evaporite sourced fluids can be seen in Figure 47.

During late diagenesis there is evidence the diagenetic system further opened to outside sourcing. There is no evidence for a significant source of Ba within the rocks that could produce the barite in the barite-celestine subvertical fracture fills throughout the core. The fractures also contain open porosity that would allow fluid flow through the system. The project area is near deep, high angle faults (Figure 5) that could have acted as fluid conduits from the units below into the Upper Wolfcamp.

Diagenesis did not have a significant control on the relative reservoir quality observed within the core. Diagenetically altered intervals do not correlate to decreases in TOC, porosity, permeability, or mechanical strength. Most diagenetic phases were sourced from internal fluids and the large externally sourced subvertical fractures are present throughout the core. Reservoir quality is likely more controlled by minerals delivered during deposition than those precipitated during diagenesis.

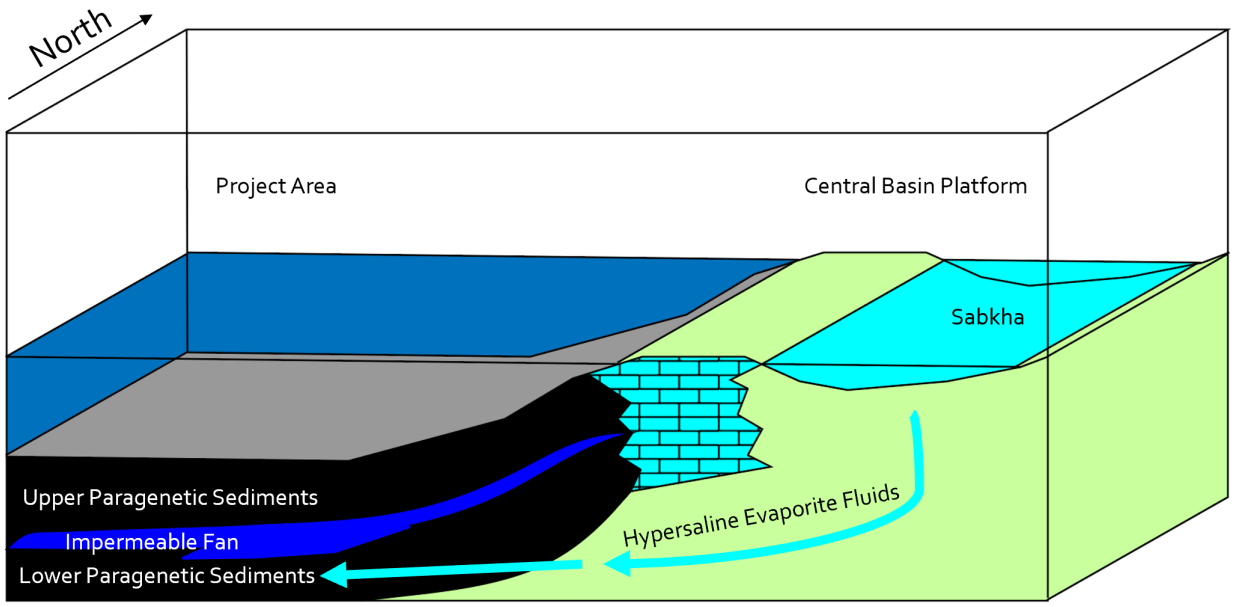

Figure 50: Block Model showing fluid source during middle diagenesis for evaporite minerals in the lower paragenetic sequence of the core.

Conclusions

For a core from the Upper Wolfcamp in the Southern Delaware Basin, six different lithofacies were identified and interpreted; Argillaceous Siliceous Silty Shale, Interbedded Laminated Calclithite and Argillaceous Siliceous Silty Shale, Open-Framework Bioclastic Argillaceous Siliceous Mudstone, Crinoid Brachiopod Bryozoan Wackestone and Packstone, Oligomictic Limestone Extraclast Paraconglomerate, and Calcite Cemented Fine Grained Arkose. Within the project area sub basin during Upper Wolfcamp time, a platform apron system comprised of channelized submarine fans was delivering sediments into deeper parts of the sub basin. The apron system was largely sourced from platform carbonates to the East. The upper interval above the fan shows a shift in the depositional system. Carbonate deposition drops significantly, and siliciclastic deposition from both hemipelagic fallout and turbidites increases. The chemostratigraphy shows bottom water conditions shift to a more anoxic environment. This shift in mineralogy and bottom water conditions may mark the transition from highstand carbonates into the lowstand siliciclastic setting of the Bone Spring group above the Upper Wolfcamp. The interval above the submarine fan system appears to be the best suited for unconventional drilling due to an increase in shale rich facies. There could potentially be a secondary target below the prograding fan sequence.

The diagenesis of the system is complex with at least three different paragenetic sequences observed within the core. The diagenetic system within the cored interval appears to be closed initially, but then opened later during diagenesis. Early and middle diagenetic alteration are inferred to be internally sourced from fluids and minerals within the Wolfcamp sediments. Middle and late diagenetic phases appear to be externally sourced in part. Evaporite minerals within lower interval horizontal fractures are inferred to be sourced from above the

Wolfcamp. Barite and celestine solid solution subvertical fracture fill is inferred to be sourced from deeper fluids below the Wolfcamp. Diagenesis however does not appear to have a significant control on relative reservoir quality within the core.

References

Adams, J. (1965). Stratigraphic-Tectonic Development of Delaware Basin. AAPG Bulletin, 49(11), p. 2140-2148.

Baker, C. L. (1928). The date of the major diastrophism and other problems of the marathon basin, trans-pecos texas. AAPG Bulletin, 12(11), p. 1111.

Broadhead, R. F., Jianhua, Z., & Raatz, W. D. (2004). Play Analysis of Major Oil Reservoirs in the New Mexico Part of the Permian Basin: Enhanced Production Through Advanced Technologies. New Mexico Bureau of Geology & Mineral Resources.

Cobbold, P. R., Zanella, A., Rodrigues, N., & Løseth, H. (2013). Bedding-parallel fibrous veins (beef and cone-in-cone): Worldwide occurrence and possible significance in terms of fluid overpressure, hydrocarbon generation and mineralization. Marine and Petroleum Geology, 43, p. 1–20.

Dunham, R.J. (1962). Classification of carbonate rocks according to depositional texture. In: Hamm, W.E. (Ed.), Classification of Carbonate Rocks. American Association Petroleum Geologists Memoir, p. 108-121.

Ewing, T.E. (2016). Texas Through Time: Lone Star Geology, Landscapes, and Resources, 431 p., BEG Publication, ISBN: 978-1-970007-09-1

Flamm, D. S. (2008). Wolfcampian Development of the Nose of the Eastern Shelf of the Midland Basin, Glasscock, Sterling, and Reagan Counties, Texas. [Master's Thesis]. Brigham Young University.

Galley, J. E. (1958). Oil and geology in the Permian basin of Texas and New Mexico: North

America.

Hardage, B., Pendleton, V., Major, R., Asquith, G., Schultz-Ela, D., and Lancaster, D. (1999). Using petrophysics and cross-section balancing to interpret complex structure in a limited-quality 3-D seismic image: GEOPHYSICS, v. 64, no. 6, p. 1760-1773, doi: 10.1190/1.1444682.

Hennenfent, G., Hegmann, M., Harris, C. and Schwartz, K. (2015). From core analysis to log-based pay identification in the Delaware Basin Wolfcamp Formation. Interpretation, 3(3), p. SV35-SV44.

Hesse, R., & Schacht, U. (2011). Early Diagenesis of Deep-Sea Sediments. Deep-Sea Sediments Developments in Sedimentology, 63, p. 557–713.

Hills, J. (1984). Sedimentation, Tectonism, and Hydrocarbon Generation in Delaware Basin, West Texas and Southeastern New Mexico. AAPG Bulletin, 68(3), p. 250-267.

Hobson, J. P., Caldwell, C. D., and Toomey, D. F. (1985). Early Permian Deep-Water Allochthonous Limestone Facies and Reservoir, West Texas. AAPG Bulletin, 69(12), p. 2130-2147.

Horak, R. L., 1985, Tectonic and hydrocarbon maturation history in the Permian basin: Oil & Gas Journal, May 27, v. 83, no. 21, p. 124–129.

Jin, X., S. N. Shah, J. C. Roegiers, and B. Zhang, 2015, An integrated petrophysics and geomechanics approach for fracability evaluation in shale reservoirs: Society of Petroleum Engineers Journal, v. 20, p. 518–526, DOI: 10.2118/168589-pa.

King, P. B., & King, R. E. (1929). Stratigraphy of outcropping Carboniferous and Permian rocks of trans-Pecos Texas. AAPG Bulletin, 13(8), p. 907-926.

Kutchin, Joseph W. (2001). How Mitchell Energy & Development Corp. Got Its Start and How It Grew: An Oral History and Narrative Overview. Universal Publishers. ISBN 978-1581126631.

Kvale, E. and Rahman, M. (2016). Depositional Facies and Organic Content of Upper Wolfcamp Formation (Permian) Delaware Basin and Implications for Sequence Stratigraphy and Hydrocarbon Source. URTeC.

Loucks, R., Brown, A., Achauer, C. and Budd, D. (1985). Carbonate Gravity-Flow Sedimentation on Low-Aangle Slopes Off The Wolfcampian Northwest Shelf of the Delaware Basin. The Society of Economic Paleontologists and Mineralogists (SEPM) Deep-Water Carbonates (CW6), p. 56-92.

Lowe, Donald R. (1982). Sediment Gravity Flows: II Depositional Models with Special Reference to the Deposits of High-Density Turbidity Currents. SEPM Journal of Sedimentary Research, Vol. 52(No. 1), p. 279-297.

Mazzullo, S.J. (1994). Diagenesis in a sequence-stratigraphic setting: porosity evolution in periplatform carbonate reservoirs, Permian Basin, Texas and New Mexico. Journal of Petroleum Science and Engineering - J PET SCI ENGINEERING. 11. p. 311-322. 10.1016/0920-4105(94)90049-3.

Mazzullo, S. J. (1995). Permian Stratigraphy and Facies, Permian Basin (Texas—New Mexico) and Adjoining Areas in the Midcontinent United States. In the Permian of Northern Pangea, p. 41-60, Springer Berlin Heidelberg.

Mazzullo, S.J., & Reid, A. M. (1988). Stratigraphic architecture of Pennsylvanian and Lower Permian Facies, Northern Midland Basin, Texas, in B. K. Cunningham, ed., Permian and

Pennsylvanian Stratigraphy, Midland Basin, West Texas: Studies to aid hydrocarbon exploration, Midland, Texas, West Texas Geological Society, Permian Basin Section. SEPM Publication, p. 88-28, 1-6.

Moede, I. (2018). Lithofacies and Chemostratigraphy of the Upper Wolfcampian in the Southeastern Delaware Basin, Pecos County, Texas. M.S. University of Texas at Austin.

Mulder, T. and Alexander, J. (2001). The physical character of subaqueous sedimentary density flows and their deposits. Sedimentology, 48(2), p. 269-299.

Nance, H. and Rowe, H. (2015). Eustatic controls on stratigraphy, chemostratigraphy, and water mass evolution preserved in a Lower Permian mudrock succession, Delaware Basin, west Texas, USA. Interpretation, 3(1), p. SH11-SH25.

Playton, T. and Kerans, C. (2002). Slope and Toe-of-Slope Deposits Shed from a Late Wolfcampian Tectonically Active Carbonate Ramp Margin. Gulf Coast Association of Geological Societies Transactions, 52, p. 811-820.

Rowe, H., Hughes, N. and Robinson, K. (2012). The quantification and application of handheld energy-dispersive x-ray fluorescence (ED-XRF) in mudrock chemostratigraphy and geochemistry. Chemical Geology, 324-325, p. 122-131.

Ross, C. (1986). Paleozoic evolution of southern margin of Permian basin. Geological Society of America Bulletin, 97(5), p. 536.

Shumaker, Robert C. (1992). Paleozoic Structure of the Central Basin Uplift and Adjacent Delaware Basin, West Texas (1). AAPG Bulletin, 76(No. 11), p. 1804-1824.

Tai, P., and Dorobek, S., 2000, Tectonic Model for Late Paleozoic Deformation of the Central Basin Platform, Permian Basin Region, West Texas, in The Permian Basin: Proving Ground for Tomorrow's Technologies, West Texas Geological Society, Midland, Texas, p. 158-176.

Turner, B. (2018). Utilization of Chemostratigraphic Proxies for Generating amd Refining Sequence Stratigraphic Frameworks in Mudrocks and Shales. Ph. D. University of Oklahoma.

Udden, J. A., & Bowman, W. F. (1917). Notes on the Geology of the Glass Mountains (Vol. 1, No. 1753). The University of Texas Bulletin, p. 41

Wahlman, G. and Tasker, D. (2013). Lower Permian (Wolfcampian) Carbonate Shelf-Margin and Slope Facies, Central Basin Platform and Hueco Mountains, Permian Basin, West Texas, USA. SEPM Special Publication, 105, p. 305-333.

Wedepohl, K. (1971). Environmental influences on the chemical composition of shales and clays. Physics and Chemistry of the Earth, 8, p. 307-333.

Wentworth, C. K. (1922). A scale of grade and class terms for clastic sediments. The journal of geology, 30(5), p. 377-392.

Wickard, Alyssa and Elmore, Richard and Heij, Gerhard. (2016). A Diagenetic Study of the Wolfcamp Shale, Midland Basin, West Texas. 10.15530/urtec-2016-2460784.

Xue, J., Lee, C., Wakeham, S. and Armstrong, R. (2011). Using principal components analysis (PCA) with cluster analysis to study the organic geochemistry of sinking particles in the ocean. Organic Geochemistry, 42(4), p. 356-367.

Yang, K., and Dorobek, S., 1995, The Permian Basin of West Texas and New Mexico Flexural Modeling and Evidence for Lithospheric Heterogeneity Across The Marathon Foreland: Stratigraphic Evolution of Foreland Basins, SEPM Special Publication, v. 52, p. 37-50.

Zhang, H., Janson, X., Liu, L. and Wang, Z. (2017). Lithofacies, Diagenesis, and Reservoir Quality Evaluation of Wolfcamp Unconventional Succession in the Midland Basin, West Texas. Search and Discovery, Article #80607.

Zoeten, E. and Goldstein, R. (2017). Diagenetic History of the Wolfcamp A in the Eastern Midland Basin, Texas. Search and Discovery, Article #51395.

Appendix

PARSLEY

EasyCore
The EasyCopy Company

Operator: Parsley Energy	
Top: 10466 ft	Bottom: 11069.7 ft
Country: United States	Well Name & No.
Location	Logged by
Date: Wed Jul 30 2014	Basin
Lease	UWI No.
OCS No.	Field
KB: 0 ft	WD: 0 ft
Latitude	Longitude

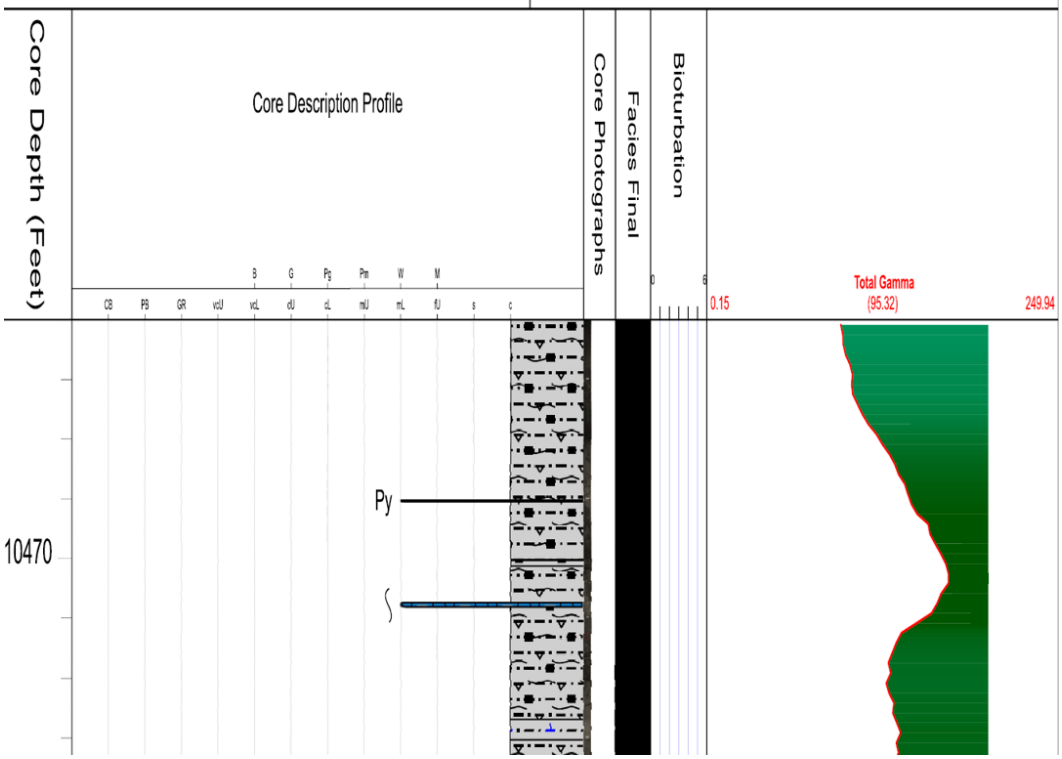

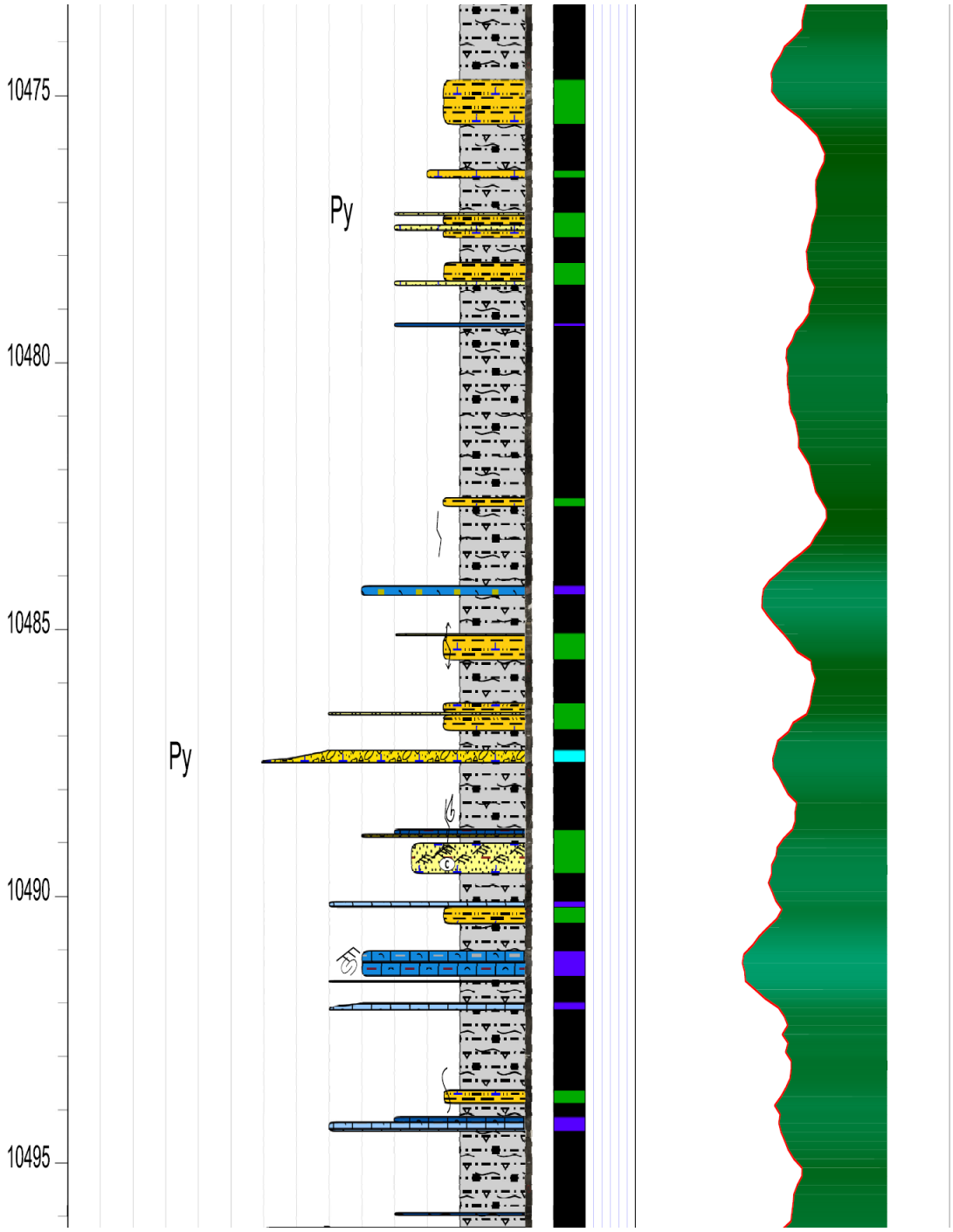
10475
10480
10485
10490
10495
Py
Py

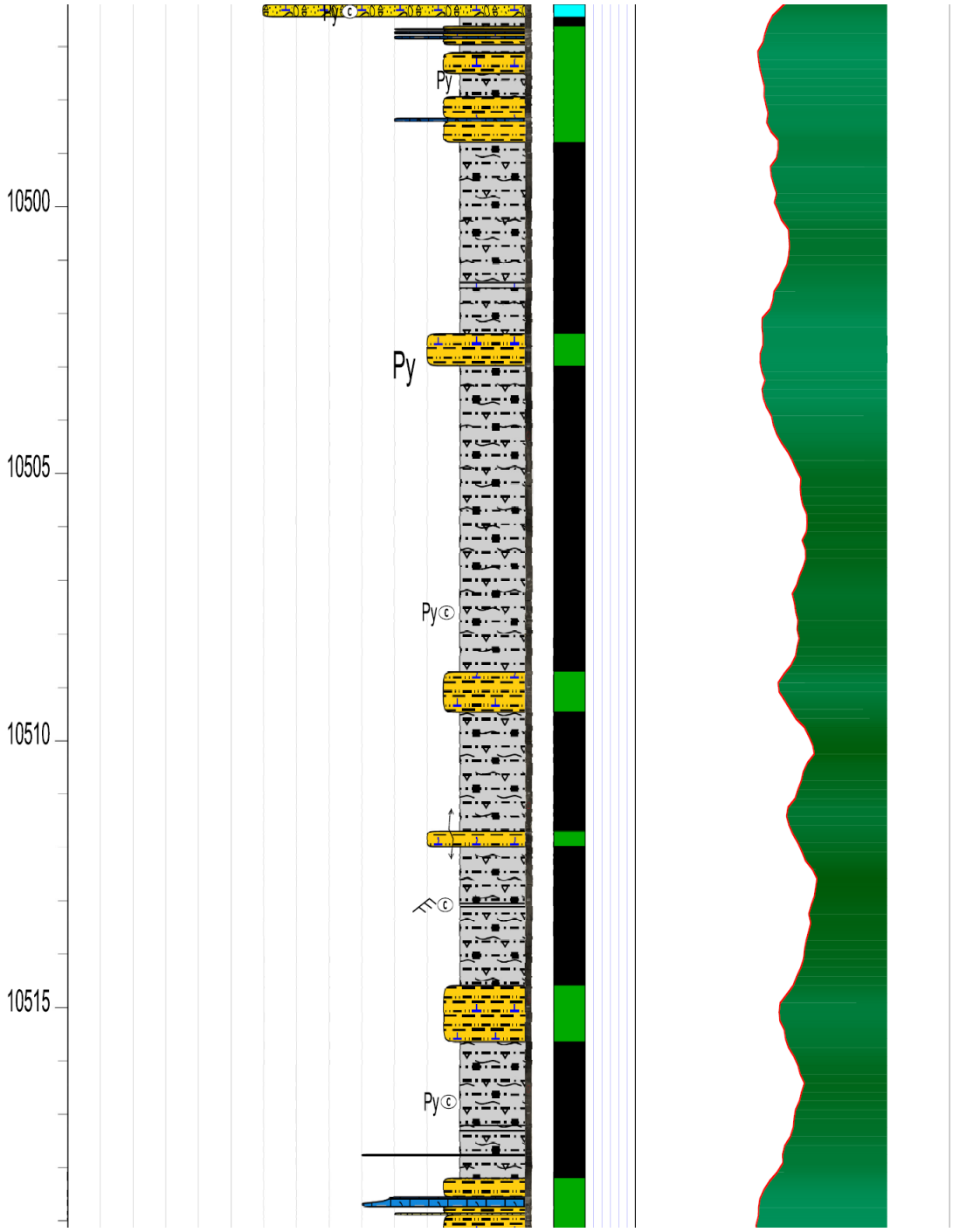
10500
10505
10510
10515
Py
Py
Py
Py
Py

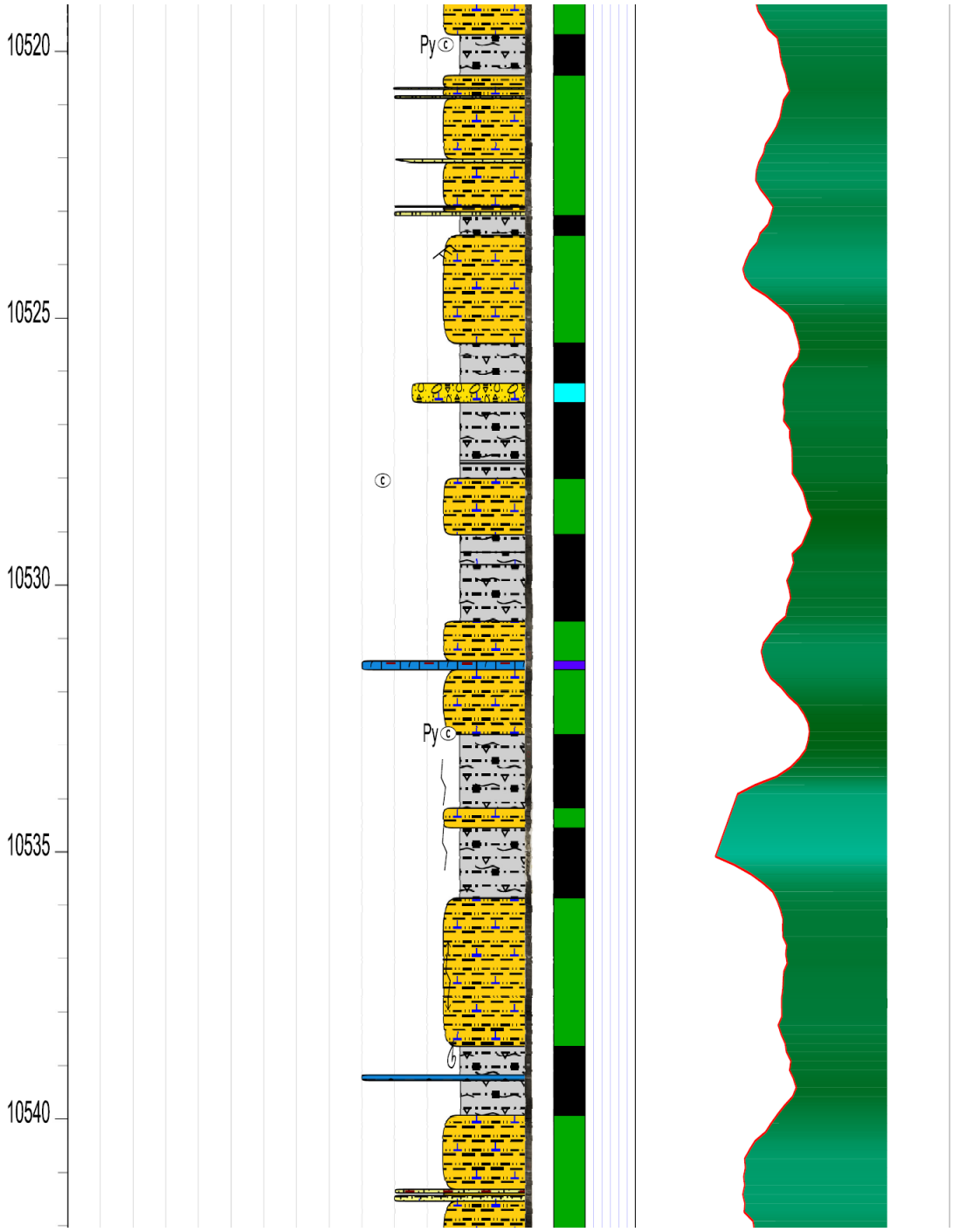
10520
10525
10530
10535
10540
Py
C
C
Py
C

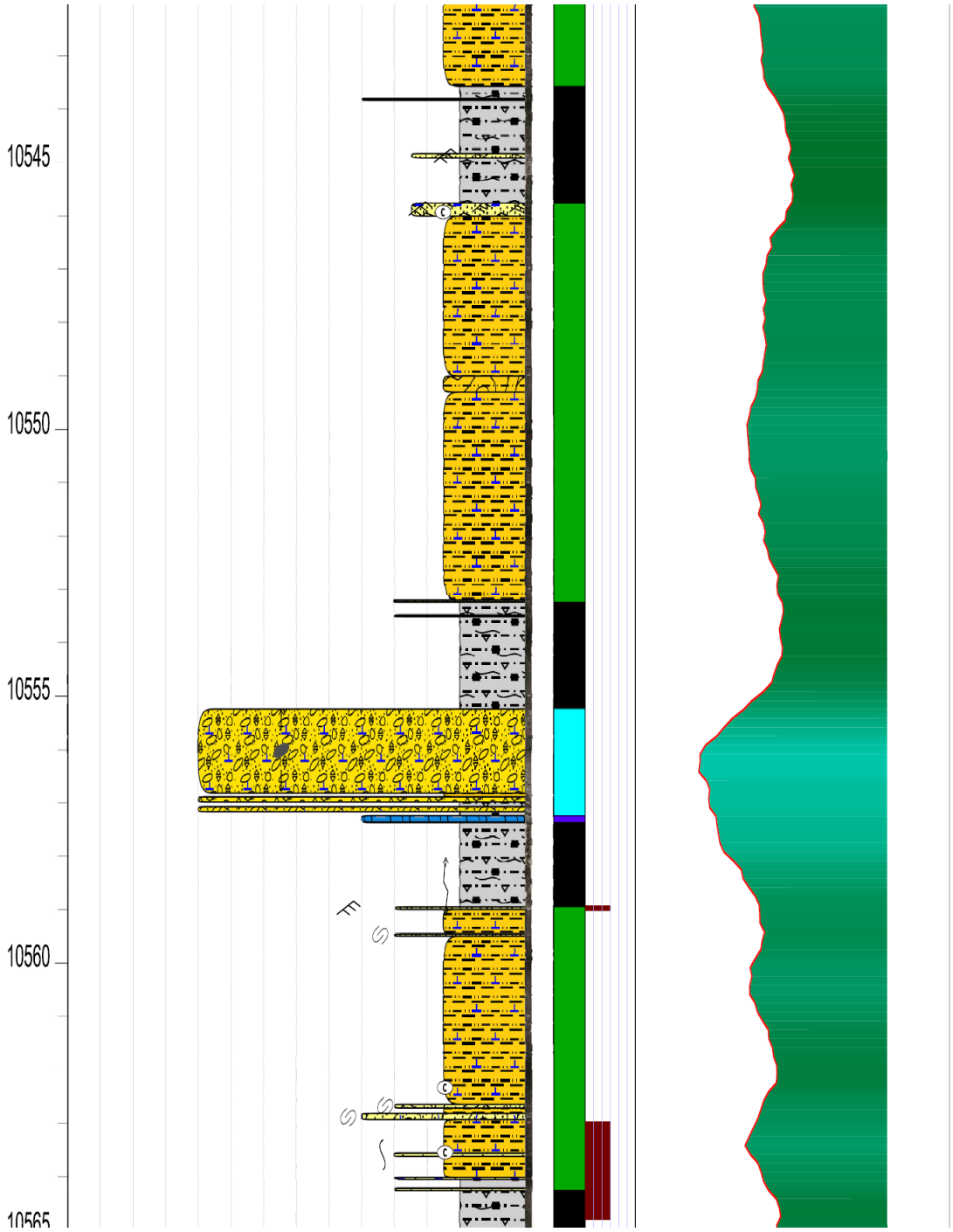
10545
10550
10555
10560
10565

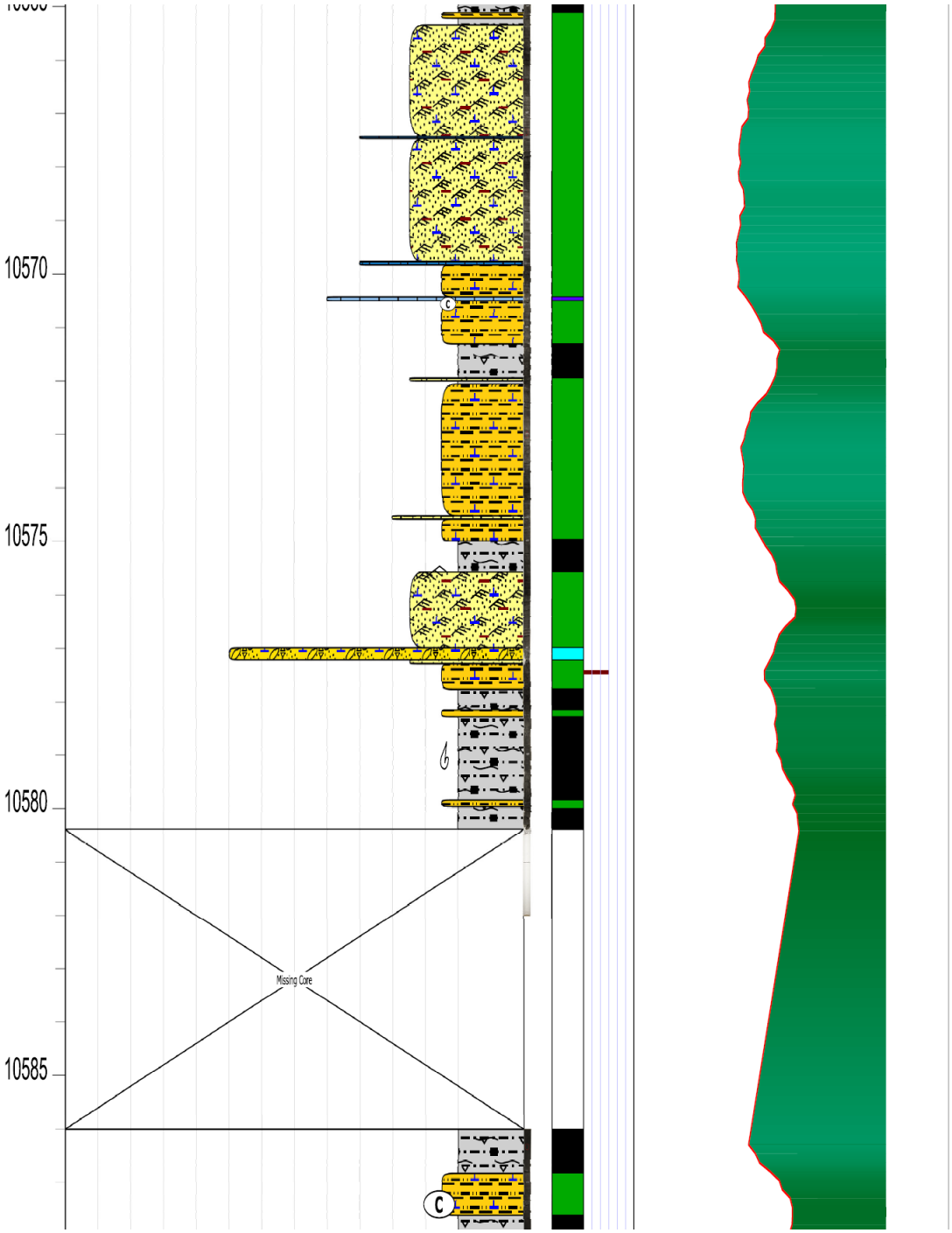
10570
10575
10580
10585
Missing Core
C
C

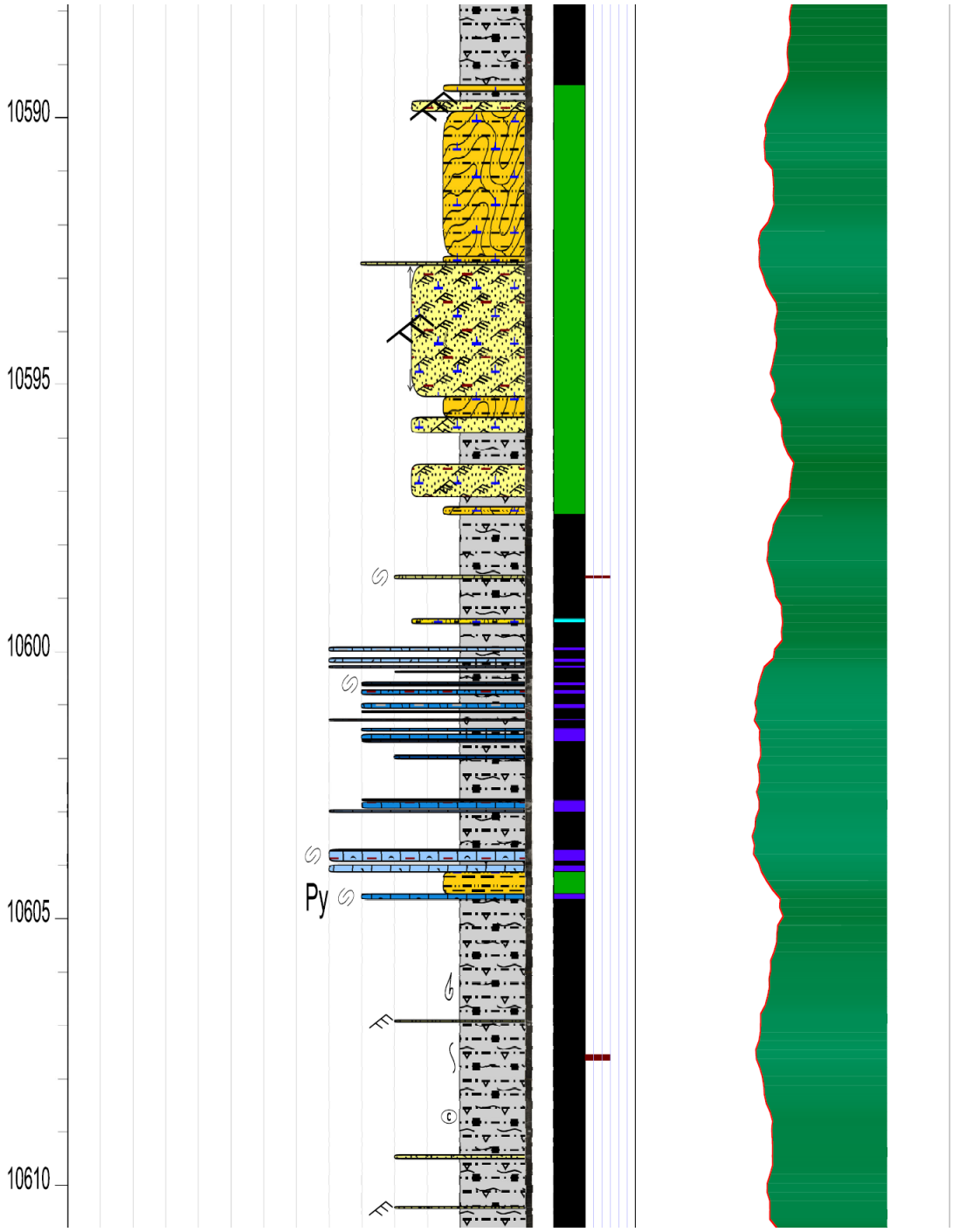
10590
10595
10600
10605
10610
Py

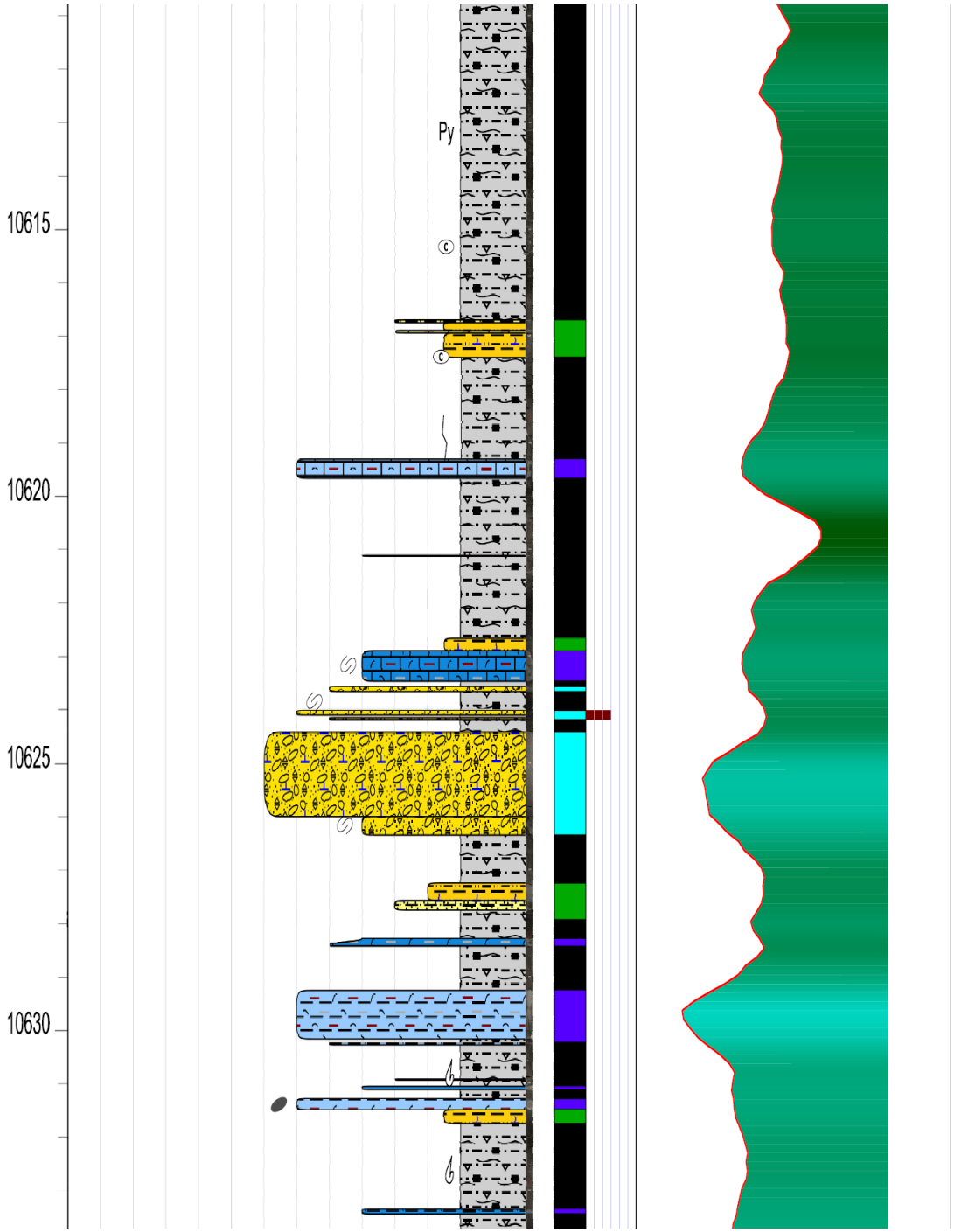
Py
10615
10620
10625
10630

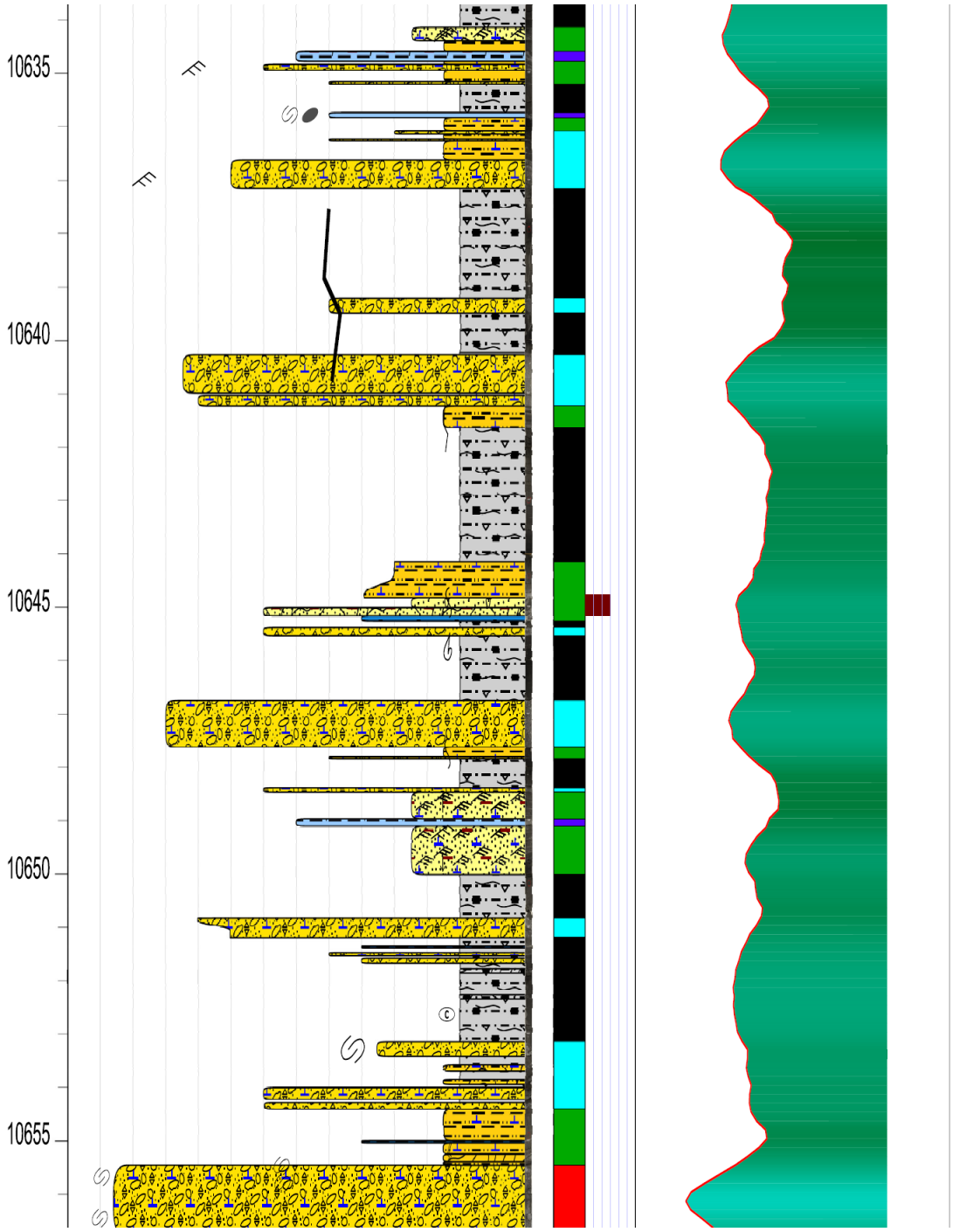
10635
10640
10645
10650
10655

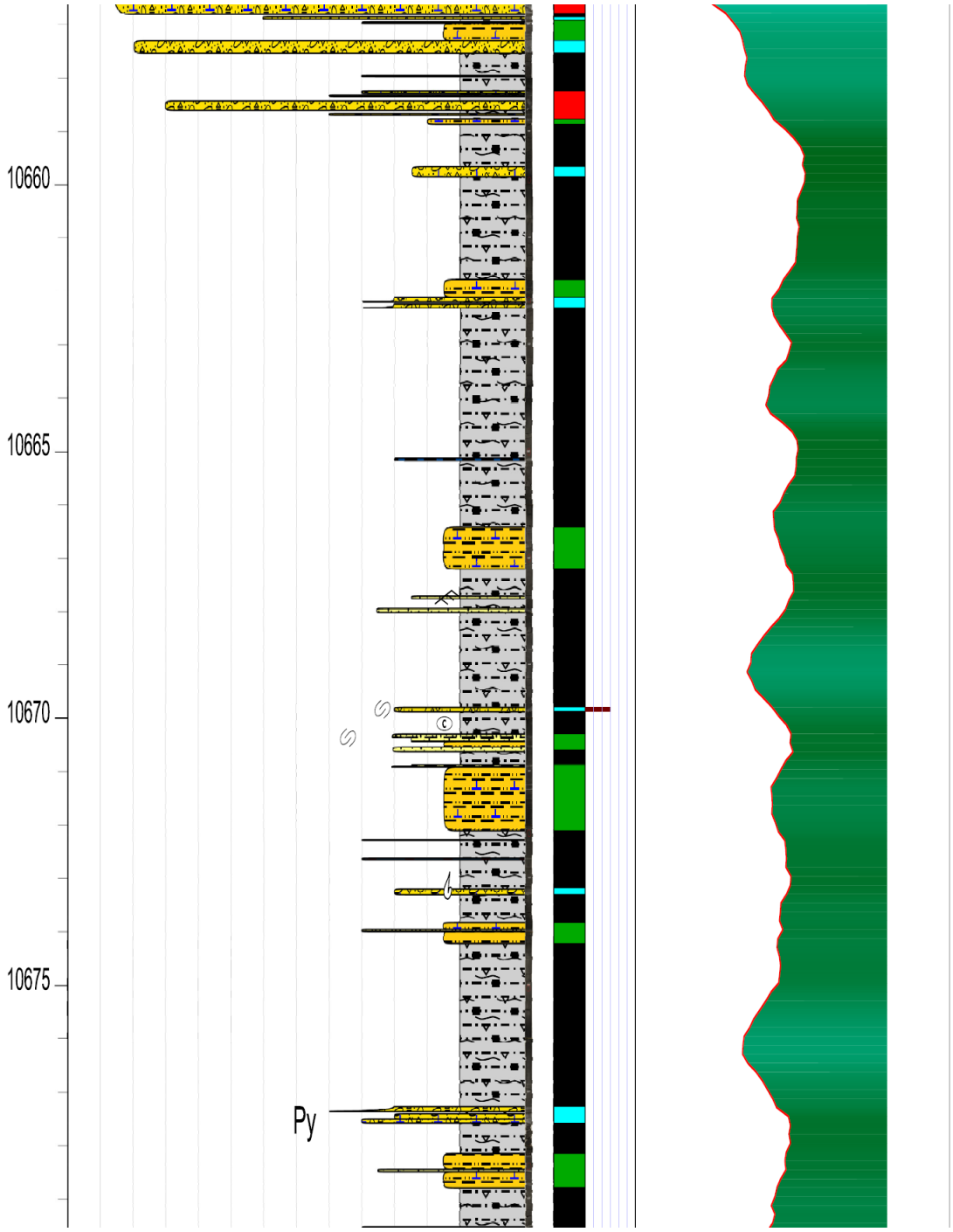
10660
10665
10670
10675
Py

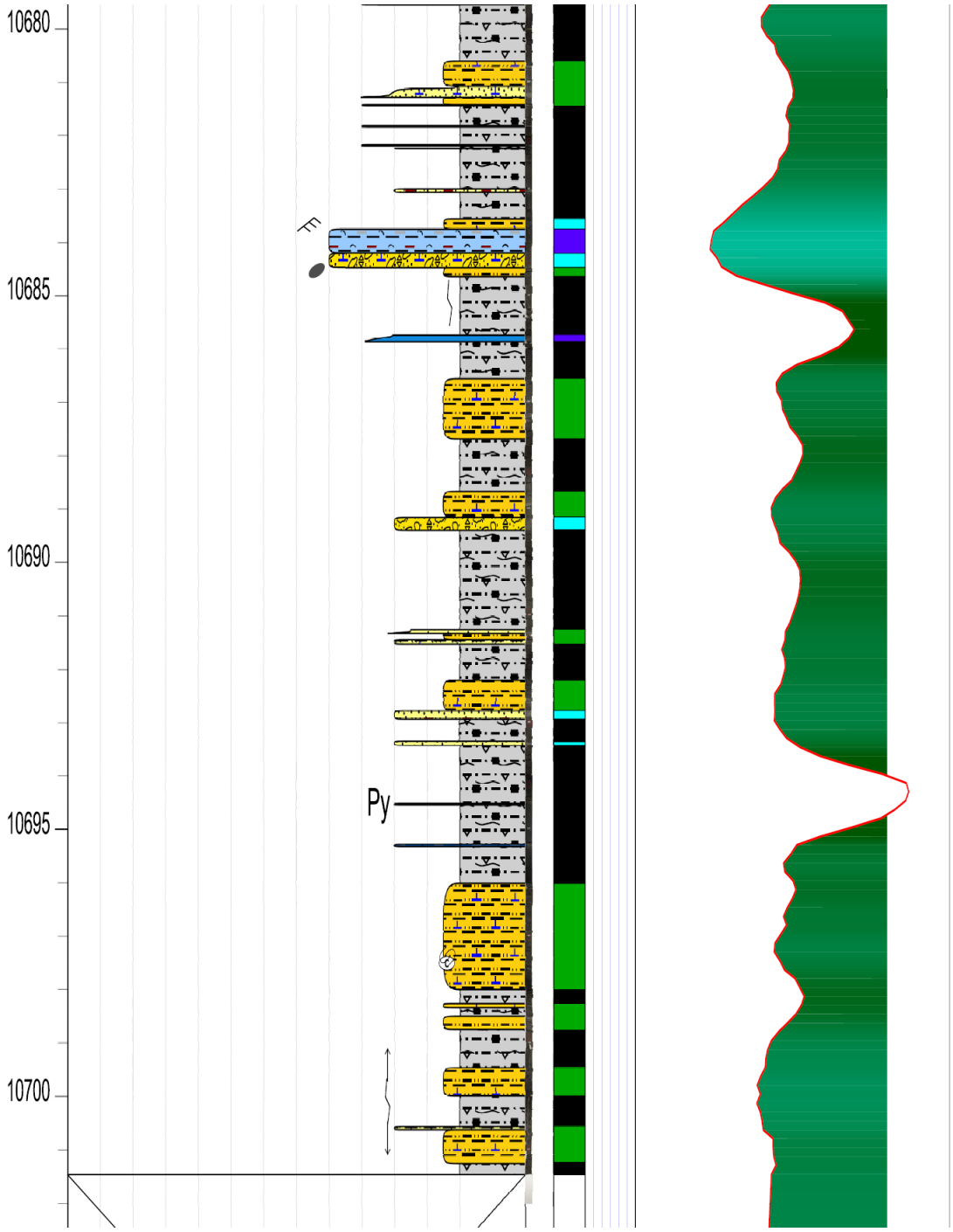
10680
10685
10690
10695
10700
Py

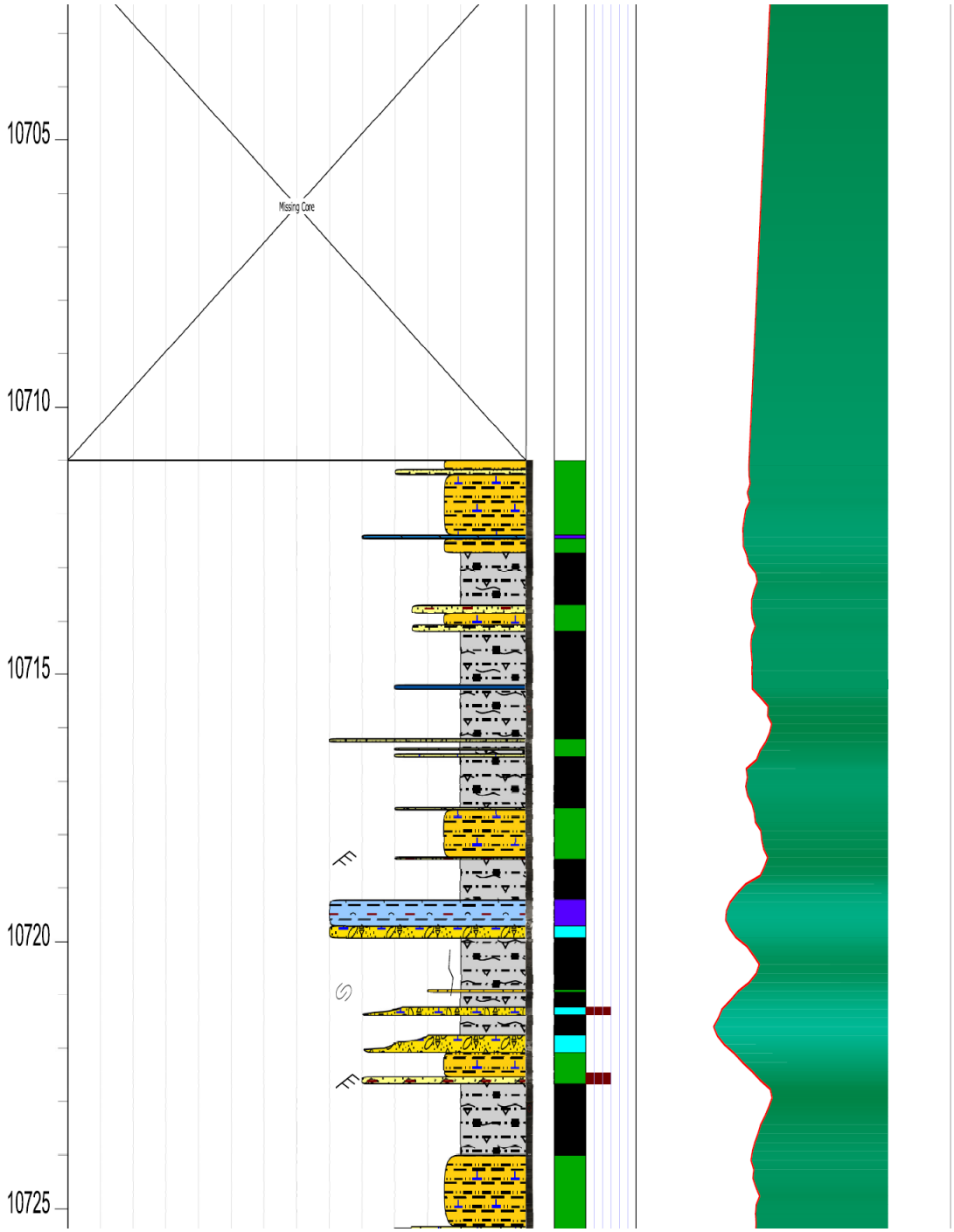
10705
10710
10715
10720
10725
Missing Core
F
S
F

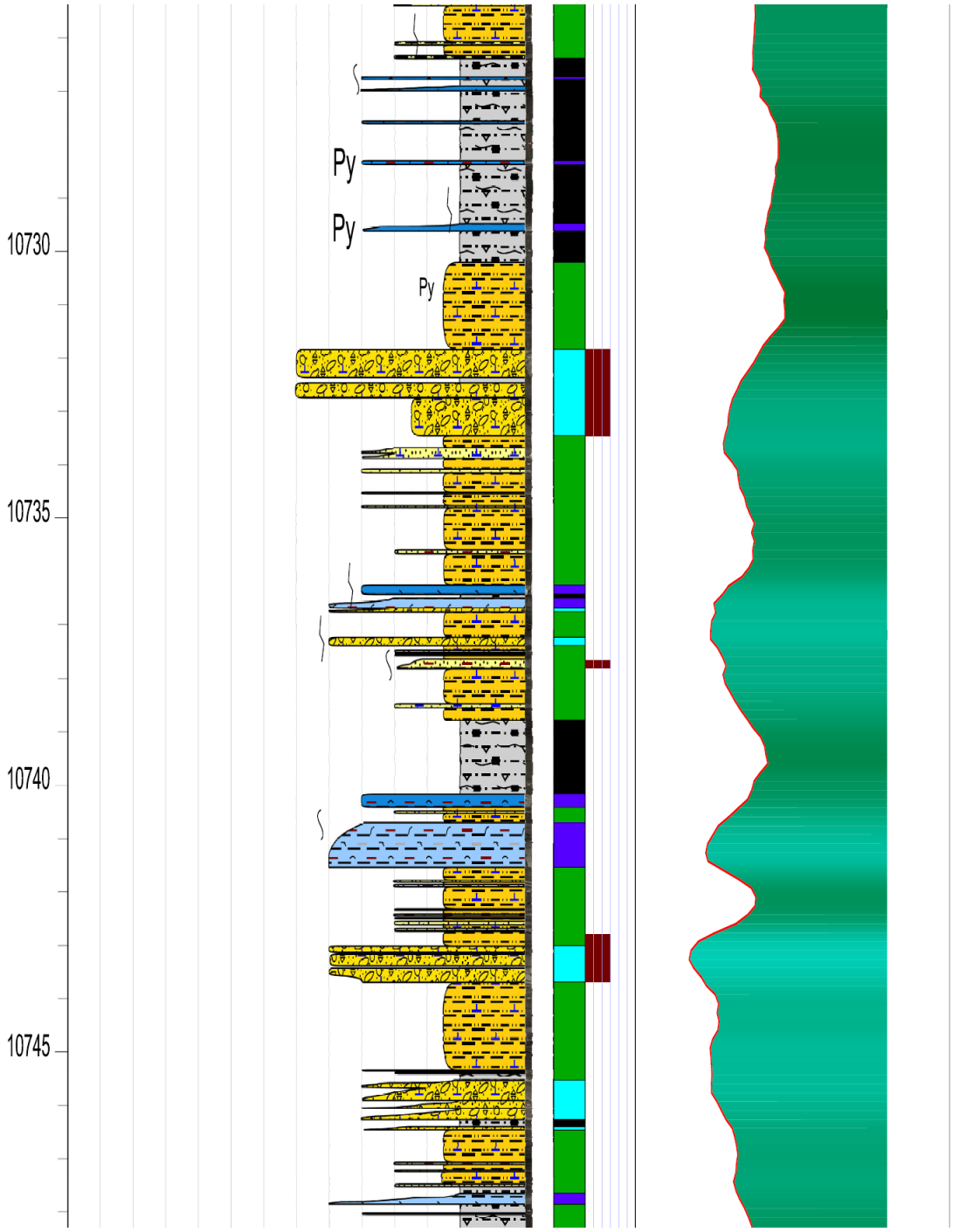
10730
10735
10740
10745
Py
Py
Py

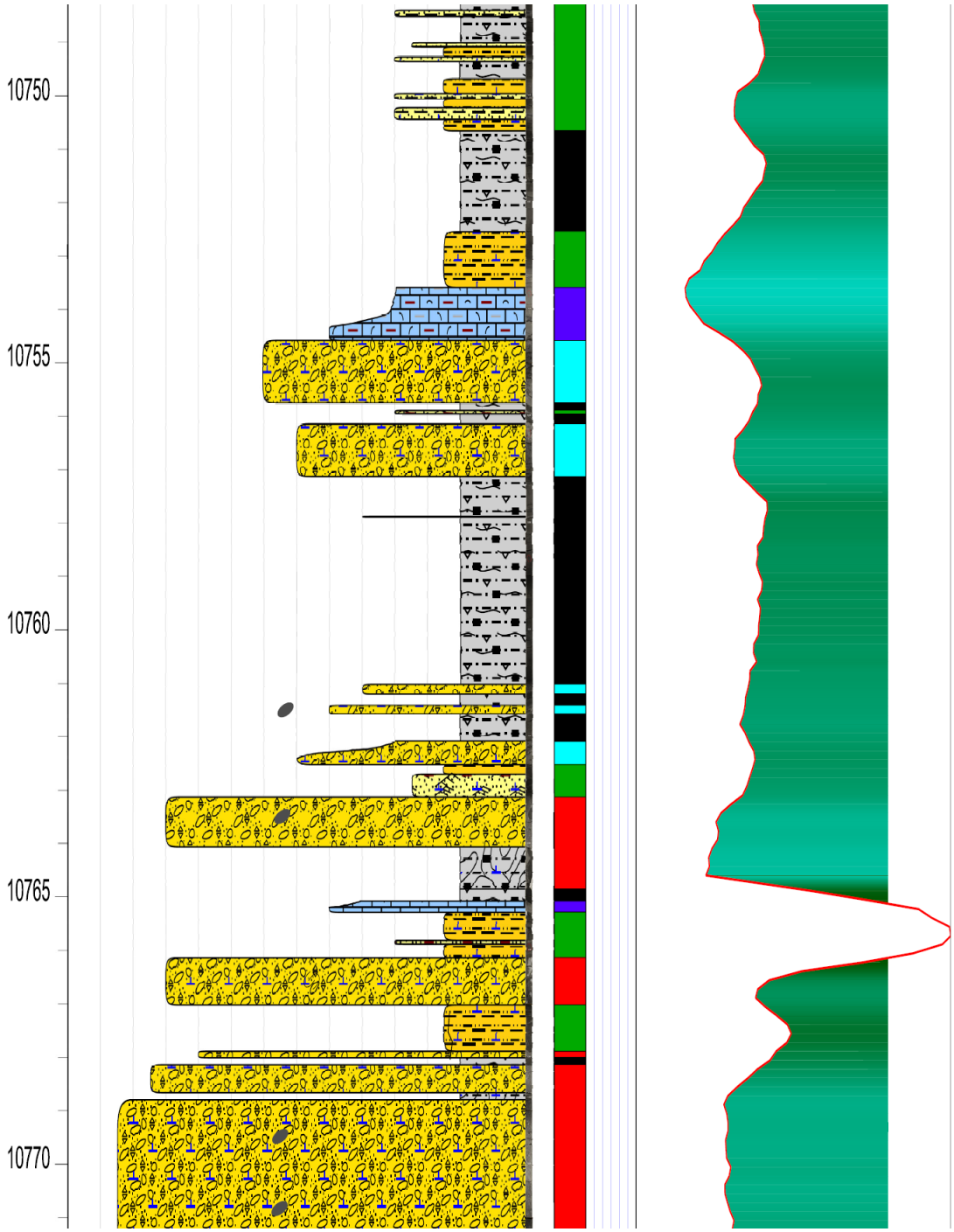
10750
10755
10760
10765
10770

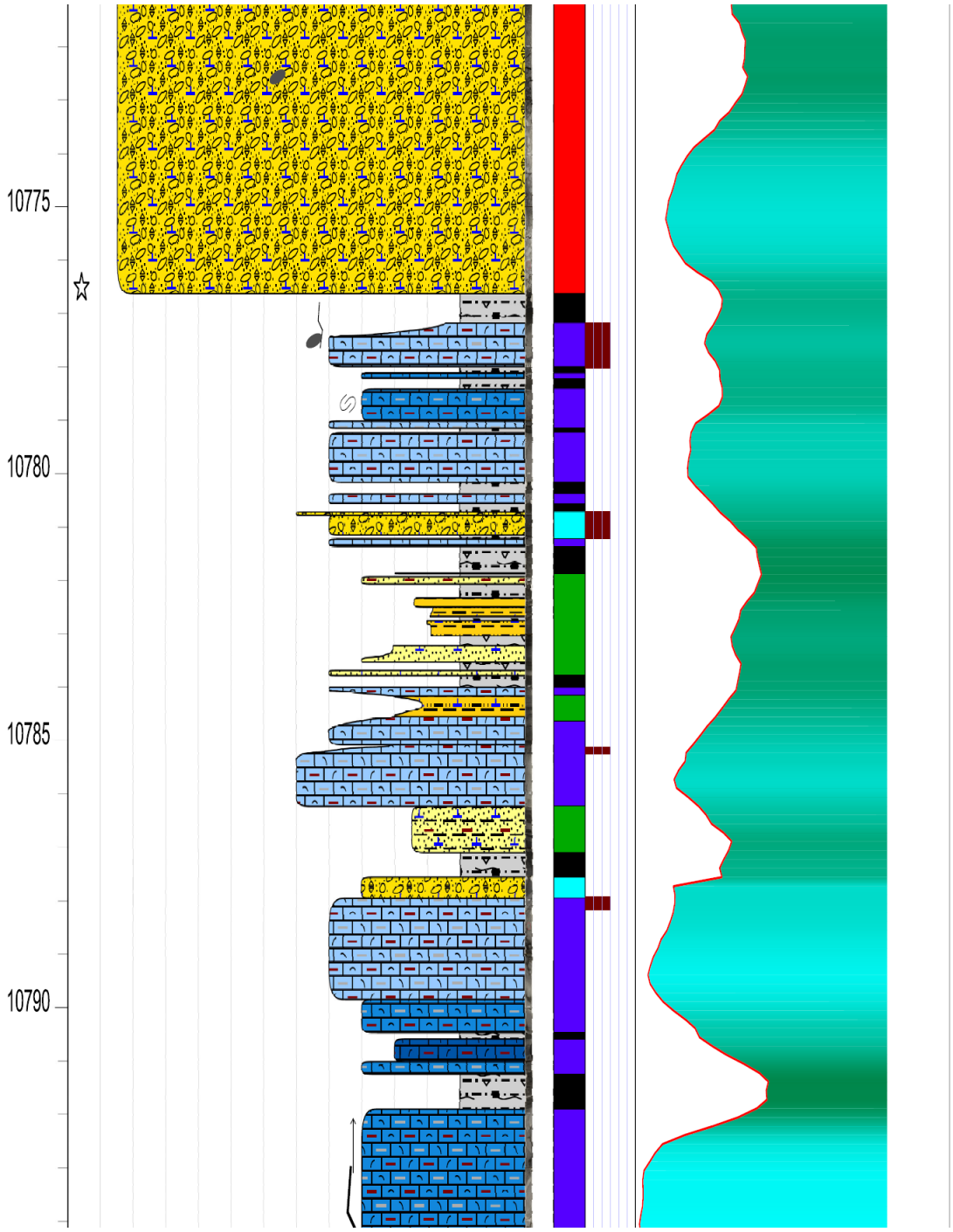
10775
10780
10785
10790

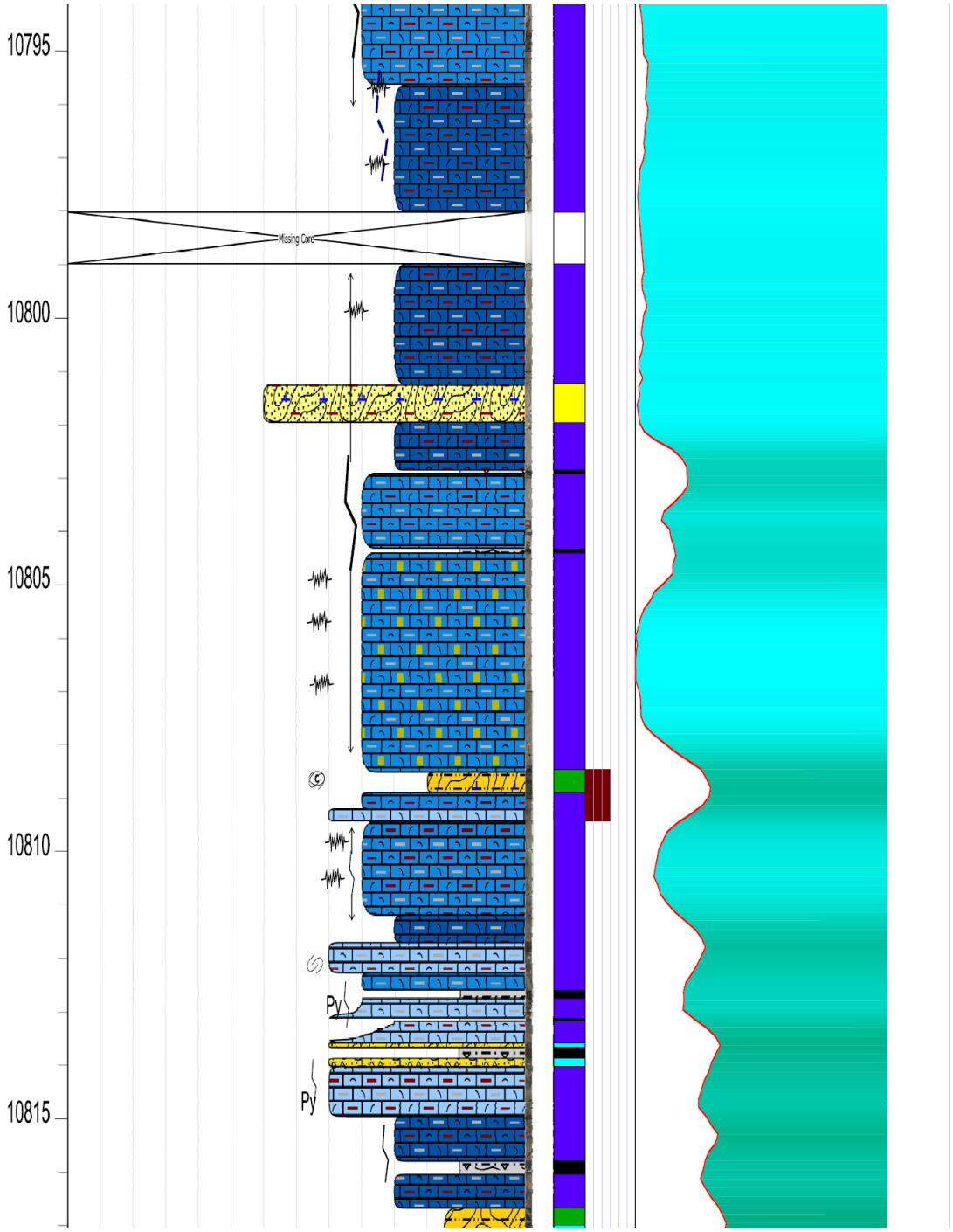
10795
10800
10805
10810
10815
Missing Core
Py
Py

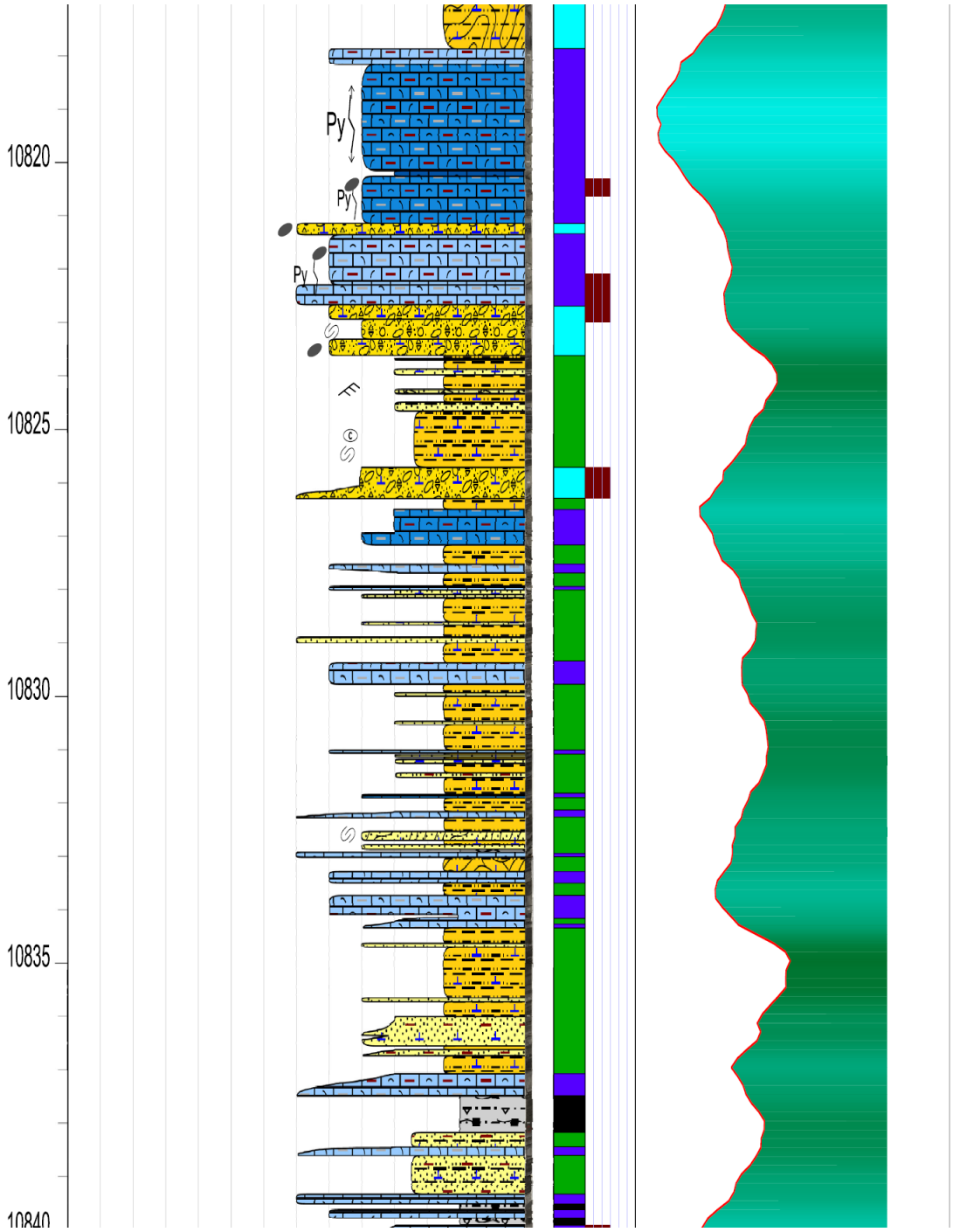
10820
10825
10830
10835
10840
Py
Py
Py
FSC
S
S

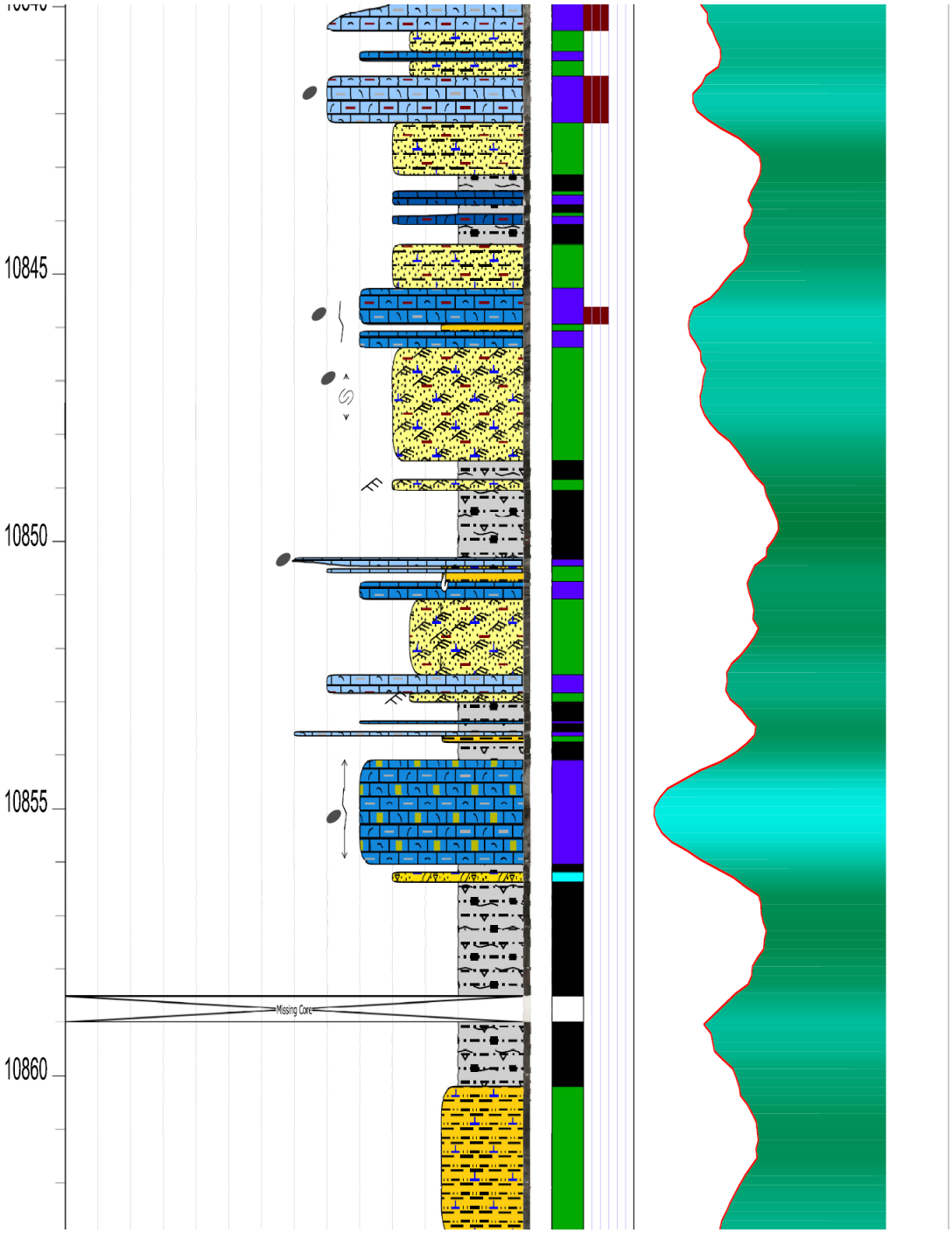
10845
10850
10855
10860
Missing Core

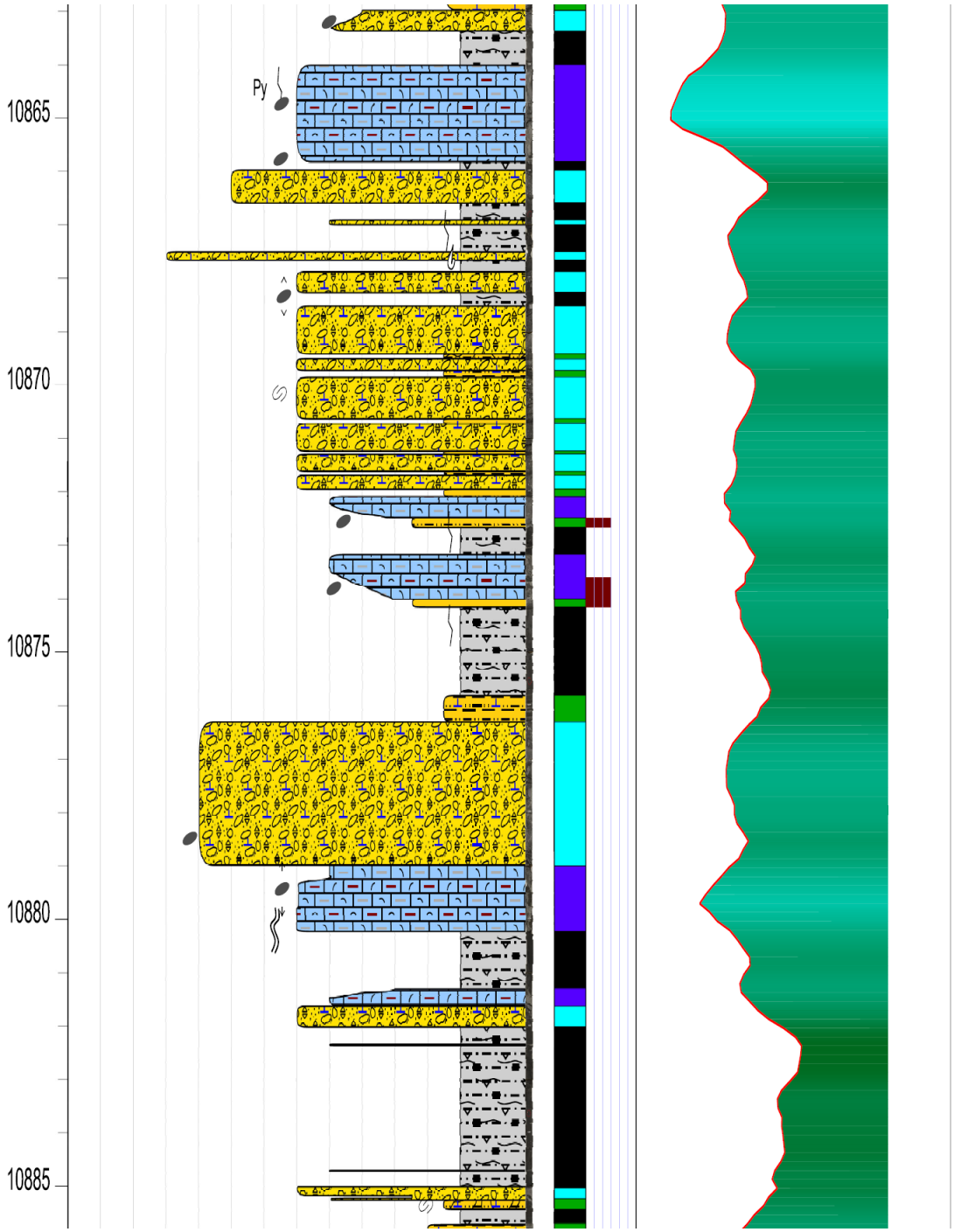
Py
10865
10870
10875
10880
10885

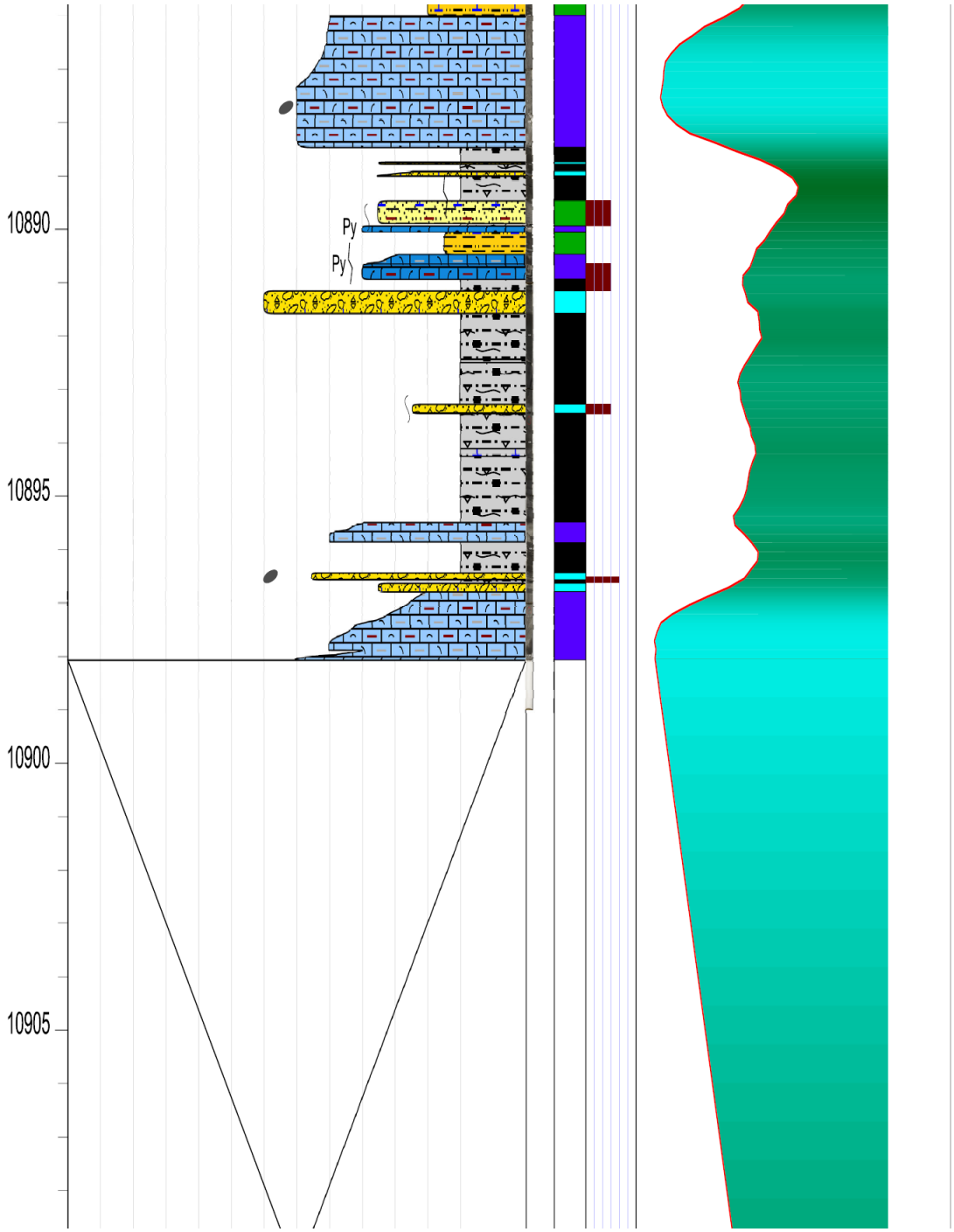
10890
10895
10900
10905
Py
Py

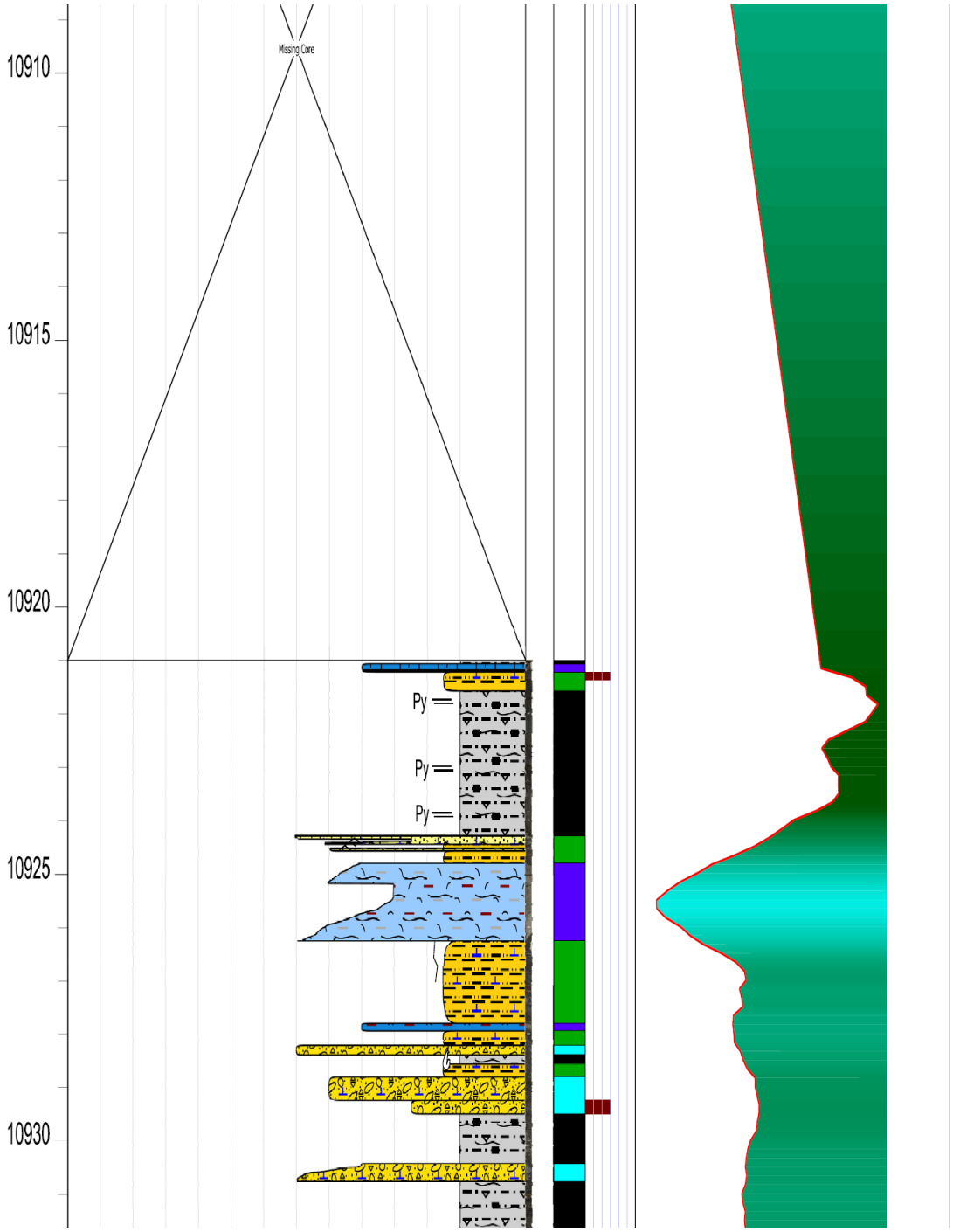
Missing Core
10910
10915
10920
10925
10930
Py
Py
Py

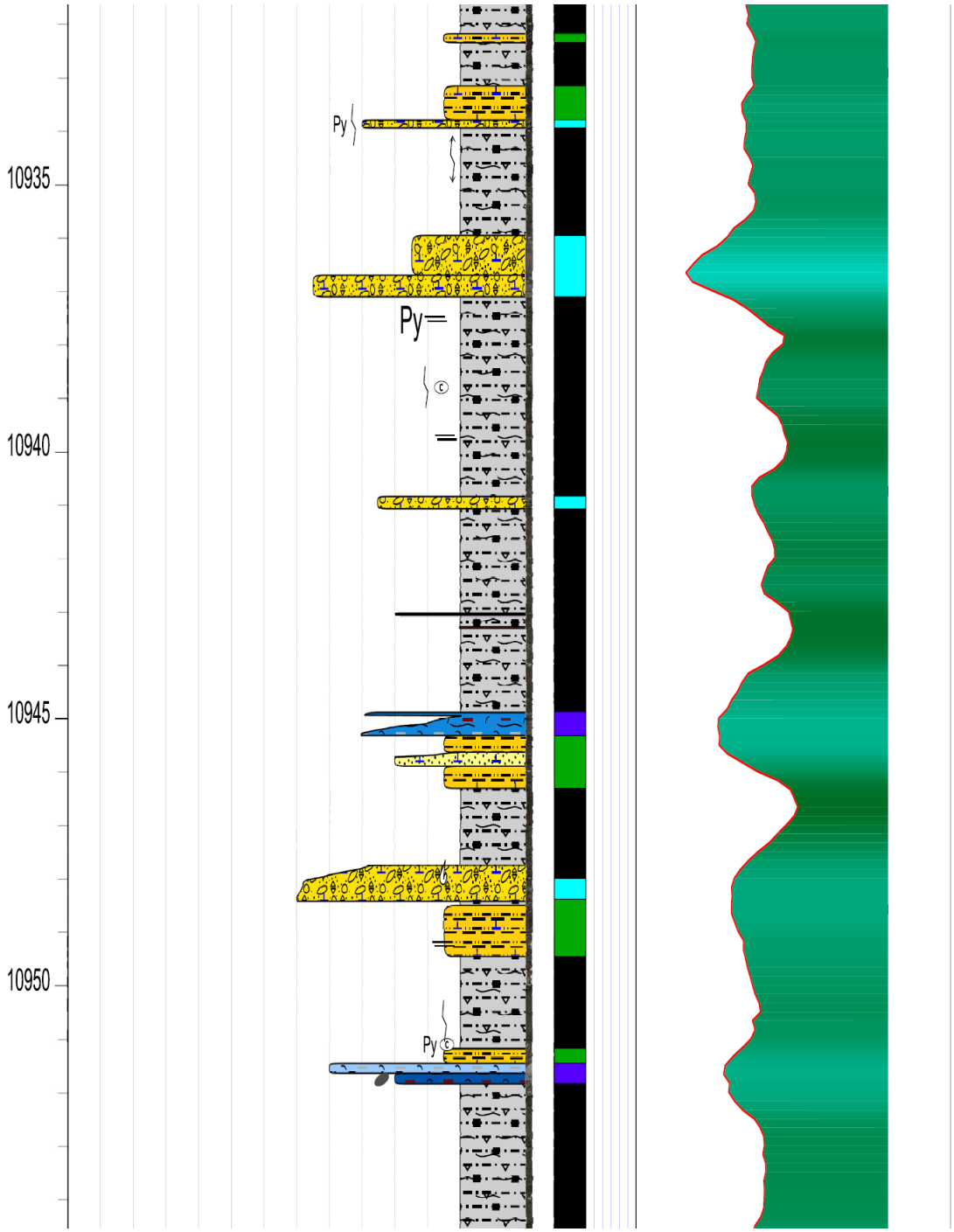
10935
10940
10945
10950
Py
Py
Py

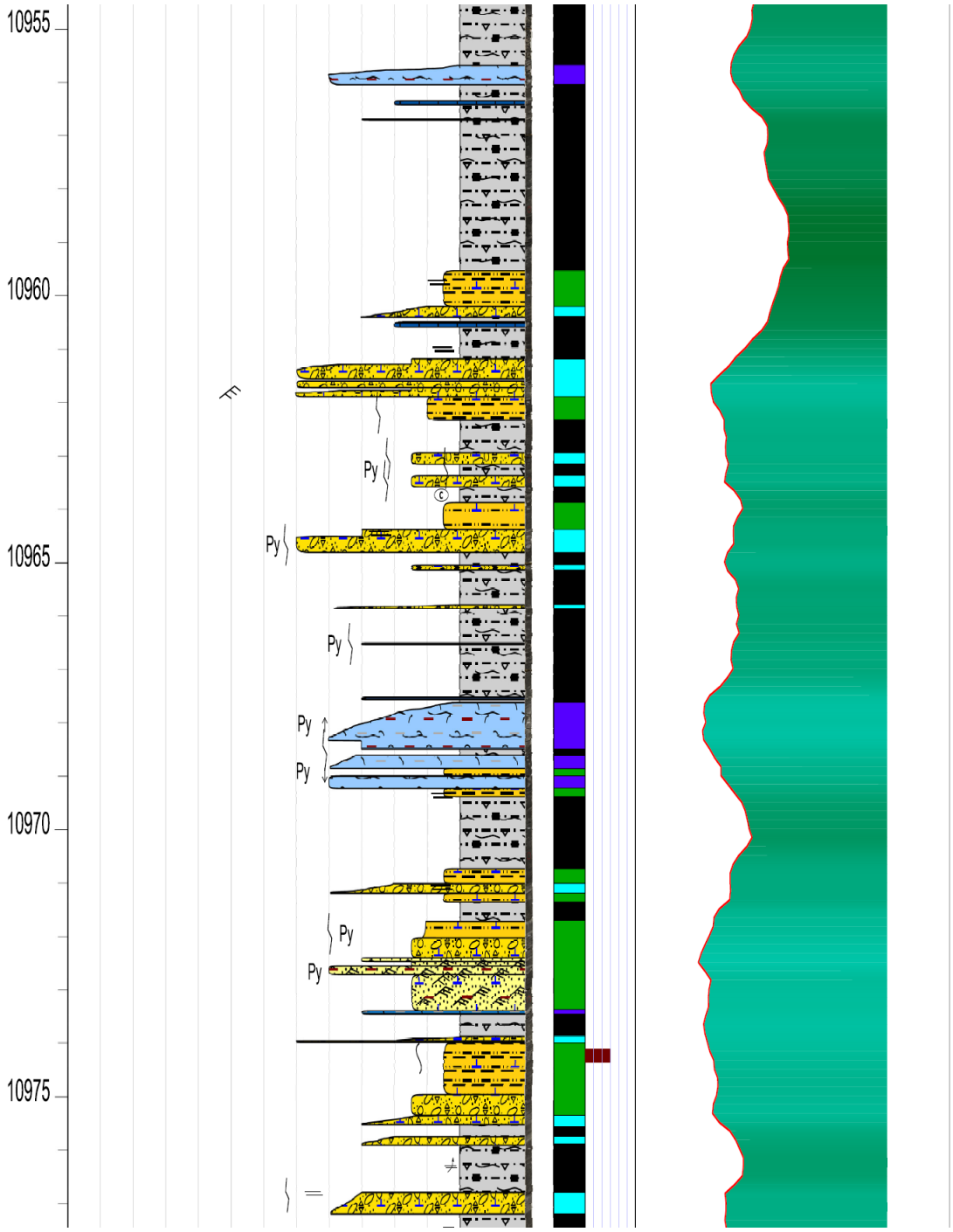
10955
10960
10965
10970
10975
Py
Py
Py
Py
Py
Py
Py
Py

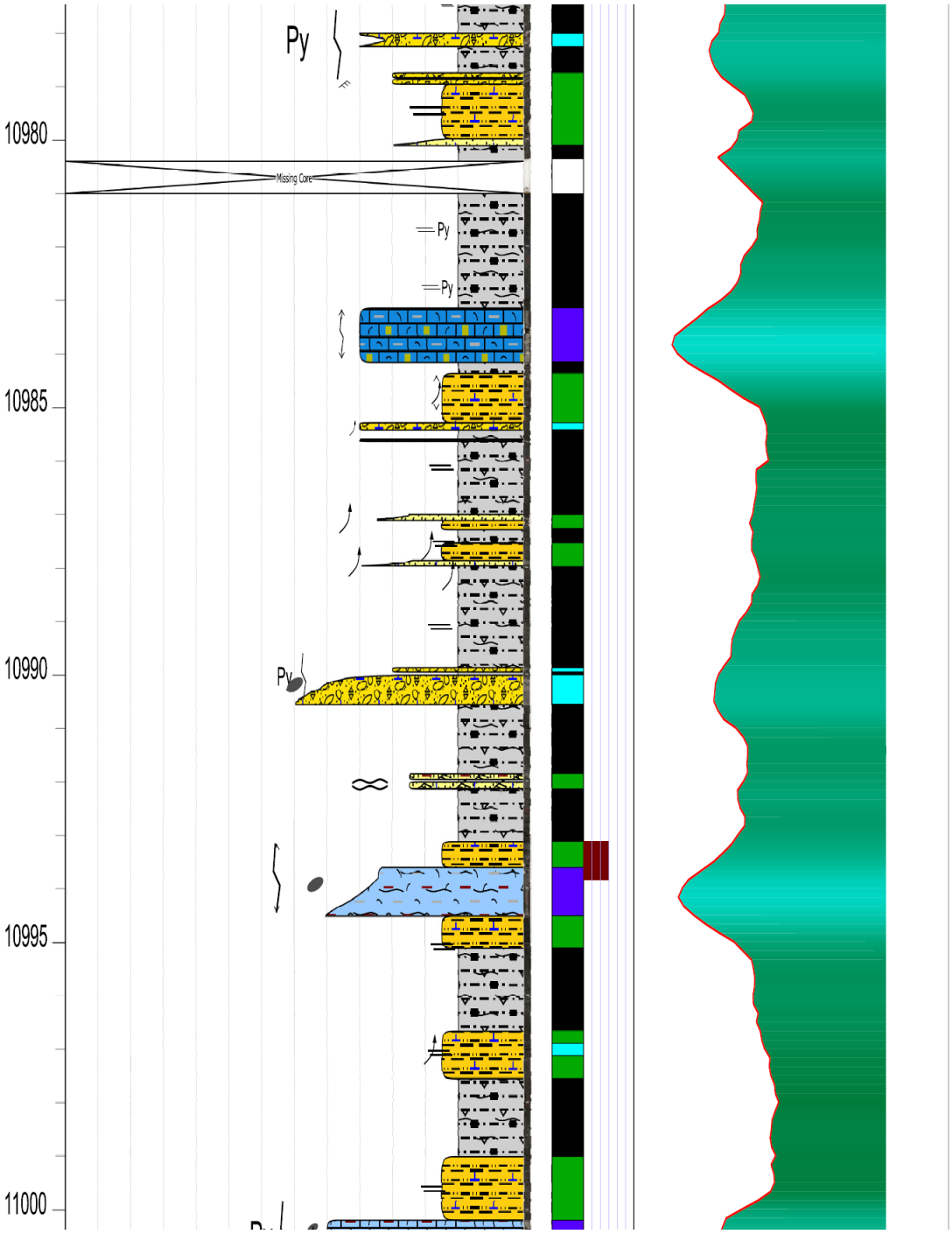
Py
10980
Missing Core
Py
Py
10985
10990
Py
10995
11000

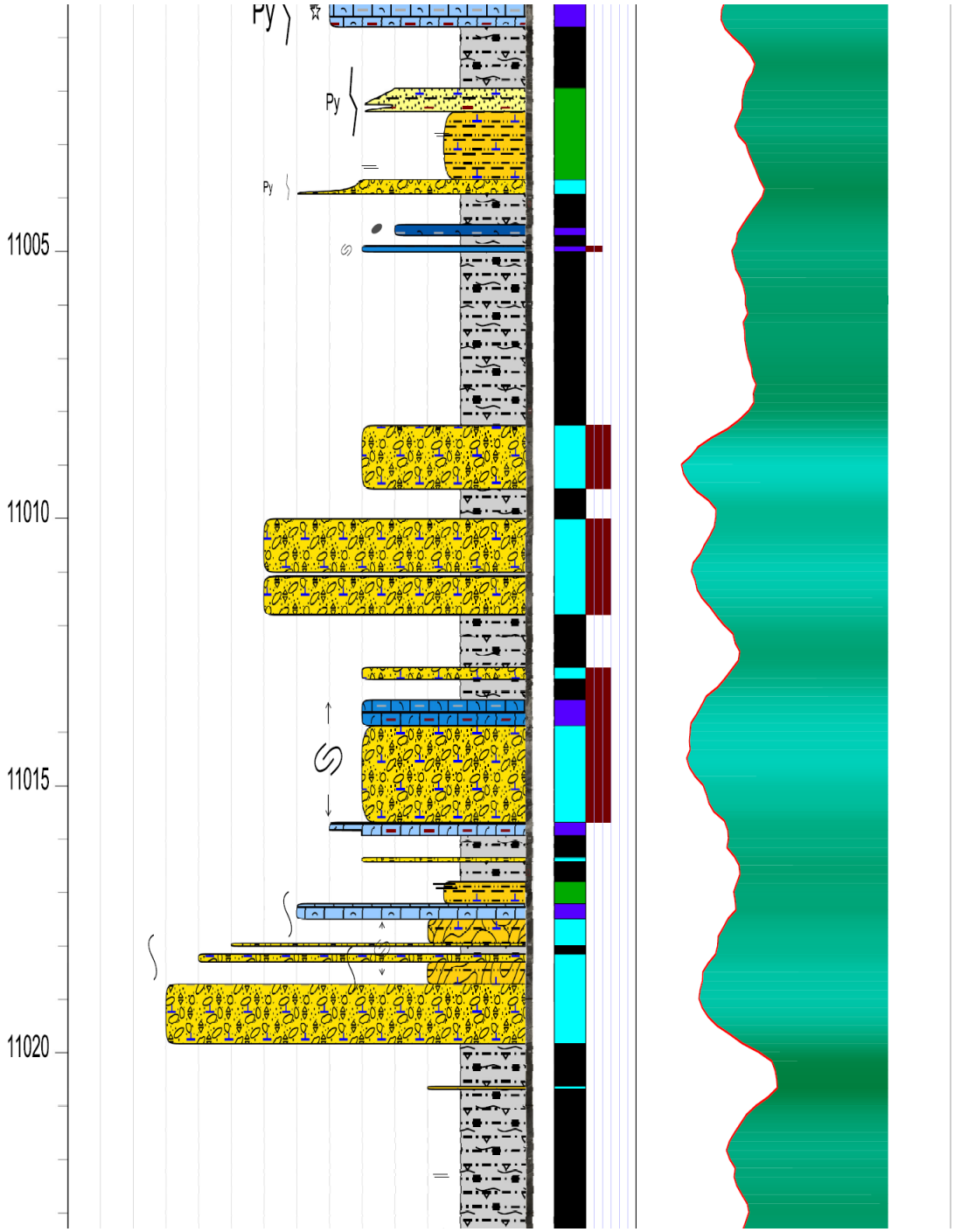
Py
Py
Py
11005
11010
11015
11020

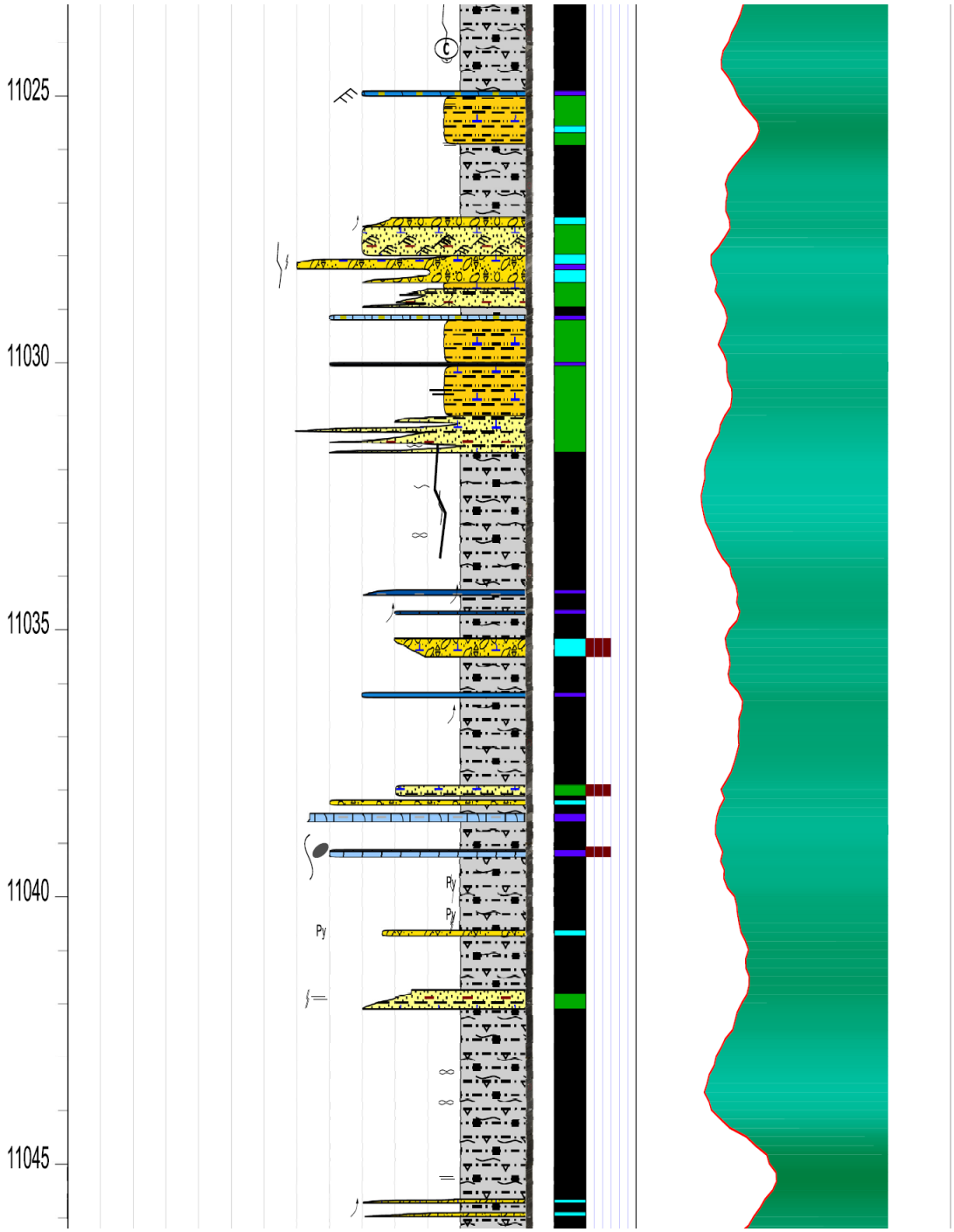
11025
11030
11035
11040
11045
C
F
Py
Py
Py

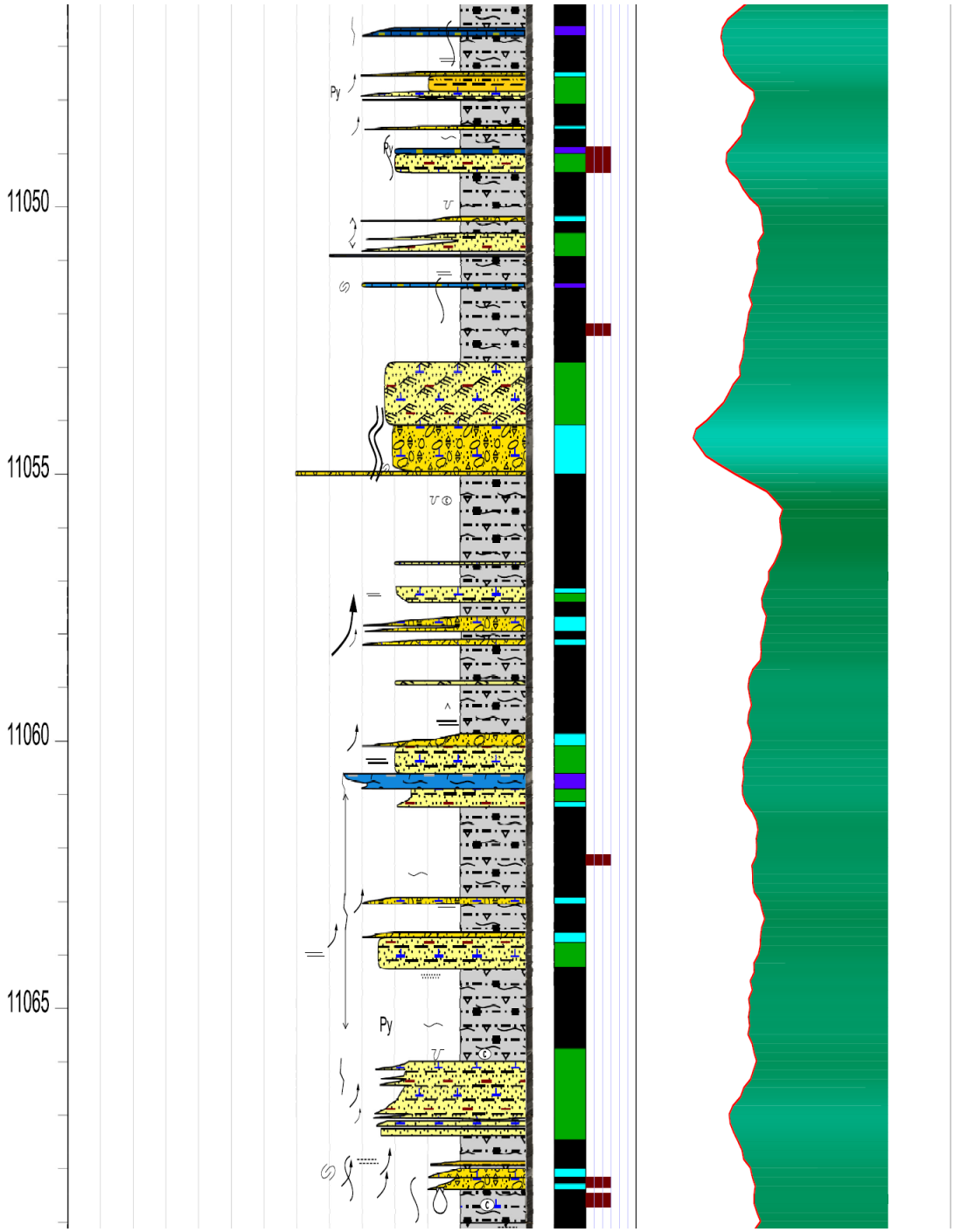
11050
11055
11060
11065
Py
Py
Py